ISSN 0736-5306

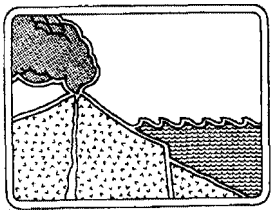

SCIENCE OF TSUNAMI HAZARDS

The International Journal of The Tsunami Society

Volume 19 Number 1 2001

copyright © 2001
THE TSUNAMI SOCIETY
P. 0. Box 37970,
Honolulu, HI 96817, USA

OBJECTIVE: **The Tsunami Society** publishes this journal to increase and disseminate knowledge about tsunamis and their hazards.

DISCLAIMER: Although these articles have been technically reviewed by peers, **The Tsunami Society** is not responsible for the veracity of any statement , opinion or consequences.

EDITORIAL STAFF

Dr. Charles Mader, Editor

Mader Consulting Co.

1049 Kamehame Dr., Honolulu, HI. 96825-2860, USA

Mr. Michael Blackford, Publisher

EDITORIAL BOARD

Dr. Antonio Baptista, Oregon Graduate Institute of Science and Technology

Professor George Carrier, Harvard University

Mr. George Curtis, University of Hawaii - Hilo

Dr. Zygmunt Kowalik, University of Alaska

Dr. T. S. Murty, Baird and Associates - Ottawa

Dr. Shigehisa Nakamura, Kyo to University

Dr. Yurii Shokin, Novosibirsk

Mr. Thomas Sokolowski, Alaska Tsunami Warning Center

Dr. Costas Synolakis, University of California

Professor Stefano Tinti, University of Bologna

TSUNAMI SOCIETY OFFICERS

Mr. James Lander, President

Dr. Tad Murty, Vice President

Mr. Michael Blackford, Secretary

Dr. Barbara H. Keating, Treasurer

Submit manuscripts of articles, notes or letters to the Editor. If an article is accepted for publication the author(s) must submit a camera ready manuscript in the journal format. A voluntary $30.00 page charge for Tsunami Society members, $50.00 for non-members will include 50 reprints.

SUBSCRIPTION INFORMATION: Price per copy $50.00 USA

Permission to use figures, tables and brief excerpts from this journal in scientific and educational works is hereby granted provided that the source is acknowledged. Previous issues of the journal are available in PDF format at **http://epubs.lanl.gov/tsunami/** and on a CD-ROM from the Society.

ISSN 0736-5306 **http://www.ccalmr.ogi.edu/STH**

Published by The Tsunami Society in Honolulu, Hawaii, USA

LITUYA BAY CASE: ROCKSLIDE IMPACT AND WAVE RUN-UP

Hermann M. Fritz[1], Willi H. Hager[2] and Hans-Erwin Minor[3]

Laboratory of Hydraulics, Hydrology and Glaciology (VAW)
Swiss Federal Institute of Technology (ETH)
CH-8092 Zurich, Switzerland

ABSTRACT

On July 8, 1958, an 8.3 magnitude earthquake along the Fairweather fault triggered a major subaerial rockslide into Gilbert Inlet at the head of Lituya Bay on the South coast of Alaska. The rockslide impacted the water at high speed creating a giant nonlinear wave and the highest wave run-up in recorded history. The soliton like wave ran up to an altitude of 524 m causing forest destruction and erosion down to bedrock on a spur ridge in direct prolongation of the slide axis. Total area between trimline of forest destruction on shores of Lituya Bay and high-tide shoreline covered about 10 km^2. A cross-section of Gilbert Inlet was rebuilt at 1:675 scale in a two-dimensional physical laboratory model at VAW. The subaerial rockslide impact into Gilbert Inlet, wave generation, propagation and run-up on headland slope were considered in a geometrically undistorted Froude similarity model. A novel pneumatic landslide generator was used to generate a high-speed granular slide with controlled impact characteristics. State-of-the-art laser measurement techniques such as particle image velocimetry (PIV) and laser distance sensors (LDS) were applied to the decisive initial phase with rockslide impact and wave generation. PIV-measurements of wave run-up on headland slope were conducted to complement wave and run-up gage records. PIV provided instantaneous velocity vector fields in a large area of interest and gave insight into kinematics of wave generation and run-up. The whole process of a high speed granular slide impact may be subdivided into two main stages: a) Rockslide impact and penetration with flow separation, cavity formation and wave generation, and b) air cavity collapse with rockslide run-out and debris detrainment causing massive phase mixing. Impact stages overlap and their transition from wave generation to propagation and run-up is fluent. Formation of a large air cavity – similar to an asteroid impact – in the back of the rockslide is highlighted. The laboratory experiments confirm that the 1958 trimline of forest destruction on Lituya Bay shores was carved by a giant rockslide generated impulse wave. The measured wave run-up perfectly matches the trimline of forest destruction on the spur ridge at Gilbert Inlet. Back-calculation of wave height from observed trimline of forest destruction using Hall and Watts (1953) run-up formula equals measured wave height in Gilbert Inlet. PIV-measurements of wave run-up indicate that enough water ran up the headland slope to cause the flooding observed in Lituya Bay as estimated by Mader (1999) with numerical simulations of the whole Lituya Bay.

---

[1] Research Engineer, VAW, ETH-Zentrum, CH-8092, Switzerland
[2] Professor, VAW, ETH-Zentrum, CH-8092, Switzerland
[3] Professor, Director of VAW, ETH-Zentrum, CH-8092, Switzerland

INTRODUCTION

Lituya Bay is a T-shaped tidal inlet that cuts through the coastal lowlands and the foothills flanking the Fairweather Range of the St. Elias Mountains on the south coast of Alaska, Figs.1 and 2. The stem corresponding to the main part of the T-shaped bay is 12 km long and extends northeastward from the bay entrance. The width of the stem ranges from 1.2 to 3.3 km except at the entrance, which is only 300 m wide. The bay fills and slightly overflows a depression carved by a valley glacier of which Lituya, North Crillon and Cascade glaciers are remnants. Submarine contours show a pronounced U-shaped trench with steep walls and a broad flat floor sloping gently downward from the head of the bay to a maximum depth of 220 m. Minimum depth at the entrance of the bay is 10 m. At the head of the bay the walls are fjord-like glacially over-steeped. The walls have been buttressed by glaciers until recently. Radiocarbon dates on high moraines suggest retreat of glaciers only in the last millennium (Slingerland and Voight, 1979). The two arms at the head of the bay are part of a great trench that extends tens of kilometers to the northwest and southeast as a topographic expression of a major transform fault, named Fairweather fault, as shown in Fig. 2.

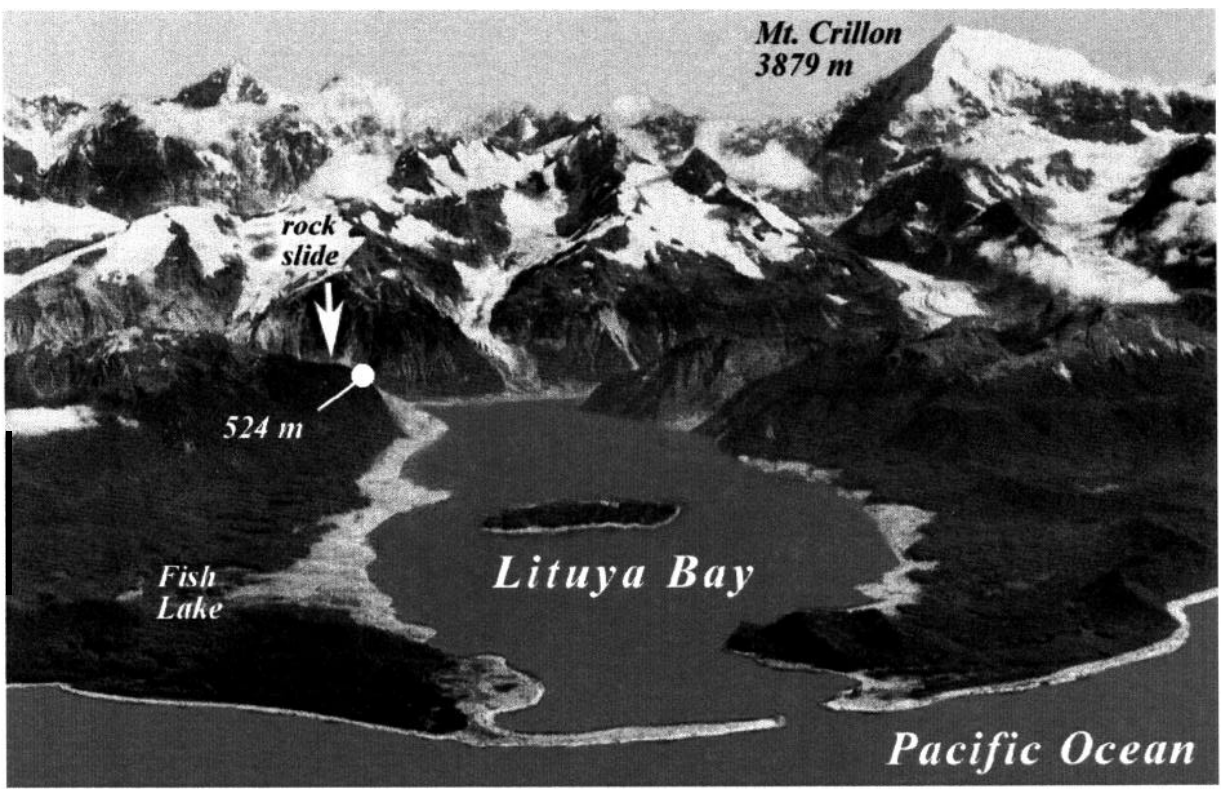

Fig. 1 **Lituya Bay** overview in August 1958 (Miller, 1960). Forest destroyed to a maximum elevation of 524 m and a maximum distance of 1100 m from high-tide shoreline at Fish Lake due to a giant wave generated on July 9th 1958 by a rockslide at the head of the bay.

Giant waves have occurred in Lituya Bay at least four and probably five times during the last two centuries emphasizing the unique geologic and tectonic setting of the bay. Frequent occurrence of giant waves in Lituya Bay, as compared to other similar bays, is attributed to the combined effect of recently glaciated steep slopes, highly fractured rocks and deep water in an active fault zone, heavy rainfall, frequent freezing and thawing (Miller, 1960). Three extreme wave run-ups in 1853 or 1854, 1936 and 1958 carved sharp trimlines of chopped trees to elevations beyond 100 m on to the slopes of Lituya Bay.

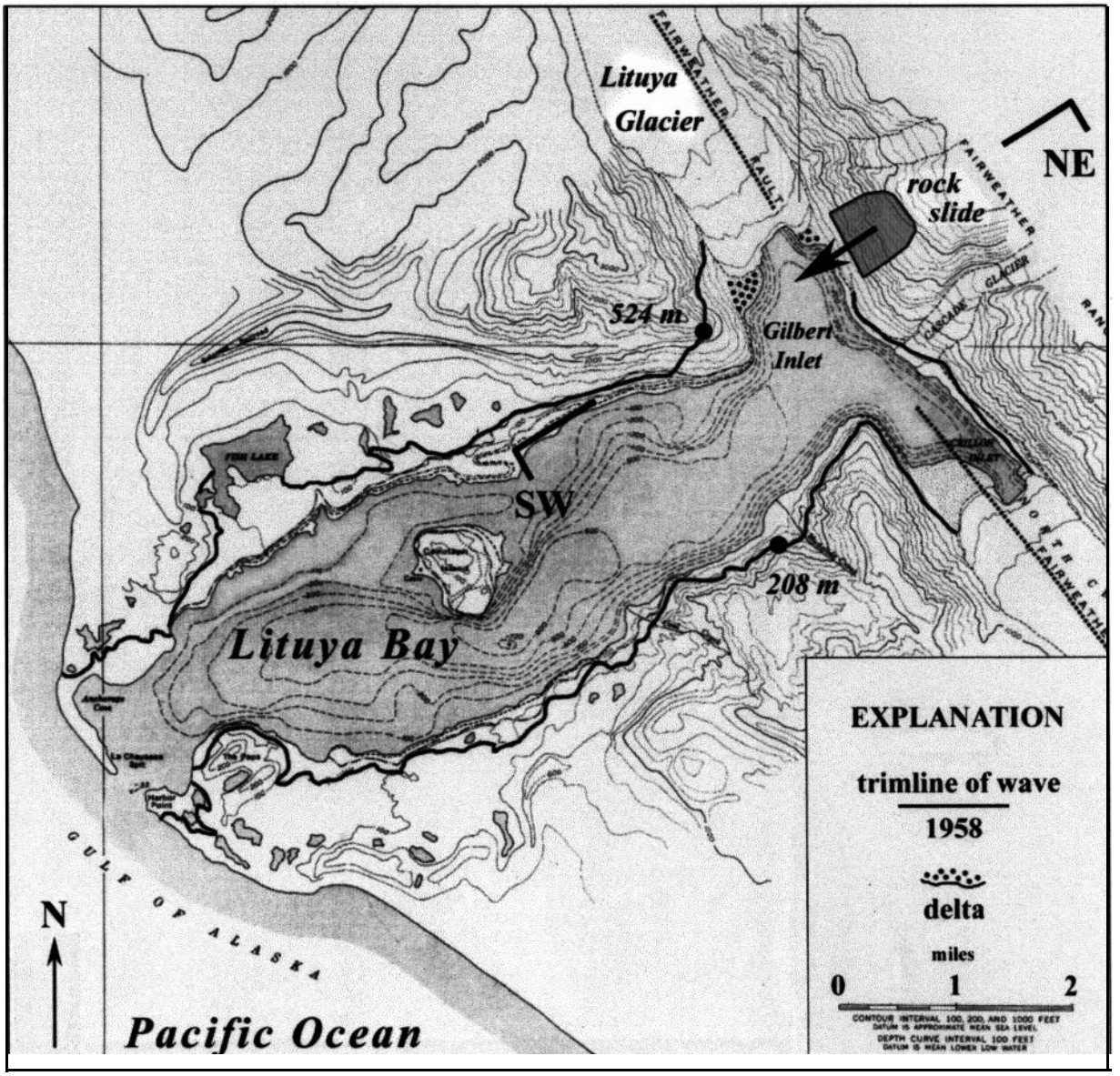

Fig. 2 **Lituya Bay map** showing topographic and bathymetric contours, trace of Fairweather fault., 1958 rockslide and **trimline** of giant wave run-up (Miller, 1960). Forests destroyed to maximum elevations of 524 m and 208 m on north and south shores, respectively.

In 1853 or 1854 a giant wave caused forest destruction on Lituya Bay shores to a maximum elevation of 120 m (Miller, 1960). A rockslide from the steep wall on the south shore of Lituya Bay near **Mudslide** Creek would best account for the maximum height of destruction directly opposite on the north shore of the bay. The **trimline** of the 1936 waves reaches a maximum height of 150 m above sea level on the northeast wall of Crillon Inlet and indicates a wave generation near the head of Crillon Inlet. Miller (1960) suggests a rockslide or rock avalanche from the southwest wall of Crillon Inlet, opposite the high point on the trimline. Eyewitness accounts question this hypothesis to some extent especially regarding time scale of the observed three waves of increasing height (Miller, 1960). In 1958 the hugest wave run-up of 524 m in recorded history was observed on a spur ridge on the southwest wall of Gilbert Inlet. Only the 1958 event is further considered here since the causes of the earlier events remain unconfirmed.

1958 ROCKSLIDE IMPACT AND WAVE RUN-UP

Beginning 10:16 p.m. local time, July 9, 1958, the southwest sides and bottoms of Gilbert and Crillon Inlets moved northwestward and up relative to the northeast shore at the head of the bay, on the opposite side of the Fairweather fault. Total movement as much as 6.4 m horizontally and 1 m vertically was noted (Tocher and Miller, 1959). Intense shaking in Lituya Bay continued for 1 to 4 minutes, the range of estimates of two eyewitnesses that anchored in the bay. The earthquake had a magnitude of 8.3 on Richter Scale. Nor less than 1 minute nor more than 2% minutes after the earthquake was first felt a large mass of rock slid from the northeast wall of Gilbert Inlet (Figs. 2 and 3).

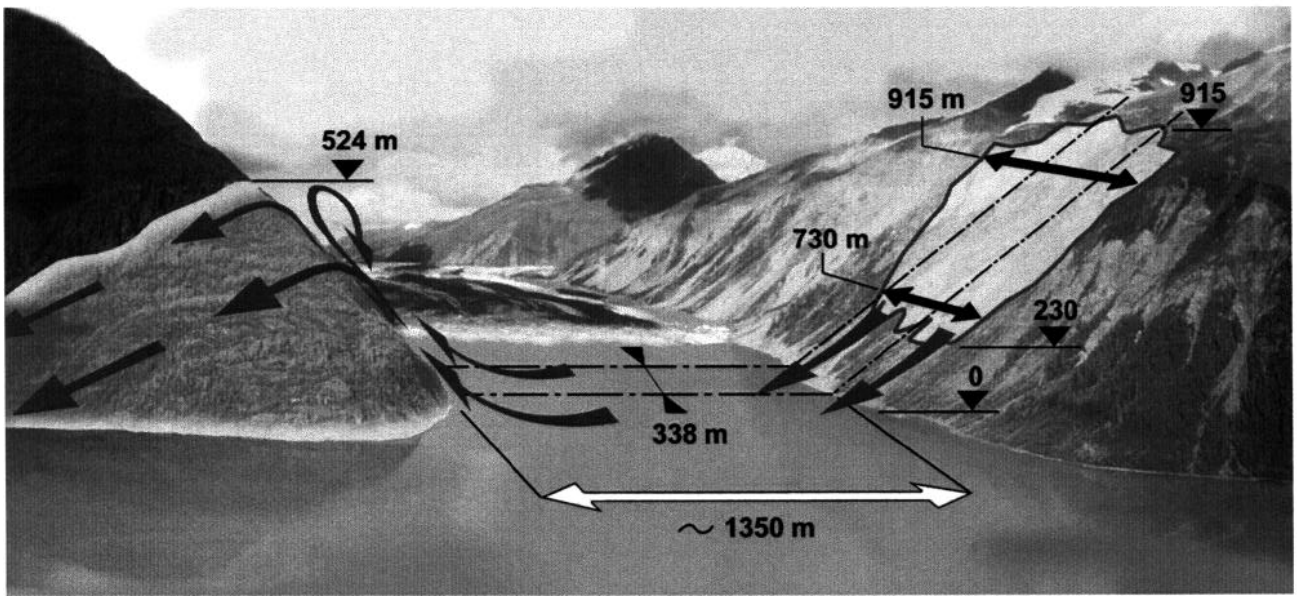

Fig. 3 Gilbert Inlet illustration showing rockslide dimensions, impact site and wave run-up to 524 m on spur ridge directly opposite to rockslide impact. Direction of view is North and the front of Lituya Glacier is set to 1958 post slide position. Illustration background is synthesized from two oblique images taken in 1997 (Photos: courtesy of Charles L. Mader).

The rockslide was triggered impulsively by fault movement and intense earthquake vibrations giving a sharp localization on time axis. It is highly probable that the entire mass plunged into Gilbert Inlet as a unit at the time of the earthquake. Pararas-Carayannis (1999) classified the mass movement as subaerial rockfall to distinguish from gradual processes of ordinary landslides whereas Miller (1960) judged it to be near the borderline between rockslide and rockfall as defined by Sharpe (1938) and Vames (1958). The rockslide occurred in an area of previously active sliding to an altitude of 915 m on a slope averaging 40". The rocks are mainly amphibole and biotite schists with an assumed density of 2.7 t/m^3. The dimensions of the slide on the slope as mapped by Miller (1960) are accurate, but the thickness of slide mass normal to the slope could be estimated only roughly (Miller, 1960). The main mass of the slide presumably involved a prism of rock roughly triangular in cross-section, with width dimensions from 732 m to 915 m (Miller, 1960 and Slingerland and Voight, 1979), length measured down the slope of 970 m (Slingerland and Voight, 1979), maximum thickness of about 92 m normal to the slope, and a center of gravity at about 610 m altitude (Miller, 1960). Dimensions are illustrated in Fig. 3. Miller estimated the volume from these as 30.6×10^6 m^3.

Prior to the rockslide low deltas of gravel had built out into Gilbert Inlet at the southeast and northwest margins of the Lituya Glacier front. Part of the slide must have hit the Lituya Glacier and glacial gravel deltas due to the pre-slide situation of slide mass, deltas and glacier front as illustrated in Fig. 2. A detailed

pre and post slide situation of Gilbert Inlet was indicated in Miller (1960). The Lituya Glacier front was a nearly straight vertical wall almost normal to the axis of Gilbert Inlet after the rockslide, shown in Fig. 4b).

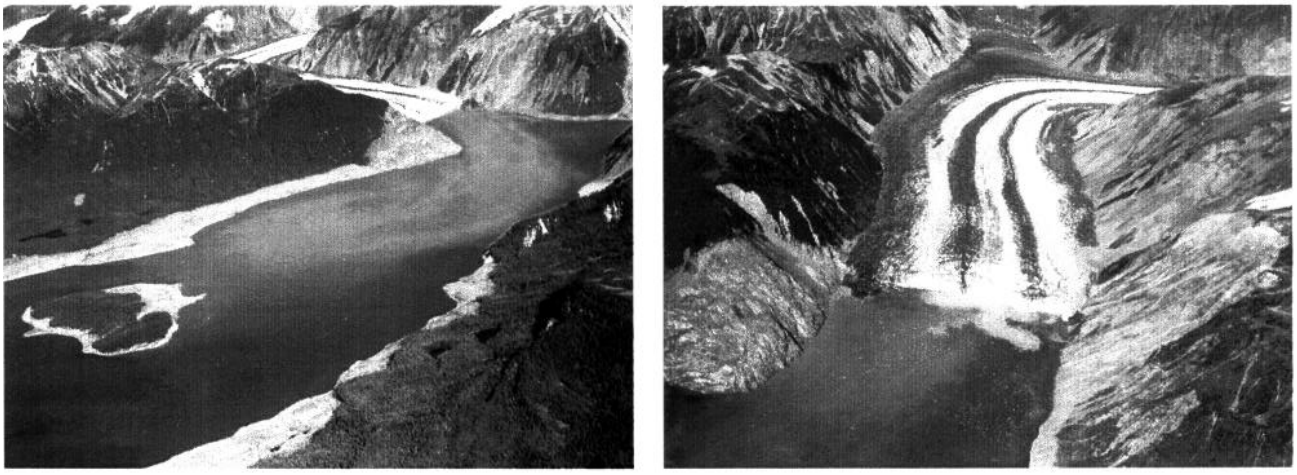

Fig. 4 **Trimlines** carved by giant wave in 1958: a) NE-view of Lituya Bay from Cenotaph Island to Gilbert Inlet with rockslide scar at the head of the bay, trimlines of destructed forest with spur ridge where the wave ran up to 524 m and partially overtopped. b) NW-view of Gilbert Inlet with landslide scar, new front of Lituya Glacier and effect of wave run-up to 524 m on the spur ridge wiping out all trees and eroding the soil down to the bedrock. (Photos: courtesy of USGS).

During the event as much as 400 m of ice had been sheared off on parts of the glacier front and the gravel deltas were pushed or washed away. The rockslide impact created a giant gravity wave similar to a solitary wave with a maximum wave run-up of 524 m in straight prolongation of the slide axis on a spur ridge on the southwest shore of Gilbert Inlet (Figs. 4 to 5a).

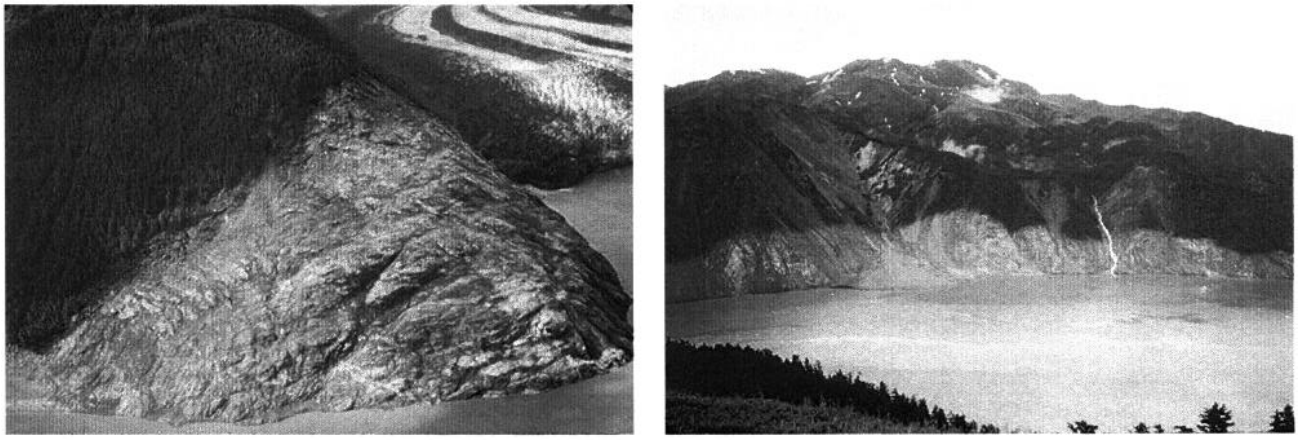

Fig. 5 **Highest marks** on trimlines carved by giant wave in 1958: a) N-view of spur ridge cleared from trees and soil down to bare rock up to a maximum altitude of 524 m. b) S-view of trimline in the Mudslide Creek area on the south shore of Lituya Bay with wiped out trees to an altitude of 208 m. (Photos: courtesy of USGS).

The maximum wave run-up of the 1958 event was incomparable at the time to any other event. The run-up of 524 m is seven times higher than the highest wave run-up observed 1936 in Norwegian Lake Loen with 75 m (Jørstad, 1968) and roughly doubles wave run-ups in Vajont reservoir, Italy (Müller, 1964) and Spirit Lake, USA (Voight et al., 1983). On October 9, 1963 the southern flank of Vajont reservoir collapsed

on a length of 2 km. Collapse occurred during reservoir draw down in an attempt to reduce flank creeping and the reservoir was only about two-thirds full. The partially submerged rockslide with a volume of 0.24 km^3 penetrated like a piston almost horizontally into the reservoir at velocities up to 30 m/s. Wave run-up in slide axis reached the lowest houses of Casso 270 m above reservoir level before impact or 245 m above dam crest. On May 18, 198 1 a lobe from the rockslide-avalanche off Mount St. Helens rammed into Spirit Lake at an assumed velocity of 70 to 80 m/s. The impact caused a wave run-up to 260 m above original lake level and raised the mean lake level by 60 m.

A simplified 3D physical model of Lituya Bay at a 1 :1 '000 scale was constructed at the University of California, Berkeley (R.L. Wiegel in Miller, 1960, pp. 65-66). Wiegel concluded from physical model observations, that a sheet of water washed up the slope opposite to the landslide to an elevation of at least three times the water depth for a slide impacting Gilbert Inlet as a unit and very rapidly. At the same time a large wave, several hundred feet high, moved in the southerly direction, causing a peak rise to occur in the vicinity of Mudslide Creek. The highest mark of chopped trees at an altitude of 208 m on the south shore trimline is shown in Fig: 5b). Wiegel(1964) estimated the hydrodynamic forces exerted on the trees by the wave as roughly ten times greater than the force necessary to snap or uproot trees. The wave then swung around into the main portion of Lituya Bay, due to refraction and diffraction. The movements of the main wave and the tail were complicated within the bay by reflections and bathymetric effects, but scale modeling apparently produced a good approximation to the Lituya Bay event. Unfortunately no measured data are available from these 3D experiments.

PHYSICAL MODEL

The subaerial rockslide that impacted into Lituya Bay at high velocity was considered in a geometrically undistorted Froude similarity model (Hughes, 1993). A cross section of Gilbert Inlet, in slide axis, was modeled at a 1:675 scale in a rectangular prismatic water wave channel (L x W x H: 11 m, 0.5 m and 1 m). The cross section modeled of Gilbert Inlet is shown in Fig. 6 and its NE-SW orientation in Fig. 2.

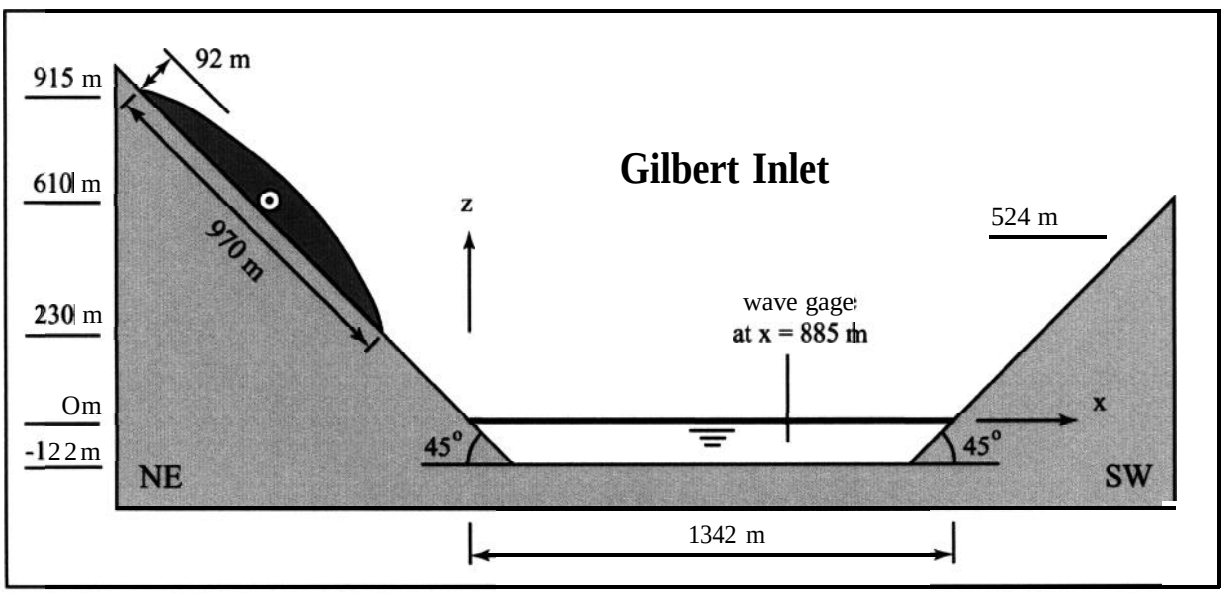

Fig. 6 **Cross section** of Gilbert Inlet along slide axis in NE to SW orientation, indicated in Fig. 2. Geometry corresponds to physical model assumptions and simplifications.

The slice rebuilt in the model is shown in Fig. 3 with dashed lines. The width of 338 m represented in the 2D model corresponds to 40 % of the mean slide width of 823 m (Slingerland and Voight, 1979). The volume per unit width $V_s' = 37.2 \times 10^3$ m^3/m' was estimated by equal distribution of the total slide volume $V_s = 30.6 \times 10^6$ m^3 over an averaged slide width of 823 m. This is a conservative assumption neglecting the volume concentration in the slide center due to roughly triangular slide cross sections along the slope. The indicated geometry corresponds to physical model assumptions with a hill angle a and headland angle β of 45". Simplified Gilbert Inlet bathymetry roughly corresponds to bedrock of the glacially carved U-shaped trench. Pre-slide gravel deltas along parts of the glacier front shown in Fig. 2 were neglected. The assumed stillwater depth h = 122 m matches the maximum water depth in Gilbert Inlet. Modeled Inlet width of 1342 m equals 11 times stillwater depth and 1.6 times mean slide width. Fig. 7 defines the notation for rockslide impact, wave propagation and wave run-up.

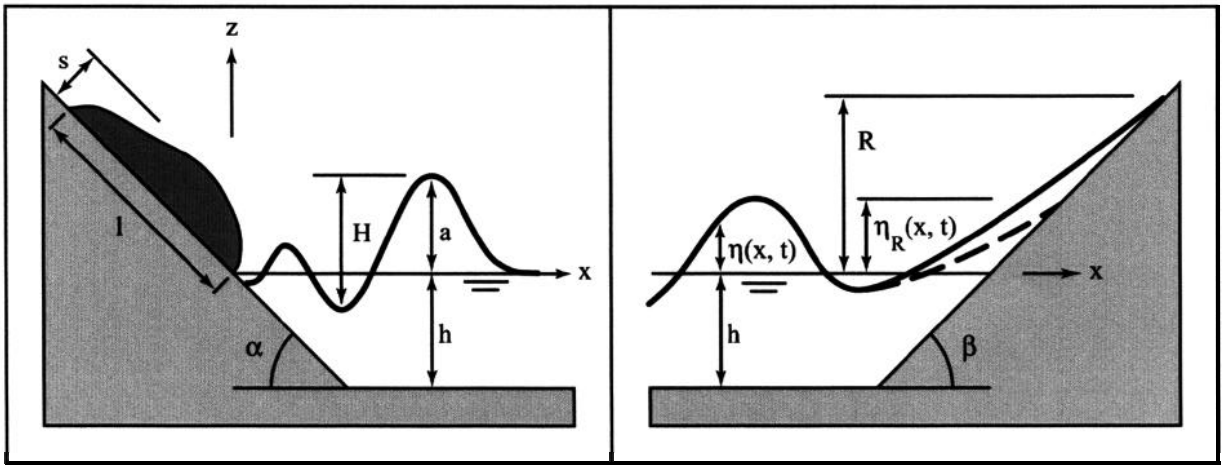

Fig. 7 Notation for rockslide impact, wave propagation and wave run-up.

In a 2D-model radial or lateral wave spreading is neglected. From the impact site in Gilbert Inlet lateral spreading only occurred in southern direction. In northern direction the impact area is confined to the Lituya Glacier front. Pre-slide position of the glacier front and gravel deltas reached into rockslide path. Both slide and wave must have been partially deflected in southern direction. This deflection possibly caused a focusing of wave run-up on a small area on the headland confirmed by extreme altitude gradients along the trimline on spur ridge (Figs. 4b and 5a). In this specific topographic situation wave height reduction due to 3D effects is further limited by the small ratio of 1.6 between propagation distance and slide width. Therefore it is expected that the present 2D-model can give a good estimate of wave and run-up heights in Gilbert Inlet. Landslides were modeled with an artificial granular material (PP-$BaSO_4$) with a mean grain diameter of 4 mm. The granular material consisted of 87 % Barium-Sulphate compounded with 13 % Polypropylene. Its density of 2.64 t/m^3 perfectly matches the assumed schist density of ρ_s = 2.7 t/m^3 and resulted in a slide mass per unit width of m' = 98.5 x 10" t/m'. Mean rockslide impact velocity v_s of 110 m/s is estimated assuming free fall equations for a slide centroid at 610 m elevation according to Noda (1970) and Law and Brebner (1968). The kinetic impact energy of the rockslide is at the upper limit neglecting frictional losses. This gives an impact Froude-number of 3.18. The impact Froude-number is defined as

$$F = \frac{v_s}{\sqrt{gh}} \qquad (1)$$

and relates the mean impact velocity v_s of the centroid to the shallow water wave propagation velocity (Noda, 1970), where g is gravitational acceleration.

INSTRUMENTATION

Rockslide impact characteristics were controlled by means of a novel pneumatic acceleration mechanism (Fritz and Moser, 2001), thus allowing exact reproduction and independent variation of single dynamic slide parameters such as impact velocity, mass and shape. An overview on implementation and combination of the various measurement systems and the pneumatic rockslide generator is shown in Fig. 8. The pneumatic rockslide generator allows to model the transition from block slide motion to granular flow. The first stage with acceleration up to the granulate release velocity corresponds to block sliding whereas the second stage from granulate release to impact on water-body is granular flow. The high-speed rockslide impact initiates an extremely unsteady energy conversion process with rapidly evolving flow fields, inter-phases and phase mixing which poses a major challenge to any measurement system. In the impact area itself only non-intrusive methods can be applied. Three different measurement techniques were built into the physical model: Laser distance sensors (LDS), particle image velocimetry (PIV) and capacitance wave gages (CWG). Fritz (2001) describes all applied measurement systems and their capabilities.

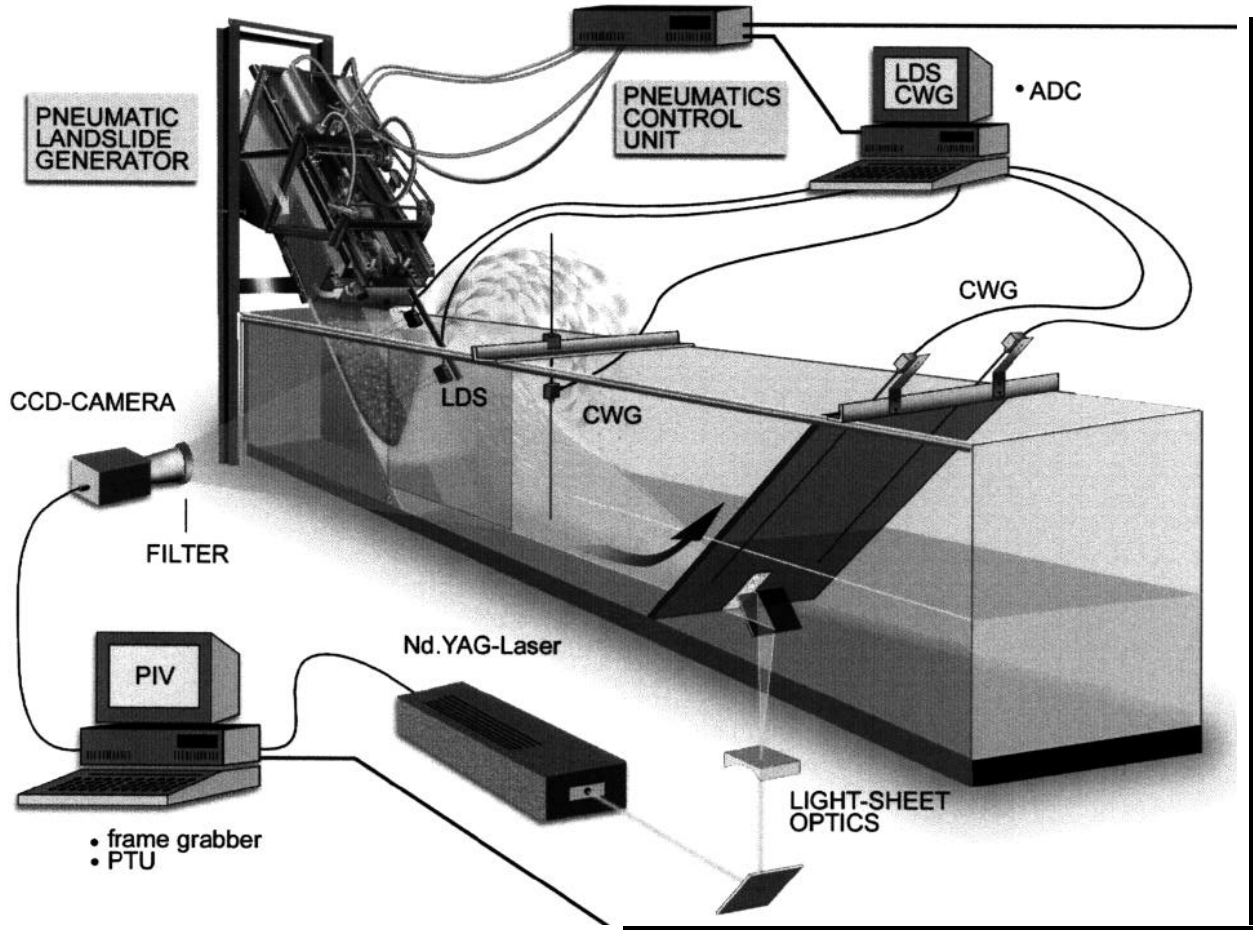

Fig. 8 **Experimental setup** with pneumatic installation and measurement systems: Laser distance sensors (LDS), capacitance wave gages (CWG) and particle image velocimetry (PIV). PIV-System with CCD-camera, twin Nd.YAG-laser, simplified light-sheet and beam guiding optics.

Slide profiles before impact are scanned with two laser distance sensors. Laser distance sensors measure the distance to the granulate based on the triangulation principle. The obtained slide profiles are used to determine slide shape, impact time and velocity. Wave features during propagation and run-up are determined with capacitance wave gages (CWG). One CWG records the wave profile at x = 885 m and two CWGs record wave run-up profiles on the headland ramp. Laser distance sensors and capacitance wave gages are sampled at 20 Hz in prototype time scale. For LDSs and CWGs an accuracy off: 1 m in prototype scale is obtained. The wave run-up records contain only sheets of water on the slope thicker than 5 m. The accuracy of the wave run-up gage measurements is limited to ± 10 m.

Large scale digital PIV is applied to rockslide impact and wave run-up areas. A twin cavity Nd.YAG-laser is used as light source. The light sheet is generated right below the partially glassed channel bottom. For measurements in the impact area the light-sheet is deflected by an under-water mirror axially into the wave generation zone creating a large vertical light-sheet (Fig. 8). For measurements in the wave run-up area the 2"-mirror on channel bottom was removed. Image areas as large as 529(H) x 516(V) m in prototype scale were acquired by means of a mega-resolution progressive scan CCD-camera. By means of cross-correlation analysis instantaneous 2D-2C velocity vector fields were computed using an adaptive multi-pass algorithm (Scarano and Riethmuller, 1999) and second order correlation (Hart, 2000). Spatial resolution is determined by the window size of 8.4 x 8.4 m used in cross-correlation analysis. Time resolution of the PIV-system for 2D-2C velocity vector field estimation was 0.6 Hz in prototype time scale. For peak velocities an accuracy of ± 1 % was reached whereas accuracy reduced proportional to velocity decay for low velocities.

EXPERIMENTAL RESULTS

Introduction

A series of experiments was conducted with the assumptions for Lituya Bay topography, bathymetry, rockslide impact velocity, mass and shape described in the physical model section. The complex phenomena that occur even on macro-scale during this extremely unsteady process with high-speed rockslide impact, air cavity formation, impulse wave generation, propagation and run-up are shown in the photo sequence of Fig. 9. The different process stages from slide impact to wave run-up overlap and their transition is fluent. The slide shape before impact shows a gentle slide front inclination with a continuous increase in slide thickness towards the rear (Fig. 9a). Slide bulking is caused by impact on the water surface and slide deflection at the channel bottom. Flow separation on the rockslide shoulder due to fast slide penetration into the water body creates a large air cavity on the back of the granular slide (Fig. 9b,c). During this separation stage three phases with sharp borderlines may be distinguished: water, granular material and air. The subsequent cavity collapse during slide run-out along the channel bottom causes massive mixing of air and water (Fig. 9d,e,f). Air is entrained into the water mainly due to air inclusion by flow reattachment during cavity collapse and detrainment of the granular material during rockslide run-out along the channel bottom. Phase mixing had little effect on the leading wave because the main wave had propagated out of the impact area before air detrainment occurred. Therefore the leading wave remains widely unaffected by Weber-effects due to surface tension non-similarity in Froude-models. The large nonlinear wave consisting of one single pulse of energy plunges onto the ramp (Fig. 9f). Wave breaking during run-up is initiated but does not fully developed due to the steep slope. The run-up process is more surging than breaking as described by Synolakis (1987) and therefore with little air-entrainment. A thin sheet of water surges up on the headland ramp (Fig. 9g,h). Müller (1995) estimated the viscous damping due to Reynolds non-similarity to be smaller than 5 % for waves smaller than the incident wave height of H = 0.24 m observed in model scale. Stive (1985) demonstrated with an experimental scale series of breaking waves on a beach that there are no significant deviations from the Froude scaling, in a wave height range of approximately 0.1 m to 1.5 m. This result implied that the "superficially" observed difference in air entrainment had no significant influence on the wave dynamics. Scale effects regarding viscosity and surface tension may be assumed smaller than 5 %.

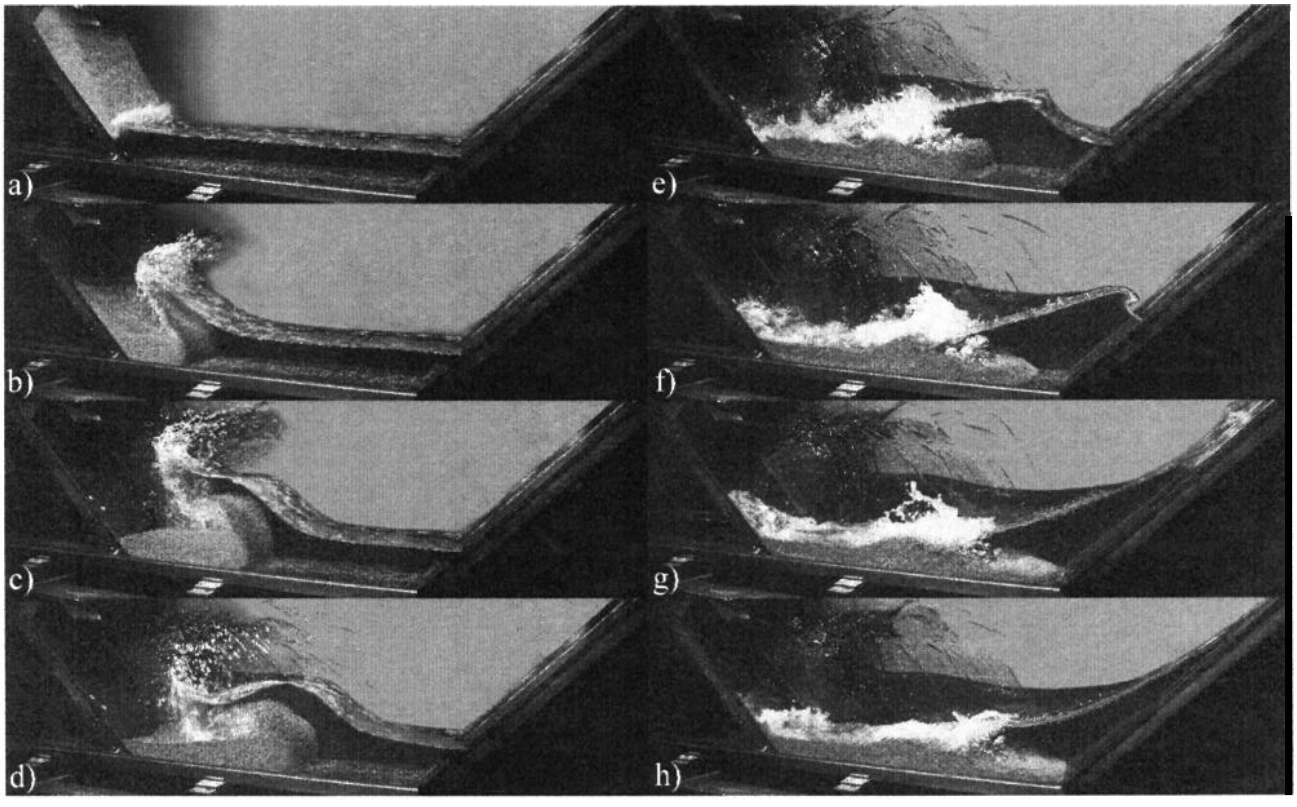

Fig. 9 **Photo-sequence** of a granular slide impact experiment with up-scaled parameters: **F = 3.18,** v_s = 110 m/s, m' = 98.5 x 10^3 t/m', h = 122 m, a= β = 45" at a time increment of 5 s.

Rockslide profile

The granulate (PP-$BaSO_4$) with a mean grain diameter of 4 mm used to model the rockslide is shown in Fig. 10a). As a bulk medium the density is reduced to 1.61 t/m' due to a void fraction of 39 %. The assumed porosity corresponds to data from Alpine debris flows (Tognacca, 1999). For comparison the porosity of a bulk mass of spheres is 48 %.

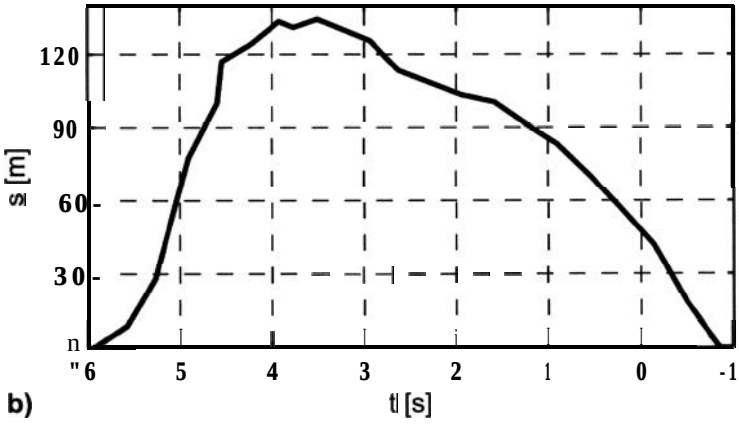

Fig. 10 a) Granulate: PP-$BaSO_4$, d_g = 4 mm, ρ_g = 2.64 g/cm" and **h) granular slide profile** scanned with a laser distance sensor orthogonal to ramp at location x = -67 m and z = 67 m.

To what extent the rockslide broke up before impacting into Gilbert Inlet and if its motion evolved from initial pure sliding into a fully developed debris avalanche is unknown. A rockslide profile scanned with a laser distance sensor orthogonal to the ramp and 67 m above the stillwater level is shown in Fig. 10b). Scanned slide impact profiles are used to calculate the mean slide impact velocity of 110 m/s. The slide profile shows a gentle increase in slide thickness with time to a maximum of 134 m and a fast decay back to zero. The maximum slide thickness of 134 m equals 1.4 times the pre-motion slide thickness of 92 m estimated roughly by Miller (1960). This increase of 40 % in slide thickness is necessary in the model to compensate for the void fraction present in granular flow in order to match the slide mass-flux per unit width. The generated slide length before impact was estimated to 748 m with the mean slide velocity of 110 m/s and slide duration of 6.8 s as indicated by the slide profile in Fig. 1 Ob).

Wavegagerecords

The waves generated by the granulate inflow (Fig. 10b) and recorded with a capacitance wave gauge at location x = 885 m are shown in Fig. 1 la). The wave propagating away from the impact area in positive x-direction creates a sole peak at t = 16 s with a maximum positive amplitude a = 152 m.

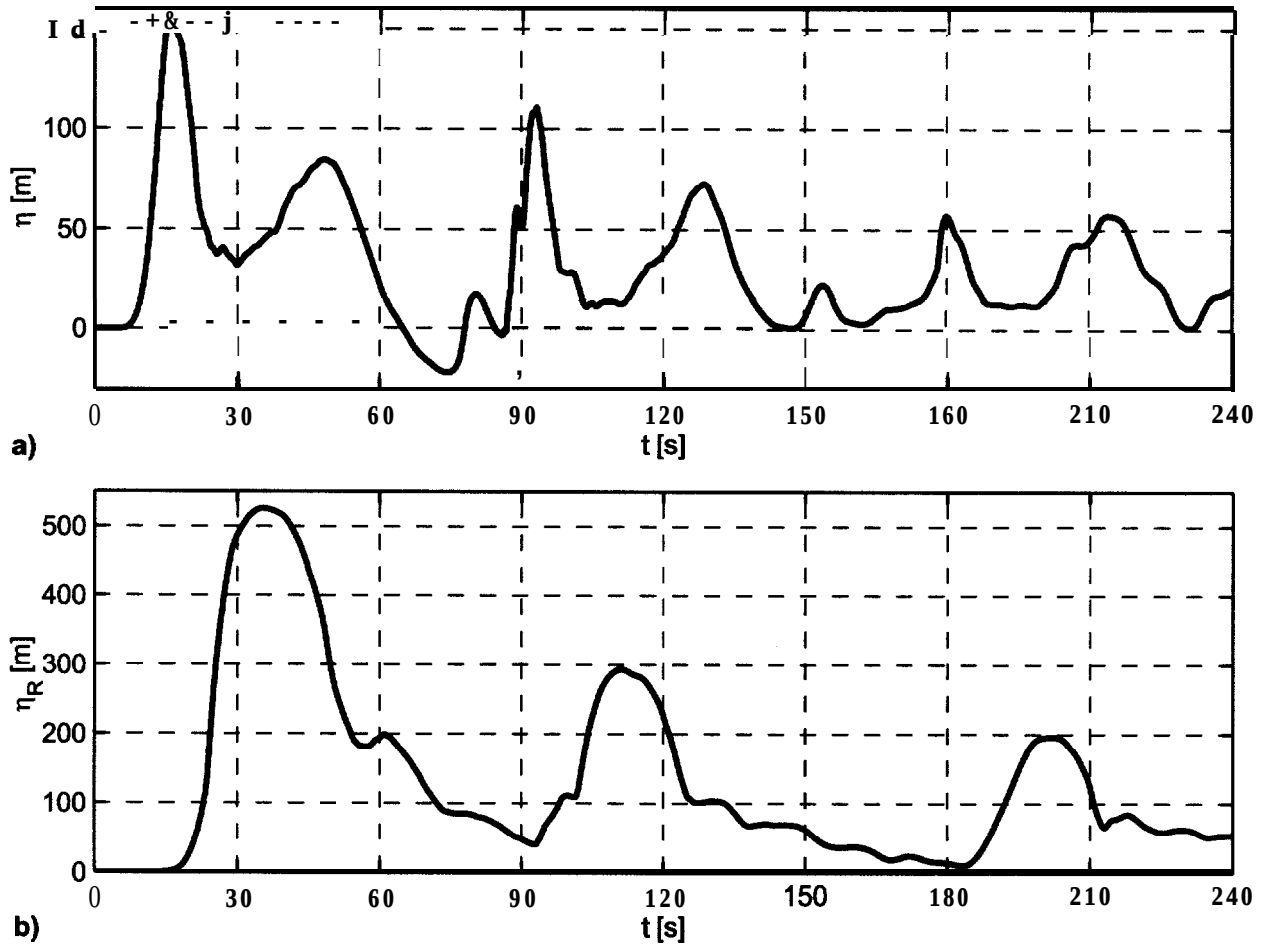

Fig. 11 a) Wave-record at location x = 885 m and **b) wave run-up record** on headland ramp at locations x = 1342 m + η_R measured with capacitance wave gages.

In the two-dimensional model of Gilbert Inlet the single outward travelling wave is reflected back and forth from both headland and rockslide ramps. The main trailing peaks recorded on the wave gauge have altering propagation directions from positive to negative x-direction, respectively. The second peak (a = 85 m, t = 48 s) on the wave record corresponds to the wave reflection from the headland propagating in the negative x-direction. An experiment without the headland ramp showed that the first wave trough (η = 37 m, t = 30 s) is truncated by the reflection from the headland and not fully developed. In the experiment without headland ramp a flat trough with a negative amplitude a = -10 m was recorded behind the single outward travelling wave crest. Therefore the total wave height is estimated to H = 162 m. The measured wave height to stillwater depth ratio H/h = 1.33 is well beyond any breaking criterion (Dean and Dahymple, 1991). The experimental run without headland ramp showed that breaking and transformation to a nonlinear bore initiated roughly at x = 1500 m – after the beginning of the headland ramp at location x = 1342 m. The third main peak (a = 111 m, t = 93 s) and the fifth peak (a = 57 m, t = 180 s) correspond to the wave reflected back from the rockslide slope. The fourth peak (a = 73 m, t = 129 s) and the sixth peak (a = 57 m, t = 214 s) are wave reflections from the headland ramp. This partial back and forth wave reflection in Gilbert Inlet could account for the "jumping and shaking" reported by one eyewitness (Miller, 1960).

The corresponding wave run-up recorded by a capacitance wave gage on the headland ramp is shown in Fig. 1 lb). The run-up gage record acquired parallel to the 45" inclined headland ramp is transformed into an elevation record. The x-location changes proportional to the amplitude according to x = 1342 m + η_R. On the headland ramp a maximum run-up height of R = 526 m is measured at t = 35 s. The measured run-up of 526 m perfectly matches the highest elevation of 524 m on the trimline of forest destruction in Gilbert Inlet. In all experiments a small amount of water overtopped the modeled headland ramp with an altitude of 550 m since the run-up gages drop out when the sheet of water on the headland ramp gets thinner than 5 m. Miller (1960) reported that the water had rushed into the forest some 10 m higher than the highest overturned trees. The two trailing peaks on the run-up record correspond to the first and second back-reflection of the single initial wave run-up. The peak to peak period increases from 76 s to 91 s. This decay in propagation velocity with diminishing wave amplitude is due to the characteristic amplitude dispersion of nonlinear waves.

PIV-measurements

A sequence of twelve instantaneous velocity vector-fields computed with PIV is shown in Figs. 12. Velocity vector-fields from two different experiments are mounted together and overlaid on original PIV-images. The sequence starts at t = 0.76 s after rockslide impact and continues with a time step of 1.73 s covering roughly a time span of 20 s. For this extremely unsteady flow the main advantage of PIV is the capability to quantitatively reveal the instantaneous macro-structure of the flow process within a large area of interest. Instantaneous velocity vector-fields allow insight into kinematics during impulse transfer and wave generation. The whole process may be subdivided into two main stages: a) Slide impact and penetration (Fig. 12a), flow separation (Fig. 12b), cavity formation (Fig. 12c,d,e,f) where slide penetration velocity exceeds wave propagation velocity, and b) cavity collapse (Fig. 12g,h), slide run-out along channel bottom and slide detrainment (Fig. 12i,j,k,l) where the wave overtakes the rockslide and propagates out of the impact area. At the beginning of cavity collapse (Fig. 12g) the wave amplitude exceeds 200 m in elevation at x = 600 m and t = 11.14 before decaying synchronously with cavity collapse to a = 152 m at t = 16 s and x = 885 m (Fig. 1 la). A high velocity gradient at the slide front during impact and penetration causes sediment transport on slide front leading to a pealing effect (Fig. 12b). The three phases – granular material, water and air – are clearly separated along distinct borderlines before flow reattachment occurs (Fig. 12h). Flow reattachment traps a large volume of air in the back of the rockslide (Fig. 12i), which leads to large bubble formation (Fig. 12j), bubble break up and massive phase mixing (Fig. 12k,l). Slide detrainment further increases phase mixing. The granular slide is deformed due to impact and deflection at the channel bottom reaching a maximum thickness and minimum length (Fig. 12d). The slide front forms an almost vertical wall with culminating height at the beginning of the cavity collapse (Fig. 12f,g). Thereafter the slide front thickness decays with slide run-out (Fig. 12j,k,l).

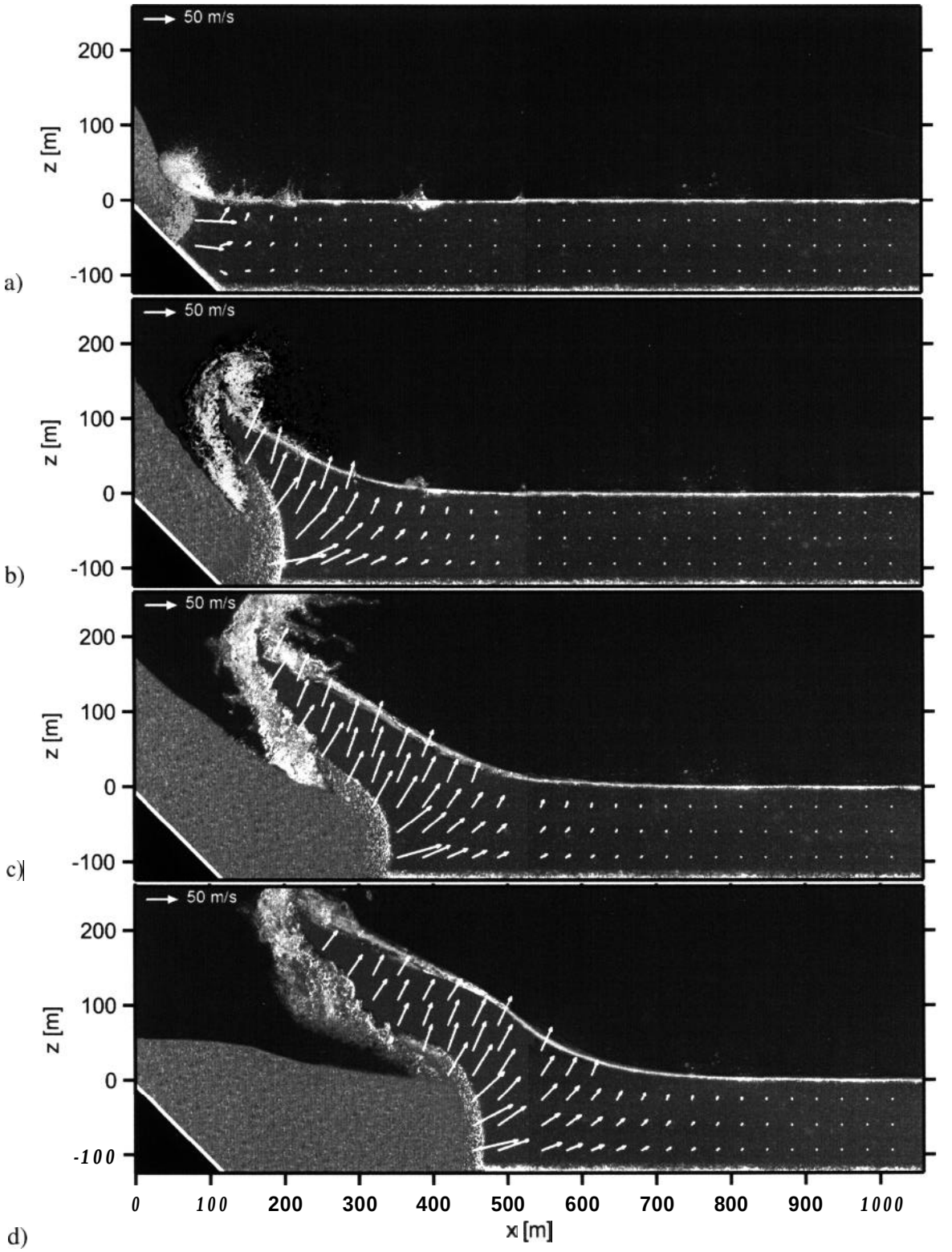

Fig. 12 PIV velocity vector-field sequence of two synchronized granular slide impact experiments with juxtaposed areas of view and up-scaled parameters: **F = 3.18,** v_s **= 110** m/s, m' = 98.5 x 10^3 t/m', h = 122 m, $\alpha = \beta = 45°$, time increment 1.73 s with first image at t = 0.76 s after impact.

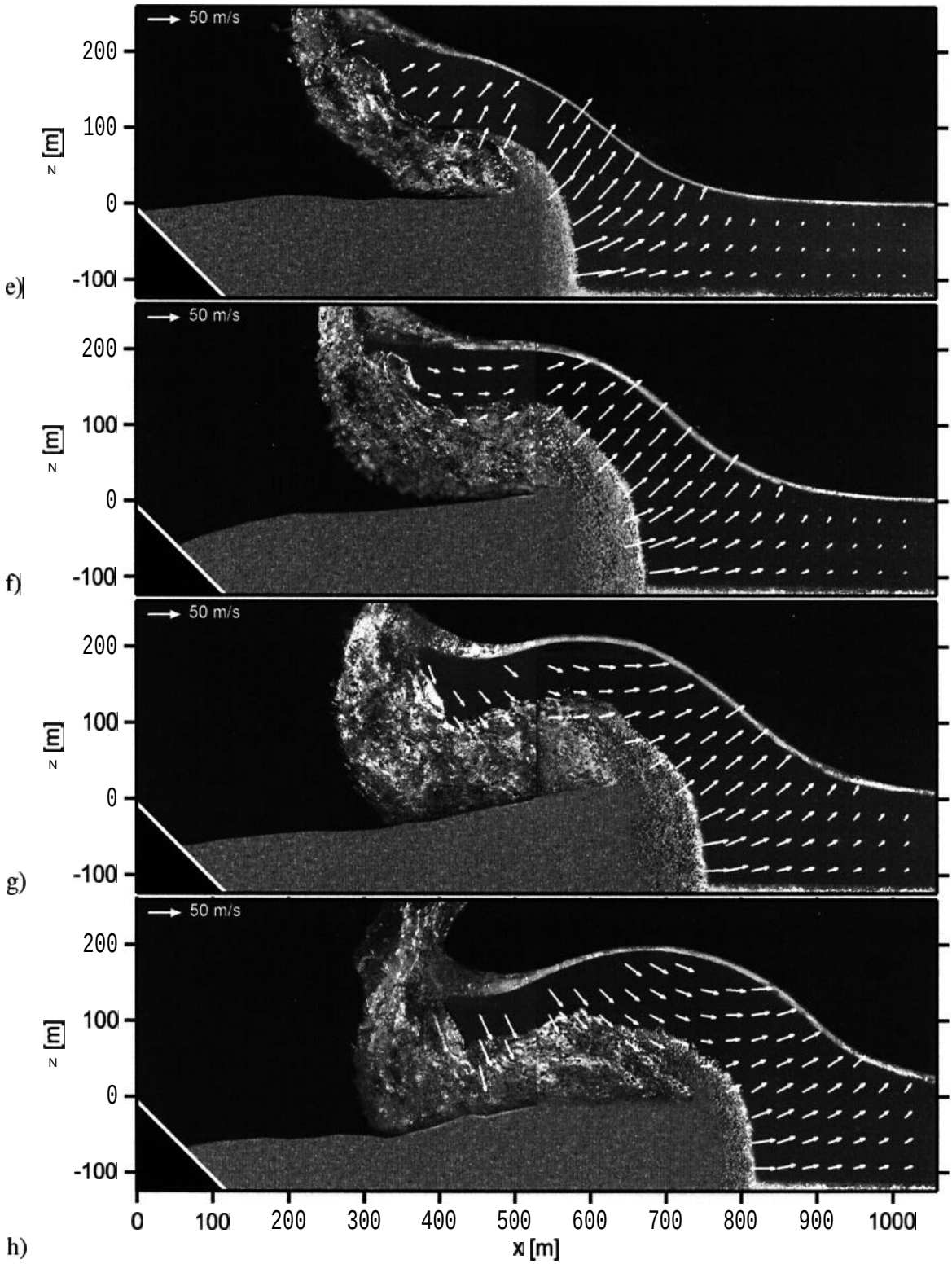

F'ig. 12 PIV velocity vector-field sequence (cont.) of two synchronized granular slide impact experiments with juxtaposed areas of view and up-scaled parameters: **F = 3.18,** v_s = 110 m/s, m' = 98.5 x 10^3 t/m', h = 122 m, a= β = 45° with a time increment of 1.73 s.

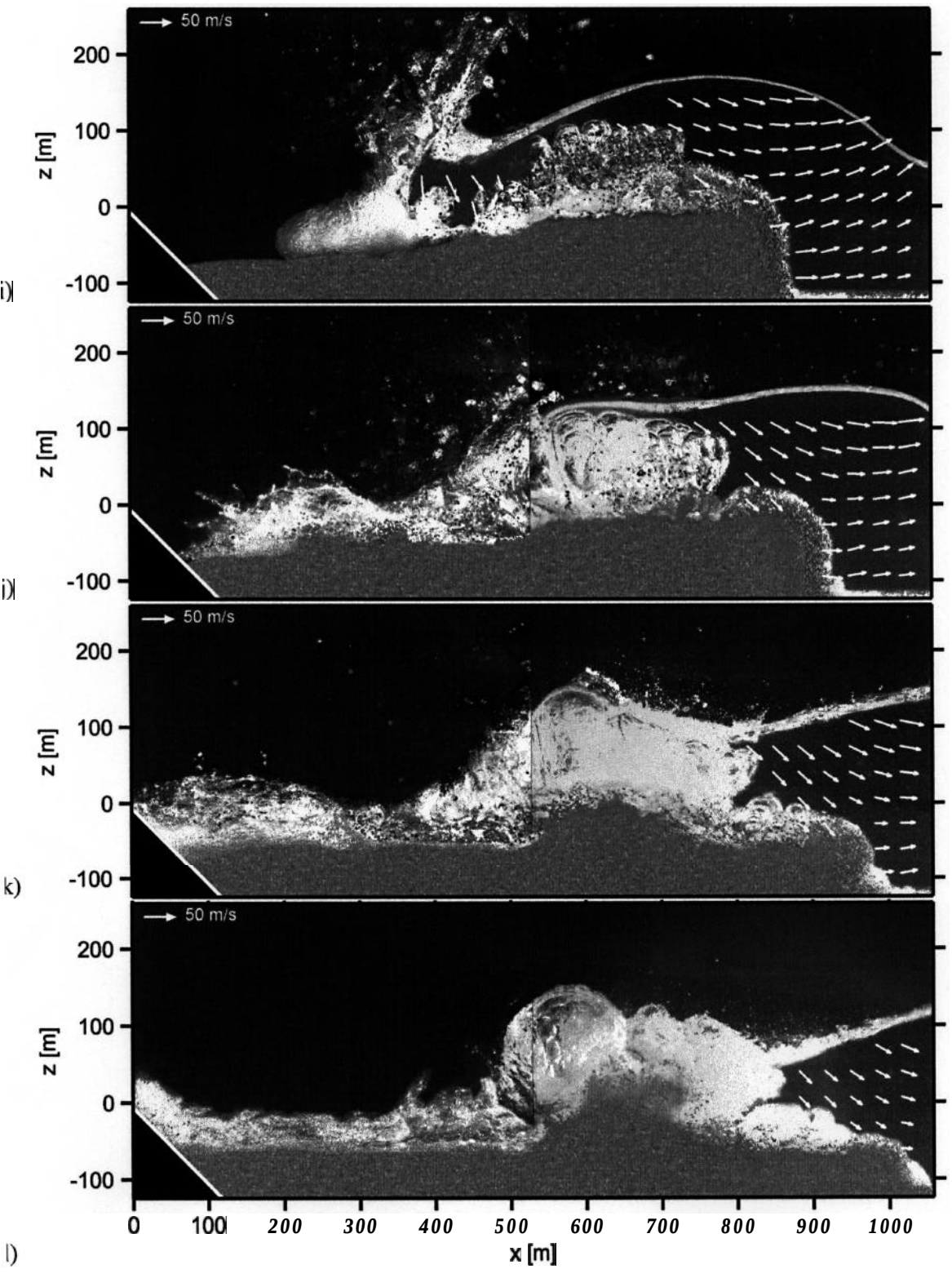

Fig. 12 PIV velocity vector-field sequence (cont.) of two synchronized granular slide impact experiments with juxtaposed areas of view and up-scaled parameters: **F = 3.18,** v_s = 110 m/s, m' = 98.5 x 10^3 t/m', h = 122 m, a= β = 45° with a time increment of 1.73 s.

Due to phase mixing and slide penetration no capacitance wave gage or any other intrusive device could be positioned closer to the impact site than x = 885 m.

A sequence of eight PIV velocity vector-fields acquired during wave run-up on headland is shown in Fig. 13. The area of view begins above the stillwater level. The sequence starts at t = 23.28 s after rockslide impact and continues with a time step of 1.73 s covering roughly a time span of 12 s. At t = 23.28 s the wave is shown prior to plunging onto the headland ramp. The wave amplitude has increased beyond 180 m. In the following images the wave surges up the headland slope with high velocity.

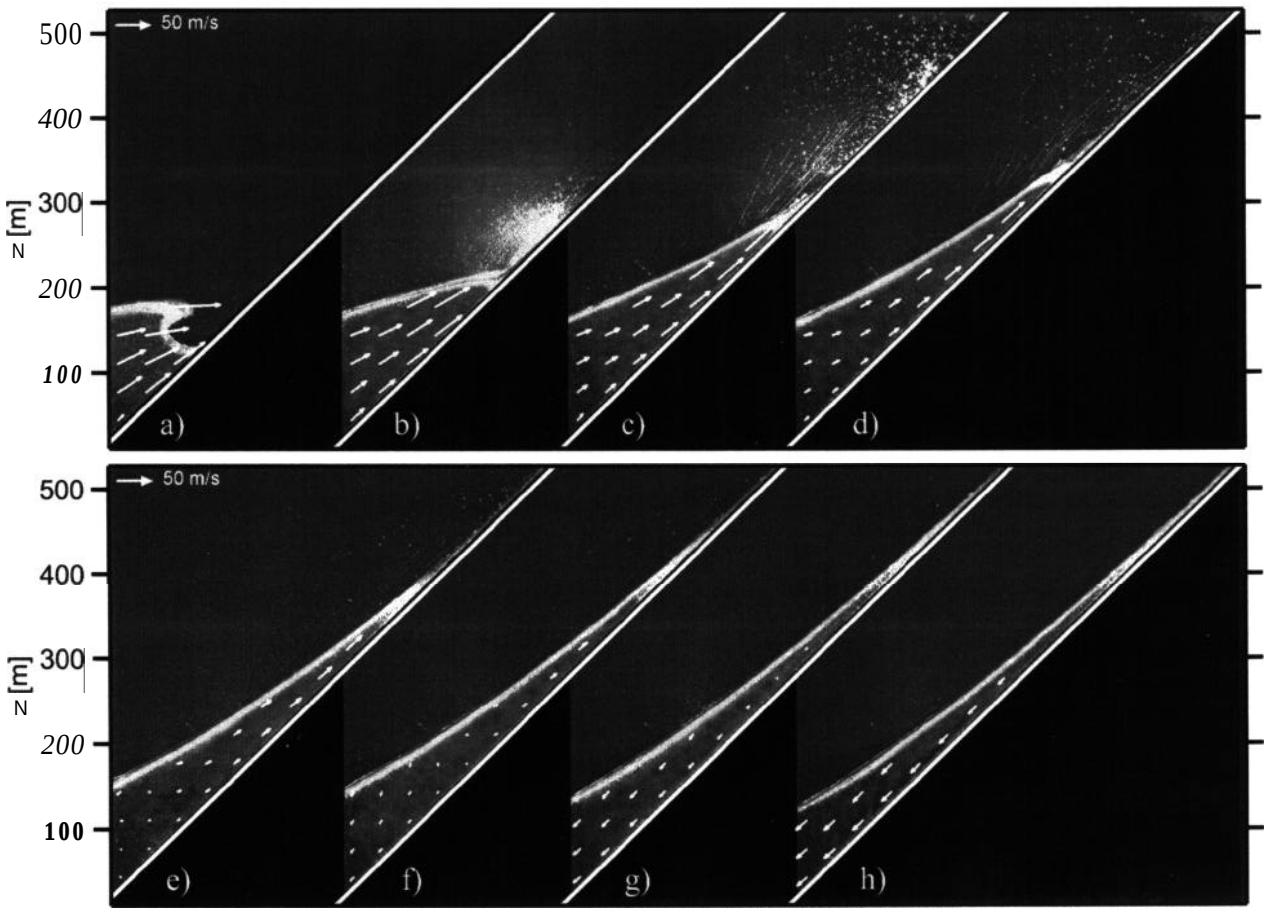

Fig. 13 PIV velocity vector-field sequence of wave run-up on headland slope created by a rockslide impact with up-scaled parameters: **F = 3.18,** v_s = 110 m/s, m' = *98.5 x* 10' t/m', h = 122 m, $\alpha = \beta = 45°$, time increment 1.73 s, first image at t = 23.28 s after impact, lower left image corner at location x = 1353 m and z = 11 m.

At t = 30.2 s (Fig. 13e) a half saddle or an instantaneous stagnation point appears in the lower left corner of the velocity vector-field. The half saddle propagates up the headland ramp phase shifted to the run-up wave front. In the area below the half-saddle water rushes down the headland ramp, whereas above the half-saddle water still surges upward. Therefore the sheet of water located on the headland ramp is already getting significantly thinner at the lower end when maximum run-up height is reached at t = 35 s (Fig. 16h). PIV gives insight into kinematics of wave run-up and complements run-up wave front records measured with capacitance wave gages. A sheet of water only few meters in thickness reaches beyond the image area limited to z = 527 m and is undetectable for the capacitance wave gages due to slim flow depth

of only a few millimeters at laboratory scale. As indicated in Fig. 13 enough water ran-up the headland slope to cause the flooding observed in Lituya Bay as estimated by Mader (1999) with numerical simulations of the whole Lituya Bay.

COMPARISON WITH PREDICTIVE MODELS

Wave generation

Slingerland and Voight (1979) applied several predictive models with empirical formulae to the Gilbert Inlet rockslide. Predicted wave heights scattered more than an order of magnitude exceeding a range from 30 m to 300 m. Some empirical formulas were applied well beyond their range of experiments. An in depth analysis, comparison of different predictive models and their assumptions can be found in Slingerland and Voight (1979). The empirical formula of Huber and Hager (1997) for 2D-impulse wave characteristics

$$H = 0.88 \sin \alpha \left(\frac{\rho_s}{\rho_w} \right)^{1/4} \left(\frac{V_s}{b} \right)^{1/2} \left(\frac{h}{x} \right)^{1/4} \tag{2}$$

predicts a wave height of H = 94 m with a= 45°, ρ_s = 2.7 t/m", ρ_w = 1 t/m^3, V_s = 30.6 x 106 m^3, b = 823 m, h = 122 m and x = 885 m. The Huber and Hager (1997) formula for 2D-impulse wave characteristics underestimates the measured wave height H = 162 m by a factor of 1.8, although F = 3.2 is within the range of experiments conducted by Huber (1980). The impact shapes of Huber's granular rock avalanches were inherently dependent on impact slide velocity. Rough estimations of slide thickness from photos (Huber, 1980) indicate that Huber's slides at comparable impact Froude numbers were thinner than the slide profile shown in Fig. 10b. Sliding block experiments conducted by Noda (1970) and Kamphuis and Bowering (1970) showed a strong dependency of generated wave heights on block-slide impact shapes. The difference in slide impact shape explains why the Huber and Hager formula underestimates the measured wave height.

Wave run-up

The Hall and Watts (1953) empirical formula for solitary wave run-up on an impermeable slope with β = 45" is

$$\frac{R}{h} = 3.1 \left(\frac{H}{h} \right)^{1.15} \tag{3}$$

and predicts a wave run-up R = 526 m with H = 162 m and h = 122 m. The measured incident relative wave height H/h = 1.33 is well beyond the range of experiments conducted by Hall and Watts (1953) with H/h < 0.5. The Hall and Watts data for β = 45" refers to non-breaking waves. The Hall and Watts formula perfectly matches the experimentally measured wave run-up and the observed altitude of forest destruction in Lituya Bay. This confirms the conclusion drawn by Slingerland and Voight (1979) using back-calculation of wave height from run-up that a wave height of about 160 m was necessary to produce the wave run-up in Gilbert Inlet. Synolakis (1987) presented an approximate theory for non-breaking solitary waves. The derived asymptotic solution for the maximum run-up of solitary waves

$$\frac{R}{h} = 2.831 \sqrt{\cot \beta} \left(\frac{H}{h} \right)^{5/4} \tag{4}$$

is valid for $H/h \leq 0.8183 (\cot \beta)^{-9/10}$ and predicts a wave run-up R = 492 m with β = 45°, H = 162 m and h = 122 m. The incident wave with H/h = 1.33 breaks during run-up since $H/h > 0.8183 (\cot \beta)^{-9/10}$. The PIV-sequence in Fig. 13 shows that wave breaking during run-up is initiated but does not fully developed due to the steep slope. The run-up process is more surging than breaking and therefore extrapolations from non-breaking run-up laws may be applied. The observed wave run-up can be calculated using existing empirical and theoretical formulas for non-breaking solitary waves with a sufficient accuracy of 10 %. Müller (1995) investigated wave run-up and dam overtopping mainly for stable intermediate depth waves in the far field of falling blocks. The Müller empirical formula

$$\frac{R}{h} = 1.25 \left(\frac{\pi}{2\beta} \right)^{0.2} \left(\frac{H}{h} \right)^{1.25} \left(\frac{H}{L} \right)^{-0.15} \tag{5}$$

predicts a wave run-up R = 333 m with β = 45°, H = 162 m, L = 1100 m and h = 122 m. The measured incident relative wave height H/h = 1.33 is well beyond the range of experiments conducted by Müller (1995) with $H/h \leq 0.5$. The Müller (1995) formula underestimates the measured wave run-up by a factor of 1.6 and may therefore not be applied outside of its validity range $H/h \leq 0.5$.

CONCLUSIONS

The physical model at 1:675 scale of the Lituya Bay 1958 event includes rockslide impact, wave generation, propagation and run-up on headland. A novel pneumatic landslide generator was used to generate a high-speed granular slide with controlled impact velocity and shape. State-of-the-art laser measurement techniques such as particle image velocimetry (PIV) and laser distance sensors (LDS) were applied to cope with an extremely unsteady three phase flow due to high speed granular slide impact, high velocity gradients, flow separation, cavity formation, wave generation and run-up. A granular slide with density and volume given by Miller (1960) impacting at a mean velocity of 110 m/s generates a large air cavity and an extremely nonlinear wave beyond breaking criterion – but non-breaking before headland run-up. The wave with a wave height of about 160 m is capable of running up to an elevation of about 530 m above mean sea level. The measured wave run-up perfectly matches the trimline of forest destruction on the spur ridge in Gilbert Inlet. Back-calculation of wave height from observed trimline of forest destruction using Hall and Watts (1953) run-up formula equals measured wave height in Gilbert Inlet. Existing formulas for non-breaking solitary wave run-up applied beyond their validity range predict wave run-up heights with an accuracy of 10 %. Existing dimensioning formulas for wave height prediction scatter wave heights over more than an order of magnitude exceeding a range from 30 m to 300 m. Further research on slide impact characteristics, wave generation and energy conversion is necessary. The formation of a large air cavity similar to an asteroid impact as proposed by Pararas-Carayannis (1999) is highlighted. The conclusion drawn by Miller (1960), that the 1958 trimline of forest destruction on Lituya Bay shores was carved by a giant rockslide generated impulse wave, is confirmed by experiments. PIV-measurements in the wave run-up area indicate that enough water ran up the headland slope to cause the flooding observed in Lituya Bay, as estimated by Mader (1999) with numerical simulations of the whole Lituya Bay. Mader (1999) suggests full Navier-Stokes modeling of the Lituya Bay rockslide impact.

ACKNOWLEDGMENTS

The writers would like to acknowledge persona1 communications with Dr. Andreas Huber, Fellow VAW-ETH, Dr. Charles Mader, Fellow LANL, Dr. George Plafker, USGS, Dr. George Pararas-Carayannis,

Hawaii, Dr. Simon Day, UCL, and Dr. Paul Liu, NOAA. The research work presented was supported by the Swiss National Science Foundation, grant number 2100-050586.97 and the Swiss Federal Institute of Technology, ETH Zurich.

REFERENCES

Dean, R.G., Dalrymple, R.A. (1991). Water wave mechanics for engineers and scientists. *Advanced series on ocean engineering* 2. World Scientific, Singapore.

Fritz, H.M. (2001). PIV applied to landslide generated impulse waves. *Laser techniques for fluid mechanics,* selected papers from the 10" International Symposium: Lisbon 2000, Portugal. Eds. Adrian, R. J. et al., Springer, New York. In press.

Fritz, H.M., Moser, P. (2001). Landslide generator. *Pneumatic World.* submitted.

Hall, J.V., Jr., Watts, G.M. (1953). Laboratory investigation of the vertical rise of solitary waves on impermeable slopes. *Tech. Memo. 33,* U.S. Army Corps of Engineers, Beach Erosion Board.

Hart, D. (2000). PIV error correction. *Laser techniques applied to fluid mechanics,* selected papers from the 9" International Symposium: Lisbon 1998, Portugal. Eds. Adrian, R.J. et al., Springer, New York.

Huber, A. (1980). Schwallwellen in Seen als Folge von Bergsttirzen (in German). *VAW-Mitteilung 47,* Ed. Vischer, D., Versuchsanstalt für Wasserbau, Hydrologie und Glaziologie, ETH Zurich.

Huber, A., Hager, W.H. (1997). Forecasting impulse waves in reservoirs. *Dix-neuvième Congrès des Grands Barrages* C31:993-1005. Florence, Italy. Commission International des Grands Barrages: Paris.

Hughes, S. (1993). Physical models and laboratory techniques in coastal engineering. *Advanced series on ocean engineering* 7. World Scientific, Singapore.

Jørstad, F. (1968). Waves generated by landslides in Norwegian fjords and lakes. *Norwegian Geotechnical Institute Publication 79:* 13-32. Norwegian Geotechnical Institute, Oslo.

Kamphuis, J.W., Bowering, R.J. (1970). Impulse waves generated by landslides. *Proc. 12th Coastal Engineering Con.*. ASCE 1:575-588.

Law, L., Brebner, A. (1968). On water waves generated by landslides. *3rd Australas. Conf. on Hydraulics and Fluid Mechanics,* Sydney, Paper 2561: 155- 159.

Mader, C.L. (1999). Modelling the 1958 Lituya Bay mega-tsunami. *Science of Tsunami Hazards* 17(2):57-67.

Miller, D.J. (1960). Giant waves in Lituya Bay, Alaska. *Geological Survey Professional Paper 354-C.* U.S. Government Printing Office, Washington D.C.

Mullet-, D. (1995). Auflaufen und Uberschwappen von Impulswellen an Talsperren (in German). *VAW-Mitteilung* 137, Ed. Vischer, D., Versuchsanstalt fiir Wasserbau, Hydrologie und Glaziologie, ETH Zurich.

Müller, L. (1964). The rock slide in the Vajont Valley. *Rock Mech. Eng. Geol.* 2(3-4): *148-212.*

Noda, E. (1970). Water waves generated by landslides. *J. Waterw. Harbors Coastal Eng. Div.* ASCE 96(WW4):835-855.

Pararas-Carayannis, G. (1999). Analysis of mechanism of tsunami generation in Lituya Bay. *Science of Tsunami Hazards* 17(3): 193-206.

Scarano, F., Riethmuller, M. (1999). Iterative multigrid approach in PIV image processing with discrete window offset. *Experiments in Fluids* 26:5 *13-523.*

Sharpe, C.F.S., 1938. *Landslides and related phenomena.* Columbia Univ. Press, New York.

Slingerland, R.L. and Voight, B. (1979). Occurences, properties and predictive models of landslide-generated impulse waves. Rockslides and avalanches 2:317-397, Ed. Voight, B. *Developments in geotechnical engineering* 14B. Elsevier, Amsterdam.

Stive, M.J.F. (1985). A scale comparison of waves breaking on a beach. *Coastal Engineering 9: 15* l-l 58.

Synolakis, C.E. (1987). The run-up of solitary waves. *J. Fluid Mech.* 185:523-545.

Tocher, D., Miller, D.J. (1959). Field observations on effects of Alaskan earthquake of 10 July, 1958. *Science* **129**:394-395.

Tognacca, C. (1999). Beitrag zur Untersuchung der Entstehungsmechanismen von Murgängen (in German). *VAW-Mitteilung* 164, Ed. Minor, H.-E., Versuchsanstalt für Wasserbau, Hydrologie und Glaziologie, ETH Zurich.

Vames, D.J. (1958). Landslide types and processes. *Highw. Res. Board Spec. Rep. 29. Natl. Acad. Sci.-Natl. Res. Counc. Publ.* **544**:22-47.

Voight, B., Janda, R.J., Glicken, H., Douglass, P.M. (1983). Nature and mechanics of the Mount St. Helens rockslide-avalanche of *18* May 1980. *Géotechnique* **33**:243-273.

Wiegel, R.L. (1964). *Oceanographical engineering.* Prentice-Hall, Englewood Cliffs, N.J.

NOTATION

a [L] = wave amplitude
b [L] = slide width
d [L] = grain diameter
F [-] = slide Froude number
g [LT^{-2}] = gravitational acceleration
h [L] = stillwater depth
H [L] = wave height
l [L] = slide length
L [L] = wave length
m [M] = slide mass
R [L] = wave run-up height
s [L] = slide thickness
t [T] = time after impact
v [LT^{-1}] = velocity
V [L^3] = volume
x [L] = streamwise coordinate
z [L] = vertical coordinate
α [°] = slide impact angle
β [°] = wave run-up angle
η [L] = water surface elevation record
ρ [ML^{-3}] = density

Subscripts

s = slide
g = granulate
R = run-up

Superscripts

= per unit width

COMPUTATIONAL TECHNOLOGY FOR CONSTRUCTING TSUNAMI LOCAL WARNING SYSTEMS-'

L. B. CHUBAROV, Yu. I. SHOKIN,
Institute of Computational Technologies SB RAS,
Academician Lavrentjev Ave., 6, Novosibirsk, 630090, Russia,
E-mail : chubarov@ict.nsc.ru

K. V. SIMONOV
Institute of Computational Modelling SB RAS,
Academgorodok, Kranoyarsk, 630090, Russia
E-mail : lena@icm.krasn.ru

ABSTRACT.

The theme of this work is the method of constructing local systems *(LS)* for early tsunami detecting, based on the results of mathematical modeling. This method suggests fulfillment of the specially organized series of computational experiments, on the results of which the rational network of hydrophysical gages is determined for the particular defended point and nomograms for estimation of the parameters of the wave's influence are calculated on the basis of the data of the operative tsunami registration on the gages. With the help of these nomograms, it is possible to accomplish operative forecast of the degree of tsunamidanger for the particular point in the real time regime with necessary advance time, high security and reliability.

Actual realization of the suggested method was accomplished for one of the harbour on the Kamchatka's coast. On the basis of this work, below there will be demonstrated the main ideas of such method of constructing local systems.

INTRODUCTION.

Depending on the degree of the remoteness from the each defended coast point there are local, regional, and remote tsunami. Thus, Russian Far East coast runs the influence of strong tsunami from the centers of the local zones near Japan, Kuril Islands, and Kamchatka. Transocean tsunami, dangerous for the region, are generated near Alaska, Aleutian Islands, South America. And the biggest quantity of victims and damage is in the areas of the coast zone, located very near the source.

Global and regional monitoring of tsunami in the Pacific region is fulfilled by the International and national departments of tsunami warning, but their work in the most cases is not very effective. We can outline several main factors, which are the reason for the insufficient efficiency of estimation of the event parameters, the reason for the inadequate exactness of local forecast, of significant loss from false alarms.

Regional systems can not provide reliability of the forecast of tsunamidanger from local underwater earthquakes, when the part of the coast and adjoining water area are covered by tsunamicenter zone, because the minimum period of time of tsunami wave running in this case may not exceed 5 minutes, during which traditional system with its hierarchical structure does not have time to react. We can mention, that normative period of time for estimation of the main tsunami parameters in regional and international tsunami warning systems is 20-30 minutes since the earthquake occurs.

Depending on the factor of advance time the significant part of the Pacific coast of Kamchatka and some areas on Kuril Islands are «extreme» for the department of tsunami warning. For the Russian Far East coast the minimum period of time of tsunami wave running from the main tsunamigenic areas in Japanese Sea is 30-35 minutes. And general situation in this region is more favorable.

Insufficient efficiency of the regional departments of tsunami warning became apparent, in particular, with earthquakes, occurred on the 29th of January in 1975 on Hawaiian Islands, on the 1 6th of August in 1976 in Philippine Sea, on the 26th of May in 1983, on the 12th of July 1993 in Japanese Sea and on 5th of November in 1994 on South Kuril Islands, which caused large damages and human victims. In the table 1, there are shown indices of activity of the department of tsunami warning for Russian Pacific coast for the last 35 years.

Table 1

Tsunamicenter's location	Events in all	Dangerous events	False alarms	Omission of tsunami
Pacific ocean (in general)	90	15	33	3
Kuril–Kamchatka zone	48	11	18	2
Suburban seas of Far East	10	2	2	1
Remote seismoactive zones	32	2	13	0

The alternative to the regional systems, which allows to decrease the burden of consequences of marine natural calamities and to provide the safety of especially important objects, such as, for example, seaside nuclear electric power stations, is the construction of local systems of early tsunami detecting. The crucial moment here is the defense of the particular coast and water areas, special objects and hydrotechnical buildings.

At the same time, we can consider local peculiarities of bottom and land contour, typical behavior of wave process near the defended coast. Localization of the defended area allows to

decrease significantly the period of time, necessary for taking the decision, and to increase the exactness of the forecast, almost to exclude false alarms. Economic efficiency of such systems in comparison with regional centers is evident.

Stated above considerations are confirmed by analysis of the experience of departments of tsunami forecast, organized on the principles of divided system of gathering and analyzing information. This analysis showed impossibility of providing the necessary advance time with local tsunami, even with the use of the mostly modern means of telemetry and telecommunications.

The necessity of increasing effectiveness of the forecast leaded to the construction of the local systems. The first of them was expanded in Japan () on the Suruga gulf coast, where after strong underwater earthquake tsunami wave can reach the coast within 4-5 minutes. For the timely warning, the special monitoring system, consisted of 4 seismographs, measuring soil acceleration, is expanded on the city's territory. Three levels of seismic signal, corresponding to the particular threshold meanings of acceleration, operate in turn with efficient tsunami warning.

An attempt of constructing the automated system of early tsunami warning for the coast of Chile was executed in the frame of American-Chilean project THRUST [2], the basis of which is the use of satellite communications channel for transferring the signal. The leading «forecast» parameter here, as in the other LS (for example, Shizuoka [1], Hawaiian Islands [3] and Tahiti Island [4]), is the size of soil acceleration, measured in specific points.

Efficiency and reliability of such systems are determined only by the principle of choosing the threshold meanings of soil movement acceleration during the earthquake. An apparent disadvantage of this approach is limitation of the set of controlled seismic parameters, on the basis of which the forecast is fulfilled. Including even minimum quantity of hydrophysical data in this set will allow to increase sharply reliability and exactness of the efficient forecast.

The suggested conception of projecting the local systems on the basis of the results of computational experiments allows to develop the main components of such systems, including the scheme of rational network of hydrophysical gages, tables of coefficients of waves acceleration from the tsunamigenic zones till the tsunami detecting gages and till the defended points, nomograms, necessary for the estimation of tsunami influence.

The advantages of this conception are the possibility to consider typical features of bathymetry, fixation of on-site data about historical earthquakes and tsunami to the defended point, autonomy of the process of monitoring and analyzing the data, reliability of means of event registration and transferring the information, guaranteed advance time of taking the decision about tsunami alarm.

1. STRUCTURE AND STAGES OF PROJECTION OF LOCAL SYSTEM OF TSUNAMI WARNING.

Actual local system's working-capacity is determined by quality of disposition of hydrophysical gages and by the authenticity of the calculated nomograms. So, there are needed maximum account of available historical on-site data about features of wave behavior in examined water area and possibility of efficient and adequate reproduction of the event with the help of flexible and adjustable computational models.

The structure of developed LS expects the presence of hydrophysical gages for estimating the tsunami waves' parameters and control center for gathering and analyzing data, transferring information and fulfilling the procedure of taking the decisions. The scheme of the technology of constructing LS and its functioning is shown in the table 2.

Table 2.

Stages	1. Gathering data	2. Analyzing data	3. Taking: decision
«planning»	Systematizing on-site data. Computational experiment.	On-site experiments. Making nomograms and scheme of gages' disposition.	Developing the plan of measures, providing the safety of objects.
«real» time	Accepting and analyzing hydrophysical signals.	Estimating the time of running, amplitude and the period of incoming wave.	Estimating the limits of the flooding zone, the strength and time of the influence. Fulfilling the plan of measures.

Local system can work in two regimes: in regime of waiting the event and in operative one. In the waiting regime the unfavorable event, the control over the sea level in near and far water area's zones is fulfilled with the help of hydrophysical stations. When detecting on one of the gages abnormal changing of stationary condition of the sea level the system start working in operative regime. After that the parameters of wave, waited in the place of an object, are estimated. On basis of the analysis of gotten data with the help of calculated tables and nomograms, there is taken the decision about possible maximum limits of the flooding zones of the defended part of the coast and of draining of the bottom of the adjoining water area, it is notified about tsunami alarm and about tsunami waves' possible strength and duration of its influence on coast and buildings.

Calculation of the parameters of particular LS consists of several stages, each of which is fulfilled in its calculation zones, which appear to be enclosed telescopely in each other. And with depth of their enclosure the degree of their detalisation increases. They can be named symbolically as «ocean», «region», «local water area)), ((protected water area)).

On the *first* stage (calculation zone – «ocean»), there are calculated maps of waves' running from remote sources. On the basis of analysis of these maps, there are determined main directions of tsunami waves' route to the zone «region».

The work on the *second* stage (calculation zone – «region») means more exact definition of time of wave's running to the defended point with use of more detailed bathymetry; determination of the optimum scheme of disposition of hydrophysical gages of tsunami warning; gathering, systematizing and analyzing historical on-site data about underwater earthquakes and tsunami in studied area for estimation of the parameters of «project» tsunami waves; modeling wave regimes, caused by revealed sources. By the results of calculations, fulfilled on this stage, it is possible to estimate maximum amplitudes and prevalent periods, to compare calculated and on-site data and, finally, to determine the most dangerous centers of possible underwater earthquakes (their disposition and structure).

The aim of the *third* stage is calculation of the coefficients of waves' strengthening with their spreading from the Local system's monitoring gages till the defended point. Initial material for the fulfillment of this work are the results of calculation of waves' transformation (in zone «local water area))), having hydrophysical characteristics (amplitude, frequency, configuration), determined at the previous stage and connected straight with the studied water area and with its possible tsunamigenic zones.

The *forth,* last, stage is fulfilled for the particular part of the coastal zone (((protected water area))) and includes calculating the limits of the flooding zones from the «project» tsunami waves; estimating the engineering risk for the objects, situated in the coast zone; making the resulting nomograms for taking the decisions.

2. ESTIMATION OF THE CHARACTERISTICS OF TSUNAMIGENIC EARTHQUAKES AND TSUNAMI BEHAVIOR IN THE SOUTH PART OF KAMCHATKA.

The high level of seismic activity in south part of Kamchatka, including Avachinsky bay, is well known (Fig.1, 2). The structure of the earth's crust in this region and peculiarities of the structure of focal zone initiate catastrophical tsunami.

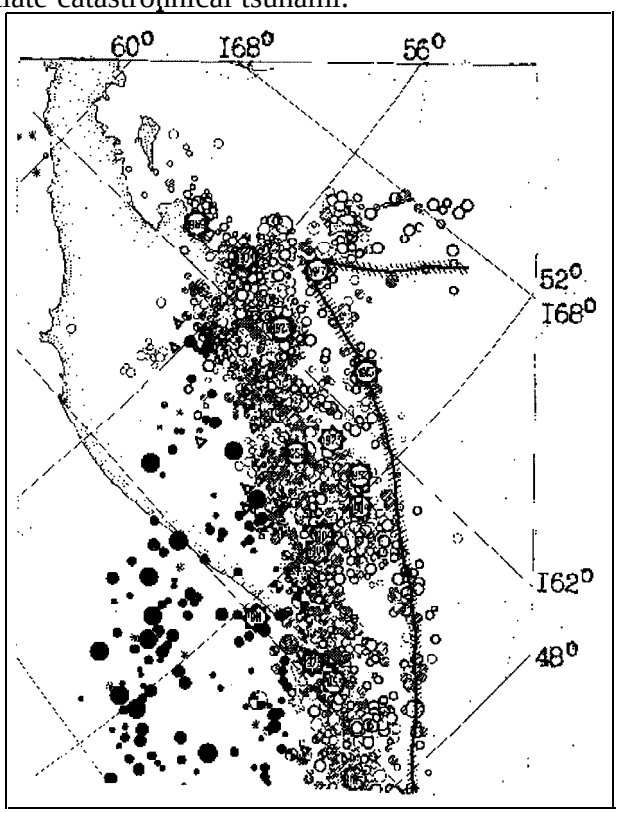

Figure 1. The scheme of seismoactive zones of Kamchatka.

Analysis of data, gotten during zoning Kamchatka's seismoactive zone by the level of tsunamigenic [5], allowed to estimate recurrence of strong earthquakes, able to initiate intensive and catastrophical tsunami, and to make the scheme of zoning, showing zones with different recurrence of such events. Selection of zones of mostly overflow-shear and overfault-shear earthquakes allowed to make the conclusion that par-axial part of the chute is zone, where tsunami of tidal character are formed. At the same time, intensive tsunami of tidal character are mostly possible in zone of deep-water trench.

In the last 250 years for the south part of Kamchatka there are known six earthquakes, which initiated intensive tsunami in 1737, 1792, 1827, 1841, 1904, and 1957 years and three earthquakes, which did not initiate strong tsunami in 1792, 1899, and 1959 years. According to the determined recurrence here within the pointed period of time should happen 9 strong earthquakes. Long-term forecast of strong earthquake in the area of Avachinsky bay, theoretical bases of which were developed in [6], tits such estimations. If to decrease the criterion of intensity of studied tsunami waves, it is possible to say that Kamchatka's coast was flooded 20 times by tsunami waves within the last 250 years [7]. And for all that, noticeable tsunami with the height of raising the level in coastal zone for more than 0.5 m appear here each 10 years, in average. This circumstance predetermines the urgency of fulfilling the measures of defending Kamchatka's coast from tsunami.

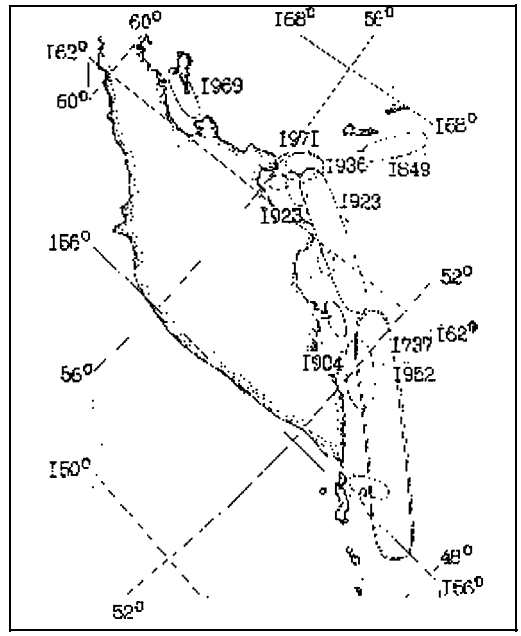

Figure 2. The map of tsunamigenic zones for Kuril-Kamchatka region.

The first numerical estimations of tsunami waves' height in various points along the Pacific coast of Kamchatka were gotten in the work [8] and formed the first Tsunami atlas [9]. And though this Atlas is used by Tsunami Warning Centers for more than 20 years, preliminary character of these estimations is evident. The subsequent refinement of the estimations of tsunami waves' height was carried out in a number of works [10].

Typical for many points dispersion of calculated data is connected with difference in ways of description of tsunami sources and in detail of digitization of underwater relief, with use of simplified mathematical models.

Carried out till the present moment 2D calculations allow to get more detailed data about the distribution of tsunami's height along the Pacific coast of Kamchatka [11]. At the same time, the role of on-site data about tsunami's behavior on the coast is determinant for estimating the quality of carried out computational experiments regarding modeling of the generation and spreading of tsunami waves in particular region.

In tables 3,4, there is represented information about tsunami waves' behavior, observed in Avachinsky bay, shown the character of secondary effect of underwater earthquakes, depicted the damage from tsunami in some points.

The problem of structure of continental slope of Eastern Kamchatka is very important in the problem of tsunami, because the transformation of the long waves is determined actually by the underwater relief.

The results of studying this area's morphology are stated in the work [12]. The main morphostructural elements of bays' bottom of Eastern Kamchatka are deep-water canyons. Such element for Avachinsky bay is Avachinsky canyon with many branches.

An attempt of tsunamizoning of Kamchatka's harbours-fiords on the basis of morphological characteristics, the results of which confirm the conclusion about the high degree of tsunamidanger for the harbours, adjoining to Avachinsky bay, was made in the work [13]. Fiord harbours on the eastern coast of Kamchatka are the reliable shelter from wind waves for ships, therefore the study of long waves' influence on water areas and coast of these harbours is very important.

Table 3. Secondary effects of strong underwater earthquakes in the area of Avachinsky bay.

The date of the event	Description
1737, August, 17, M = 8.25	Strong earthquake lasted about 15 min., people could not stand on feet, in 20 min. There rushed tsunami waves with the height of 6 m up. Before coming of the third wave, there was observed very big sea ebb. After 15 min. there came destroying wave, which changed coastal relief, in the area of swamped lowlands there were formed creeks.
1792, August, M = 8.25	Strong earthquake was felt in P.-Kamchatsky, water in Avachinsky harbour rose in waves as in steam boiler.
1827, August, 9	«Sea in the bay went back very far», earthquake was followed by volcanic activity.
1841, May, 18, M = 8.0	Strong earthquake in P.–Kamchatsky. Some cliffs near the port were demolished. The strong choppiness was observed in the bay.
1848, June	Earthquake near P.–Kamchatsky, water in Avachinsky bay was raising and falling. It drained the bottom of the bight.
1904, June, 26, M = 8.1	Strong earthquake in P.-Kamchatsky, ground was shaking under peoples' feet. On the coast of Avachinsky bay stone blocks were falling into the water, on the surface of the bay there appeared billow, which gushed on the coast.
1952, November, 5, M = 8.25	Very strong earthquake, in 18–40 min. there came tsunami waves, which caused catastrophical damage, changed coastal relief.
1960, May, 23, M = 8.5	Strong earthquake near Chile coast, catastrophical tsunami was formed, large damages in the coastal zone of Avachinsky bay.

3. CALCULATION OF THE PARAMETERS OF LOCAL SYSTEM OF DEFENSE FROM TSUNAMI.

In this paragraph, the results of modeling the spreading of long waves like tsunami in the water area, adjoining to the studied part of coastal zone, are represented. At all that, the possible influence of tsunami waves, generated by three types of sources – remote, regional and local, on the specified part of the coastal zone was taken into the consideration. In accordance with the type of the source there were observed differently scaled calculation zones. Computational experiments, discussed here, we may divide into two groups.

The purpose of *the first* one was to determine the time of wave's running from Aleutian – Alaskan, South American and others well-known tsunamigenic zones and to estimate the conditions of tsunami waves' reaching the coast of Kamchatka. In these calculations for modeling remote tsunami the zone OCEAN was used (net step $A = 1^{o}$), and for modeling regional tsunami the zone OKHOTSK was used (net step A = 6', Fig. 3).

Two additional zones were also used: zone NORTH, including water areas of south part of Kamchatka and north group of Kuril Islands, and zone CENTER, including the central part of eastern coast of Kamchatka, water areas of three adjoining to it Kamchatsky bays (Avachinsky, Kronotsky, and Kamchatsky), part of the water area of Bering Sea and Komandorskie Islands (net step A = 5000 m and 10000 m accordingly).

The *second group* of calculations was carried out for the calculation of waves' amplitude characteristics and for the estimation of coefficients of strengthening. For this purpose three

calculation zones were used telescopely enclosed in each other, KAMCHATKA, AVACHA, and HARBOUR.

Basic zone KAMCHATKA (with maximum depth H = 7600 m, minimum depth – 10 m, and net step A = 4000 m, dimension 80*80, Fig. 4) includes significant elements of underwater relief of the area from c. Lopatka till c. Shipunsky.

Zone KAMCHATKA includes large-scaled part of water area of Avachinsky bay AVACHA (dimension –137* 139, grid step A = 1250 m, Fig. 5). Zone HARBOUR (H = 80 m, A = 75 m, dimension – 150*141, the fragment of this zone is depicted on the Fig. 6), in its turn, is appeared to be enclosed in zone AVACHA.

Table 4. The damage from tsunami waves on the coast of Avachinsky bay.

The date of the event	**Description**	**Estimations of maximum tsunami waves' height for some points in meters calculations forecast on 100 years [13,14]**	
1737	People and buildings were washed off the coast in the area of the bay.		
1841	Brig «Okhotsk» was torn off and taken away on the middle of Avachinsky harbour, buildings were washed out in vill. Ostrovnoe.		
1904	Big wave, when reached the harbour's coast, threw boats on 60 m far inland away.		
1952	st. Morzhovaya – one house is destroyed, boats are thrown away on the coast; vill. Nalychevo – 14 houses are destroyed, people perished; vill. Khalatyrka – 5 buildings were destroyed, people perished; c. Besymyanny – 2 houses were washed away.	11.4	8.6
	st. Sarannaya – the spit with buildings was washed away.	14.8	
	st. Zhirovaya – almost all buildings on the spit were washed away.	14.5	
1960	st. Morzhovaya – 2 houses were destroyed.	14.0	18.1
	st. Vilyuchinskaya – 20 buildings were destroyed, various supplies are washed away.		
	st. Russkaya – various supplies are washed away.	15.5	

The all three calculation zones have mutual control points, located on the sea border of the zone HARBOUR. In such a way there is fulfilled natural transition to more detailed description of water area. And it improves the detail of the carried out calculations and exactness of gotten estimations. Determination of kinematic characteristics (calculations of the first group) was fulfilled

on the basis of ray-path theory of waves' spreading in the heterogeneous medium with the help of algorithms, described in [16].

Amplitude characteristics of waves (calculations of the second group) were determined in the open ocean on the basis of linear equations of shallow water with the help of system of programs MKUR, described in [16]. Calculations in small water area HARBOUR were carried out also on the basis of linear equations of choppy sea [17]. Additional research of ripple effects inside the small water area were carried out on the basis of nonlinear- dispersing model [18].

Figure 3. Calculation zone OKHOTSK.

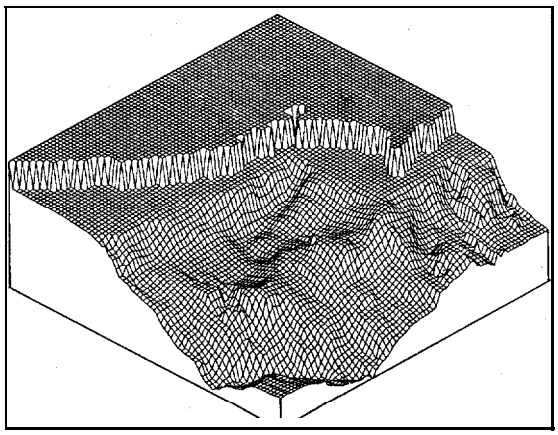

Figure 4. Calculation zone KAMCHATKA

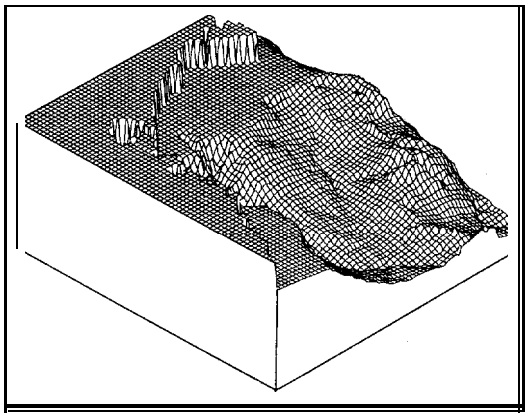

Figure 5. Calculation zone AVACHA.

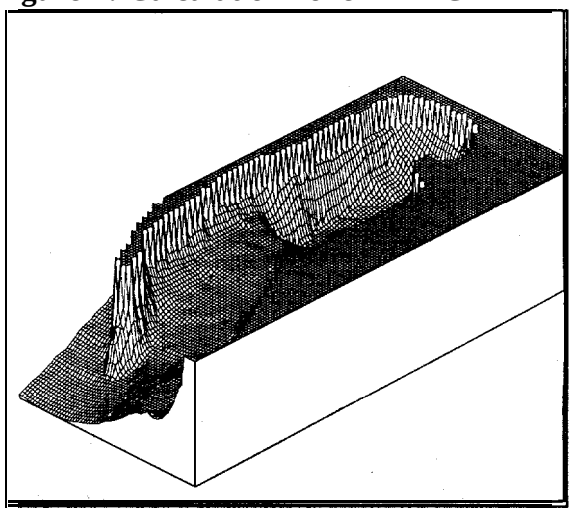

Figure 6. Calculation zone HARBOUR.

For the development of the scheme of rational disposition of gages of early tsunami detecting it is necessary to estimate parameters of advance time and to determine the directions of wave's front movement to the defended water area from tsunamisources of different type. With this purpose there were fulfilled calculations of leading wave's fronts' movement from dot and spatial tsunamisources. In determination of source zones when modeling tsunami there were used known data about tsunamigenic earthquakes in Pacific ocean and historical data about strong local earthquakes of the last century.

Analysis of the results showed that remote and regional tsunami move to the defended local water area KAMCHATKA or AVACHA, accordingly, at strictly determined angles to the direction North-South (S – N). Thus, the waves, moving from the north of Kamchatka, from the Bering Sea, Komandorskie Islands, Aleutian-Alaskan tsunamigenic zone, are running at an angle of 135^{o}, from the areas of tsunamigenic zones of the Pacific eastern coast – at an angle 0^{o}–30^{o}, and southern tsunami, including those that are caused by Kuril and Japanese underwater earthquakes – at angle 45^{o}–60^{o}.

The wave front runs to the defended small water area HARBOUR at an angle, which does not depend on the location, configuration and size of the source. The main front's direction is formed at the top of the canyon at the depth of 200 – 1000 m. The direction of the wave movement to the defended part of the coastal zone is also strictly determined by the configuration of underwater relief and does not depend on the conditions of wave's coming to the zone HARBOUR. General time of tsunami wave's spreading in the zone is T_d = 15 min., and its way to the specified point T_1 = 12 – 13 min.

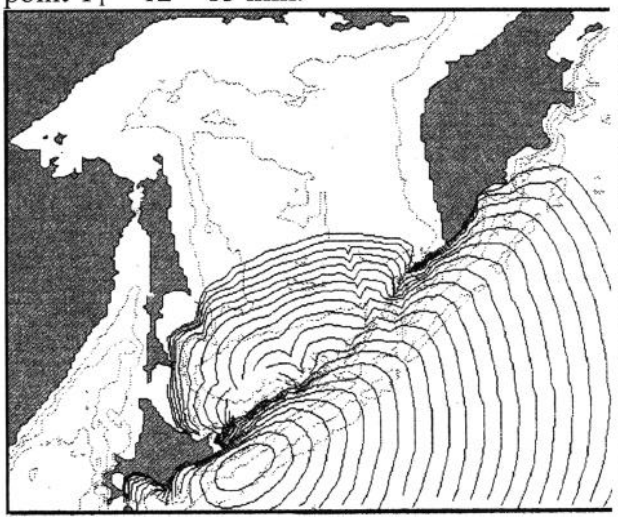

Figure 7. Calculation zone OKHOTSK. The spreading of tsunami from South-Kuril tsunamigenic zone.

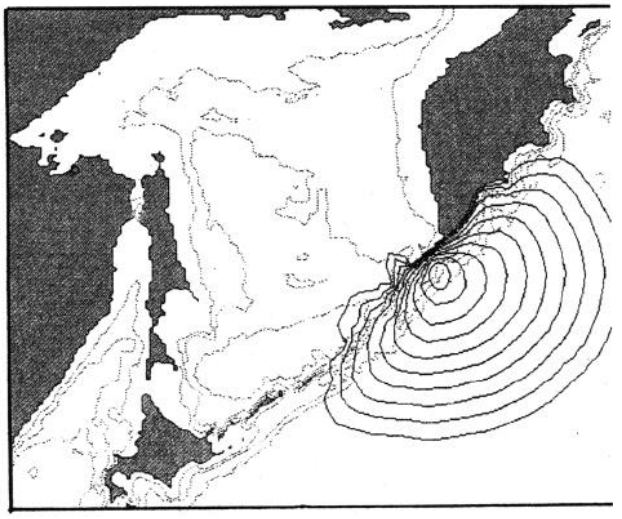

Figure 8. The spreading of tsunami from North-Kuril tsunamigenic zone.

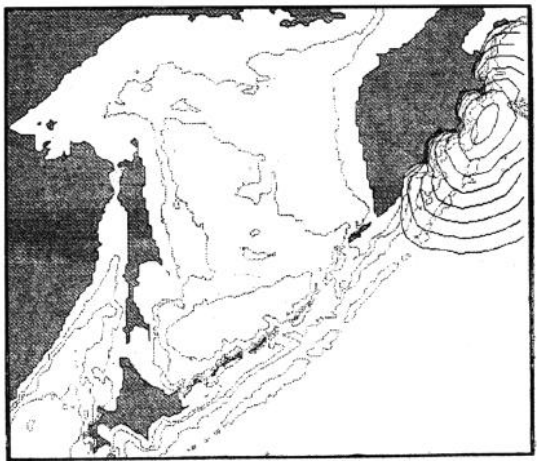

Figure 9. Calculation zone OKHOTSK. The spreading of tsunami from the sources in Kamchatsky bay.

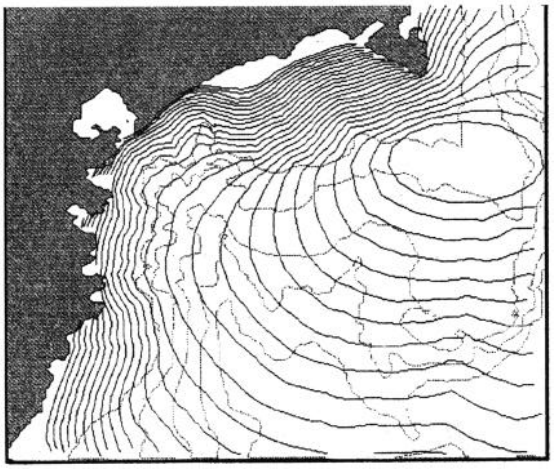

Figure 10. Calculation zone AVACHA. The spreading of tsunami from the sources near c. Shipunsky.

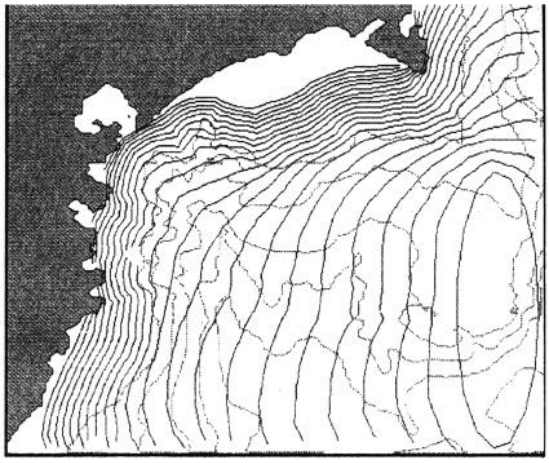

Figure 11. Calculation zone AVACHA. The spreading of tsunami from the sources in the area of continental slope.

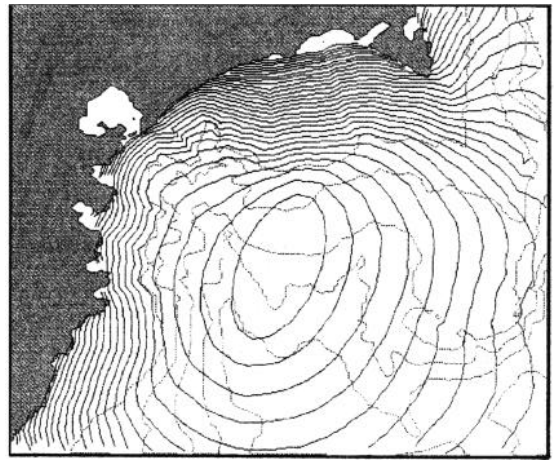

Figure 12. Calculation zone AVACHA. The spreading of tsunami from the nearest source in the area of Avachinsky canyon.

With placing the gage of early tsunami detecting on the top of corresponding canyon at a depth of 1000 m (if place the gage at the big depths, it may turn out that it is put in the center zone of strong local earthquake), the time of tsunami spreading from it till the entrance in the zone HARBOUR is T_2 = 8 min., and it depends little on the gage's moving along the canyon's axis from depths of 200 – 2000 m (T_3 = 1 – 2 min.).

Thus, placing the first main gage (N_4) in the top of the canyon (numeration of the gages is through – from North to South, Fig. 13), it is possible to provide necessary size of advance time parameter $T_3 = T_1 + T_2 > 20$ min. and to fulfill the terms «not to miss tsunami». If to consider the time of coming of the wave's amplitude maximum, the size of parameter T_3 will increase on 1/4 of the wave's period, what in case of strong local underwater earthquakes is 4 -5 min. Gotten low estimation T_3 = 20 min. is in good accord with on-site data about the time of tsunami waves' running under real events. Analysis of time of waves' running, calculated for the global zone OCEAN and regional zones OKHOTSK, CENTER, NORTH, including zones KAMCHATKA and AVACHA, showed that the gage, located in the water area, adjoining to c. Shipunsky, will defend the specified point from the remote tsunami waves, beginning from the northern and till the south-eastern direction of wave's movement.

Thus, the natural location of the second main gage (N_2) is zone with depths of about 100 m in the area of the northern border of Avachinsky bay – cape Shipunsky. Difference of the time of wave's running from the gage N_2 to the gage N_4 is 10 -15 min. for the gages, located in the northern and north-eastern areas of the AVACHA zone. For the waves, moving from the east, this difference decreases till 5 min. The gage in the area c. Shipunsky does not defend this water area from tsunami waves of eastern, south-eastern, and southern directions, running to Avachinsky bay, and it also does not defend coast from the local tsunami with sources, situated further south than c. Shipunsky.

Another elements of local system of early tsunami warning are three azimuth gages – northern one (N_1), disposed near the gage (N_2) and controlling tsunami waves' movement from north and north-east; two gages in the water area of Avachinsky bay at the depths 1000 – 2000 m: eastern (N_3) and southern (N_5) ones, controlling corresponding directions.

Thus, the whole studied zone AVACHA is divided into five sectors, connected with main directions of possible wave's coming on the local system's gages. Advance time parameter T_3 for the defended point, determining time for the fulfillment of alarm measures, changes from 35 min. for the northern till 20 min. for the southern and eastern directions of waves' running.

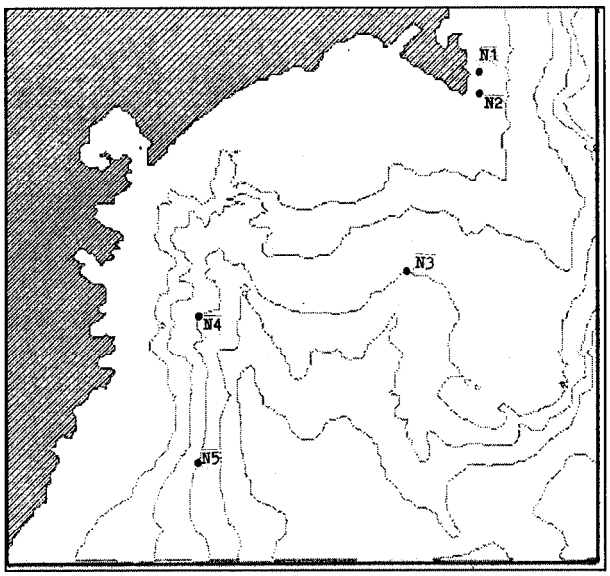

Figure 13. The scheme of disposition of Local system's gages.

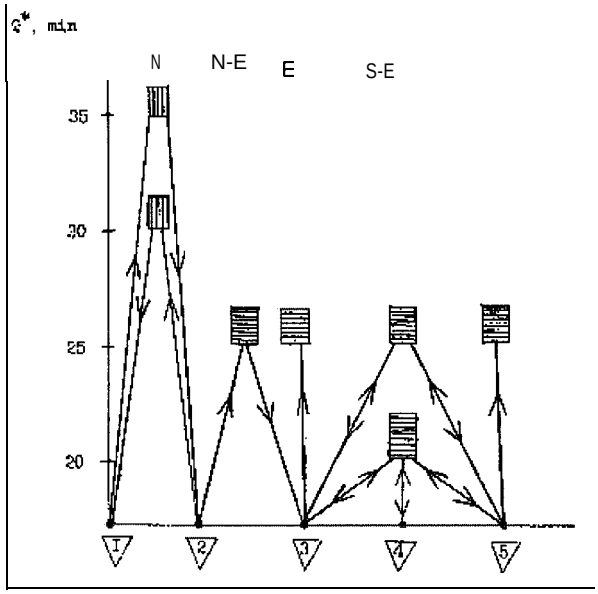

Figure 14. Scheme for the estimation of advance time parameter depending on the order of waves' coming on the gages.

Natural warning about possible coming tsunami, after which it is necessary to redouble monitoring over the sea level, is the degree of feeling earthquake in the area of defended point. It is possible to get notification about strong underwater earthquake in other regional zones from the corresponding departments of tsunami warning. In taking the decision about tsunami alarm two gages take part as a rule – main and azimuth. In accordance with the order of wave's registration on these gages, advance time parameter is estimated (scheme in Fig. 14). Then efficient forecast of tsunamidanger for the defended water area is developed according to the size of registrated sizes of leading wave's amplitude A_i and its period T_i (i is the number of main gage) with the help of corresponding calculation nomogram.

The choice of nomogram is determined depending on the direction of wave's movement with the help of the same scheme. Because the gage N_2 controls northern and north-eastern directions of wave's movement, the degree of danger from the northern tsunamisuorces in Kamchatka and from tsunamigenic zones in the area of Aleutian Islands and Alaska will be determined by *Nomogram I.* Waves from the tsunamigenic zones, located along the Pacific eastern coast, and also from tsunamisources in the area of Kuril Islands and Japan, are registrated by the gage N_4. In this case it is necessary to apply *Nomogram II.*

For the actual realization of the suggested structure of LS and construction of *Nomogram I* and *II,* there were carried out series of computational experiments for calculation zones KAMCHATKA, AVACHA, and HARBOUR. Calculated mareograph point on the sea border of the zone HARBOUR (hypothetical gage (N_5)) was the connecting one in these calculations. Calculated mareograms in this point served for recalculation of the coefficients of intensification from the zones KAMCHATKA and AVACHA to the small zone HARBOUR. When computational modeling of tsunami waves' spreading in mentioned water areas, there were used the following variants of source (see tables 5 – 7):

- variant *M1* – wave is set on the sea border of the calculation zone in the form of $A_o\sin(\pi t/T_o)$ or $A_o\sin(2\pi t/T_o)$, where A, and T_o – initial tsunami amplitude and tsunami period (in meters and seconds);

- variant *M2* – initial disturbance, being the some parts of ((generalized)) tsunami source, where L, W, x_0, y_0 – length, width, and coordinates of source's center (in the size of calculation zone's net step A), A, – maximum initial amplitude (in meters), a – an angle of deviation of the source's axis with respect to the direction North – South;
- variant M.3 – the same as *M2* but in the form of ellipse, where *a, b, x,* y – big and small semi–axes, center coordinates (in the size of calculation zone's net step A), A, – maximum initial amplitude (in meters), a – an angle of deviation of big ellipse's axis with respect to the direction North – South.

The influence of mechanism of shearing and of form of the initial rise in tsunami source on the height of the wave in coastal zone was studied in the work [193, where it is shown, in particular, that the most effective form of wave in the tsunami source is to set it in the form of «cap» – semi–ellipsoid. As the result of carried out computational experiments there were calculated wave fields on different moments of time and mareograms for the points, corresponding to the location of main (N_2), (N_4) and azimuth (N_1), (N_3), (N_5) gages of the control gage in the area of the defended point (N_7), and hypothetical gage (N_6) on the sea border of the calculation zone HARBOUR (fig. 15, 16).

In Tabl. 5-7, there are represented main calculation data: sizes of maximum amplitudes A_2, A_4, A_7 for the main mareograph points N_2, N_4, N_7, and also A_6 – amplitude of maximum fluctuation for the calculation mareograph point – N_6. At the same time, coefficients of strengthening of tsunami wave K_1, K_2, K_3 are calculated as

$$K_1 = A_6/A_2, K_2 = A_6/A_4, K_3 = A_7/A_6,$$

and resulting coefficients for the *Nomograms I* and *II* are

$$K_I = K_1 * K_3, K_{II} = K_2 * K_3, \text{ accordingly.}$$

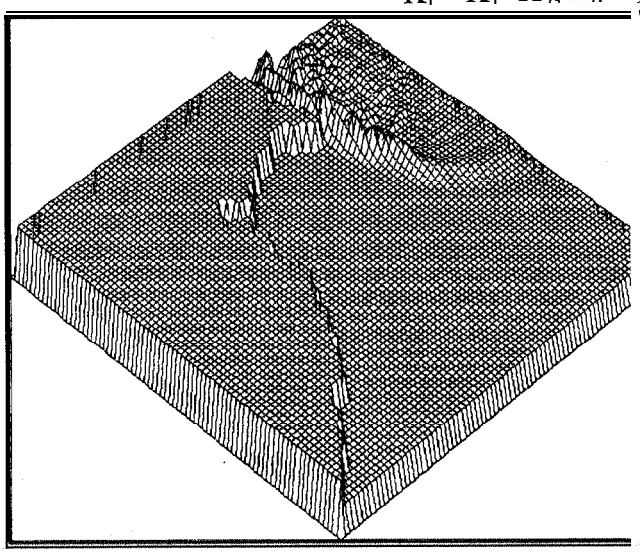

Figure 15. Calculation zone KAMCHATKA. The spreading of wave from the source, located near c. Shipunsky.

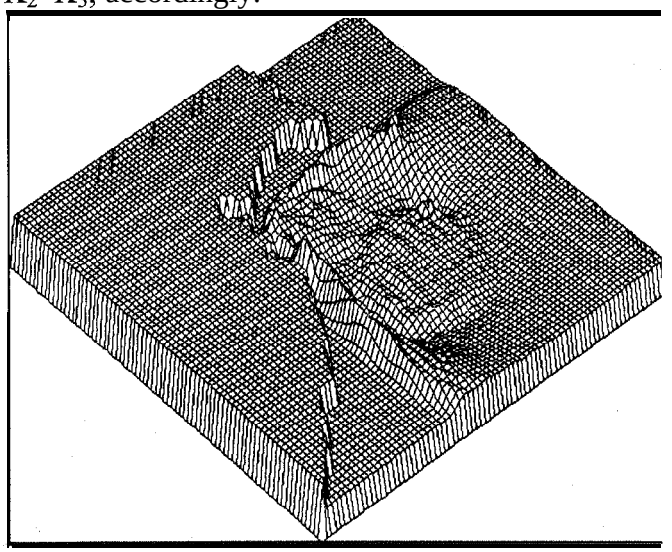

Figure 16. Calculation zone KAMCHATKA. The spreading of wave from the source, located near continental slope.

Analysis of the results of computational experiments for the zones KAMCHATKA, AVACHA, and HARBOUR allowed to estimate «project» coefficients of strengthening K_I, K_{II} depending on waves' periods. Such dependence appeared to be essential. Resulting calculation nomograms for the defended point are represented in the Fig. 17, 18. The scale for estimating the degree of tsunamidanger (wave's influence, the size of possible damage) depending on expected (predictable) wave's height in the specified point (see legends to nomograms) is accepted in accordance with data, represented in the work [20]. These nomograms are developed without taking

into consideration possible wave's strengthening due to ebb-and-flow and rundown-runup events in water area. Corresponding correction may be taken into account after fulfilling additional on-site investigations.

Table 5. Calculation of tsunami wave's parameters for the zone KAMCHATKA

Type of the source	Parameters of the source				A_2, m	A_4, m	A_6, m	K_I	K_{II}
	A_o, m		T_o, sec		*1*	*2*	*3*	*4*	*5*
M1	1		300		3.8	1.4	3.8	1.0	2.7
	1		600		4.3	1.5	4.8	1.1	3.2
	1		900		3.7	1.6	4.5	1.2	2.8
	1		1200		3.1	1.7	4.1	1.3	2.4
	1		1800		2.6	1.4	3.6	1.4	2.6
	1		750		4.2	1.5	4.8	1.1	3.2
	1		500		4.5	1.4	4.8	1.0	3.4
M2	*L, W,*	*(x,y)*	CL	A_o, m	*1*	*2*	3	4	*5*
	800*10	(20,60)	– 45	2		1.3	3.9		3.0
	800*10	(20,60)	– 60	2		1.3	3.7		2.8
	800*10	(20,60)	– 30	2		1.3	4.0		3.0
	800*10	(10,10)	+ 45	2	4.5		1.5		0.3
M3	*a*b*	*(x,y)*	*α,°*	A_o, m		*2*	3		*4*
	20*10	(20,60)	– 45	2		0.88	2.7		3.07
	5*10	(30,50)	– 45	2		0.96	3.0		3.10
	10*6	(30,50)	– 45	2		0.64	1.8		2.8
	10*6	(10*10)	+ 45	2					
	15*10	(30,50)	+ 45	2		0.72	2.2		2.8
	15*10	(30,50)		2		0.88	2.8		3.1
	10*15	(30,50)		2		0.80	2.5		3.1

Table 6.

Type of the source	Parameters of the source				A_2, m	A_4, m	A_6, m	K_I	K_{II}
	A_o, m		T_o, sec		*1*	*2*	*3*	*4*	*5*
M1	1		600		3.6	1.4	4.0	1.1	2.8
	1		900		3.2	1.3	3.4	1.0	2.6
	1		1200		2.8	1.2	3.0	1.0	2.5
	1		1800		2.3	1.1	2.7	1.1	2.4
	1.5		2400		2.6	1.8	4.1	1.0	2.3
M3	*a*b*	*(x,y)*	*α°,*	A_o, m	*1*	*2*	*3*	*4*	*5*
	50*30	(50,90)	+ 45	2		1.0	2.8		2.8
	25*15	(50,90)	– 45	2		0.7	1.8		2.6
	50*30	(50,90)	+ 45	2		1.0	2.6		2.6
	25*15	(50,90)	+ 45	2		0.6	1.6		2.7
	50*30	(50,90)		2		1.0	2.6		2.6
	30*50	(50,90)		2		0.9	2.4		2.7

Table 7.

A_o, m / T_o, sec	1.0		2.0		3.0		4.0		6.0		8.0	
	A_7	K_3	A_7	K_3	A_7	K_3	A_7	K_3	A_7	K_3	A_7	K_3
300	0.78	0.8	1.71	0.9	2.82	0.9	4.17	1.0	6.24	1.0	7.94	1.0
600	1.28	1.3	2.79	1.4	4.52	1.5	6.21	1.5	8.94	1.5	10.20	1.3
900	1.47	1.5	2.92	1.5	4.57	1.5	6.06	1.5	9.33	1.5	10.14	1.3
1200	1.66	1.7	3.36	1.7	5.32	1.7	6.98	1.7	10.4	1.7	09.89	1.2
1800	3.07	3.0	6.15	3.0	9.23	3.0	7.44	1.9	11.0	1.9		

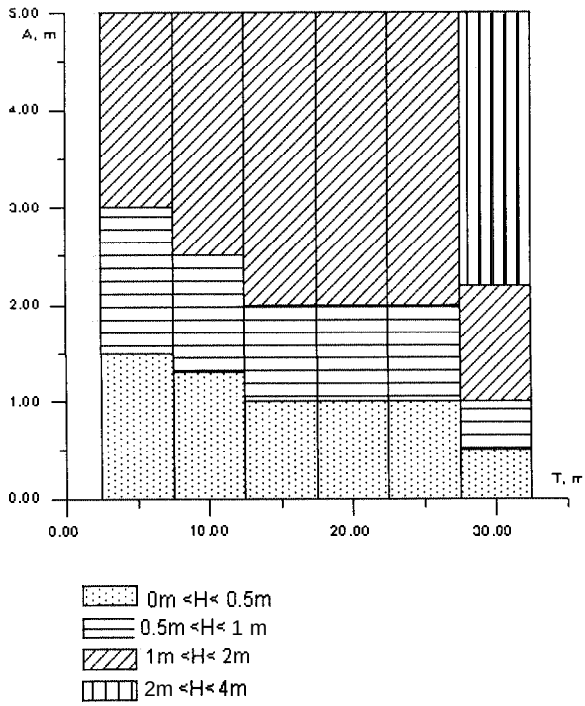

Figure 17. Nomogram I for estimating the degree of tsunamidanger on the basis of wave's monitoring on the gage N_2

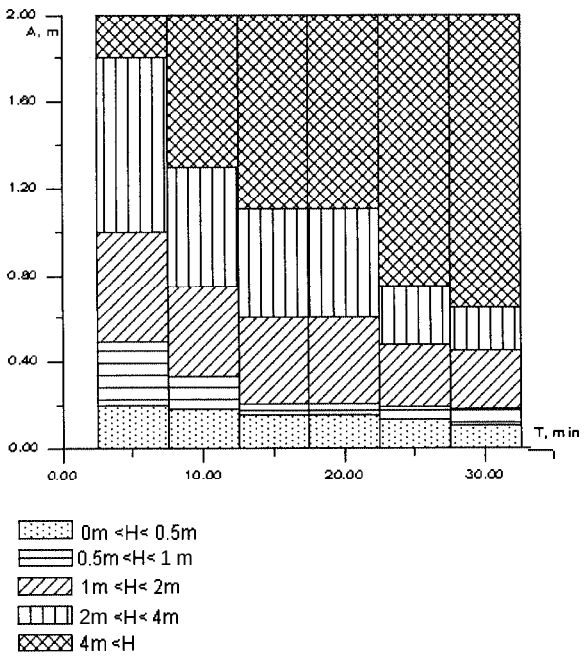

Figure 18. Nomogram I for estimating the degree of tsunamidanger on the basis of wave's monitoring on the gage N_4

REFERENCES

1. Bernard E.N., Behn R.R., Hebenstreit G.T., and et. all. On Mitigation Rapid Onset Natural Disasters: Project THRUST // EOS, 1988. – Vo1.69. -N 34.
2. Earthquake countermeasure in Shizuoka Prefecture // Shizuoka Prefectural Government. Earthquake Preparedness Division. – 1985. – 33 p.
3. Cox D., Morgan I. Local Tsunamis in Hawaii – implications for warning // Report of Hawaii Institute of Geophysics N 84-4 – Honolulu, 1984. – 104 p.
4. National Report of France // Tsunami Newsletter,1985. -Vol. 18. -N 2. – P. 21-29.
5. Averyanova V.A. Regularities of Orientation of Movements When Kuril-Kamchatka Earthquakes and Possibility of Zoning Tsunamigenic // Tsunami Problem. – M: Nauka, 1968. – P. 105-120.

6. Fedotov S.A. Long-term Seismic Forecast for Kuril-Kamchatka Zone // Tsunami Problem. – M: Nauka, 1968. -P. 121-132.
7. Zayakin Yu.A., Luchinina A.D. – Tsunami Catalogue in Kamchatka. – Obninsk, 1987, 5 1 p.
8. Ikonnikova L.A. Extremely Large Tsunami near the Soviet Pacific Coast // Papers of DVNIIGMI. – Vladivostok, 1964. – Vol. 17. – P. 69-75.
9. Ikonnikova L.A. Tsunami Atlas. – DVNIIGMI, Vladivostok, 1963.
10. Pelinovsky E.N. Nonlinear Dynamics of Tsunami Waves. – Gorkiy: IPF , 1982. – 226 p.
11. Karev V.Yu., Simonov K.V., Chubarov L.B., Shokin Yu.I. Computational Experiment in Tsunami Problem: Detailed Tsunamizoning of Pacific Coast of Kamchatka // Tsunami Investigation. – M: Nauka, 1990. – N 4. –P. 64-84.
12. Seliverstov N.I., Bondarenko V.I., Nadezhny A.M. Structure of Continental Slope of Eastern Kamchatka // Geology of Far East Suburb of Asia. – Vladivostok, 198 1. – P. 78-90.
13. Kaplin P.A.,Ionin A.S. Some Peculiarities of Coastal Relief of Kuril-Kamchatka Zone in Connection with Tsunami Problem // Bulletin of the Seismology Council of AS USSR. – M., 1961. – N 9. – P. 74-88.
14. Atlas of Tsunami Maximum Setup / Ed.-in-Chief Solovyev S.L. – Vladivostok, DVNIGMI, MGI AS USSR, 1978. – 61 p.
15. Go Ch.A., Kaystrenko V.M., Pelinovsky E.A, Simonov K.V. Forecast of Tsunamidanger for the Coast of Kamchatka // Meteorology and Hydrology, 1986. – N 7. – P. 74-8 1.
16. Shokin Yu.I., Chubarov L.B., Marchuk An.G., Simonov K.V. Computational Experiment in Tsunami Problem. – Novosibirsk: Nauka SB, 1989. – 167 p.
17. Fedotova Z.I. The Simple Numerical Method for a Long-Wave on a Beach // XIX-th Biennial Symposium on Advanced Problems and Methods in Fluid Mechanics.Abstract of papers. – Warsaw, 1989. – P. 200-201.
18. Kim K.Y., Reid R.O., Whitaker R.E. On Open Radiational Boundary Condition for Weakly Dispersive Tsunami Waves // J. Comp. Physics, 1988. – Vol. 79. – P. 327-348.
19. Gusyakov V.K., Chubarov L.B. Numerical Modeling of Excitation and Spreading of Tsunami in a Coastal Zone // Physics of Earth, 1987. – N 11. – P. 53-64.
20. Manoilin S.V. Some Experimentally-Theoretical Methods of Determing Tsunami Influence on Hydrotechnical Constructions and Water Areas of Sea Ports // Preprint N 5, CC SB AS. – Krasnoyarsk, 1989. – 45 p.

This study has been supported by the Russian Basic Research Foundation (Grants NN 00-01-00899, 00-15-96172), Integration Program of SB RAS (Project N 2000-l) and Federal Integration program (Project N 274)

ANALYTICAL SOLUTION AND NUMERICAL MODEL FOR THE INTERFACE IN A STRATIFIED LONG WAVE SYSTEM

Monzur Alum Imteaz
Research Fellow
Department of Civil Engineering
The University of Queensland, Brisbane, QLD 4072, Australia.

and

Fumihiko Imamura
Professor
Disaster Control Research Centre
Graduate School of Engineering
Tohoku University, Aoba, Sendai 980-8579, Japan.

ABSTRACT

For a two layered long wave propagation, linearized governing equations, which were derived earlier from the Euler equations of mass and momentum assuming negligible friction and interfacial mixing are solved analytically using Fourier transform. For the solution, variations of upper layer water level is assumed to be sinosoidal having known amplitude and variations of interface level is solved. As the governing equations are too complex to solve it analytically, density of upper layer fluid is assumed as very close to the density of lower layer fluid to simplify the lower layer equation. A numerical model is developed using the staggered leap-forg scheme for computation of water level and discharge in one dimensional propagation having known amplitude for the variations of upper layer water level and interface level to be solved. For the numerical model, water levels (upper layer and interface) at both the boundaries are assumed to be known from analytical solution. Results of numerical model are verified by comparing with the analytical solutions for different time period. Good agreements between analytical solution and numerical model are found for the stated boundary condition. The reliability of the developed numerical model is discussed, using it for different a (ratio of density of fluid in the upper layer to that in the lower layer) and β (ratio of water depth in the lower layer to that in the upper layer) values. It is found that as 'α' increases amplification of interface also increases for same upper layer amplitude. Again for a constant lower layer depth, as 'β' increases amplification of interface. also increases for same upper layer amplitude.

INTRODUCTION

Stratified flow is related with many environmental phenomena. Salt water intrusion in estuaries, spillage of the oil on the sea surface, spreading of dense contaminated water, sediment laden discharges into lakes and flow due to landslides are examples of stratified flow. In deep sea due to temperature gradient a strong stratification occurs.

Tsunamis are generated due to disturbances of free surface caused by not only seismic fault motion but also landslide and volcanic eruptions (Imamura and Imteaz, 1995). Tsunamis are categorized in to a long wave and long wave theory has been applied for the governing equations of propagation of tsunami considering a single layer (i.e. equal density throughout the depth). But even only for the consideration of density gradient in the deep sea it is necessary to consider the stratified layers. The internal hydraulics of a single layer, either beneath or above a stagnant or passive layer, is discussed in standard references (Prandtl, 1952 and Turner, 1973). There are some studies on two-layers long waves or flows in the case of underwater landslides generating tsunamis (Hampton, 1972; Parker, 1982; Harbitz, 199 1; Jiang & Leblond; 1992).

In the past years a number of analytical and experimental studies were carried out on two layer flow. There are a few numerical models on unsteady gravity currents (Akiyama et all, 1990; Kranenburg, 1993). But all of them compared their model results with experimental results or with results of previous researcher, none of them discussed the validity of numerical results comparing with analytical solution, although analytical solution is the best way to compare the numerical results. Because the mixing or entrainment process at the interface has not been successfully developed by physical model.

Imamura and Imteaz (1995) have developed a numerical model on two-layerd long wave flow, which was compared with the analytical solution. In the developed model variations of interface was assumed to be known and variations of top surface was solved numerically and analytically. But often it is more difficult to know the variations of interface, rather it is easier to know the variations of top surface. The present model solves the variations of interface having known amplitude for the variations of top surface. Also the variations of interface is solved analytically to validate the developed numerical model. The developed model is used for different conditions to see the properties of two-layer flow.

NOTATIONS

ρ = Density of fluid
M = Discharge per unit width of flow
η = Water surface elevation above still water level
a = Ratio of density of upper layer fluid to lower layer fluid
h = Still water depth
x = Distance along downstream direction
t = Axis representing time
g = Acceleration due to gravity
i = Spatial node points in finite difference scheme

n = Temporal node points in finite difference scheme
β = Ratio of depths of lower layer to upper layer
k = Wave number
c = Wave celerity
a = Time dependent amplification factor of wave
η_0= Initial amplitude of wave

THEORETICAL BACKGROUND

A mathematical model for two layer flow in a wide channel with non-horizontal bottom was set up assuming a hydrostatic pressure distribution, negligible friction and negligible interfacial mixing. Also uniform density and velocity distributions in each layer were assumed. Considering the two-dimensional case as shown in Figurel, Euler equations of motion and continuity for each layer were integrated. The detailed derivations of the integrated equations are described by Imteaz, M. A. (1993). The equations are non-linear in nature. Considering the small amplitude waves compared to the still water depth, non-linear terms were neglected. The linearized governing equations are as follows:

Governing equations for upper layer-

$$\frac{\partial M_1}{\partial x} + \frac{\partial(\eta_1 - \eta_2)}{\partial t} = 0 \tag{1}$$

$$\frac{\partial M_1}{\partial t} + g h_1 \frac{\partial \eta_1}{\partial x} = 0 \tag{2}$$

and for lower layer,

$$\frac{\partial M_2}{\partial x} + \frac{\partial \eta_2}{\partial t} = 0 \tag{3}$$

$$\frac{\partial M_2}{\partial t} + g h_2 \left\{ \alpha \left(\frac{\partial \eta_1}{\partial x} + \frac{\partial h_1}{\partial x} - \frac{\partial \eta_2}{\partial x} \right) + \frac{\partial \eta_2}{\partial x} - \frac{\partial h_1}{\partial x} \right\} + g \eta_2 \left(\alpha \frac{\partial h_1}{\partial x} - \frac{\partial h_1}{\partial x} \right) = 0 \tag{4}$$

Where, η is the water surface elevation, h the still water depth, M the discharge, ρ the density of fluid, $a = \rho_1/\rho_2$, x for spatial direction and t for time domain. Subscripts 1 and 2 indicate the upper and lower layer respectively.

$\partial h/\partial x$ terms were ignored, assuming a flat bottom to ease the analytical solution. By simple differential operation and substitution four linearized equations were transformed into two equations, one equation for each layer.

Upper layer equation is,

$$\frac{\partial^2 \eta_1}{\partial t^2} - g h_1 (1 + \alpha\beta) \frac{\partial^2 \eta_1}{\partial x^2} - g h_2 (1 - \alpha) \frac{\partial^2 \eta_2}{\partial x^2} = 0 \tag{5}$$

and lower layer equation is,

$$(1+\alpha\beta)\frac{\partial^2 \eta_2}{\partial t^2} - gh_2(1-\alpha)\frac{\partial^2 \eta_2}{\partial x^2} - \alpha\beta\frac{\partial^2 \eta_1}{\partial t^2} = 0 \qquad (6)$$

where, β is h_2/h_1. In above two equations, the last terms are added to the simple wave equation as an external force.

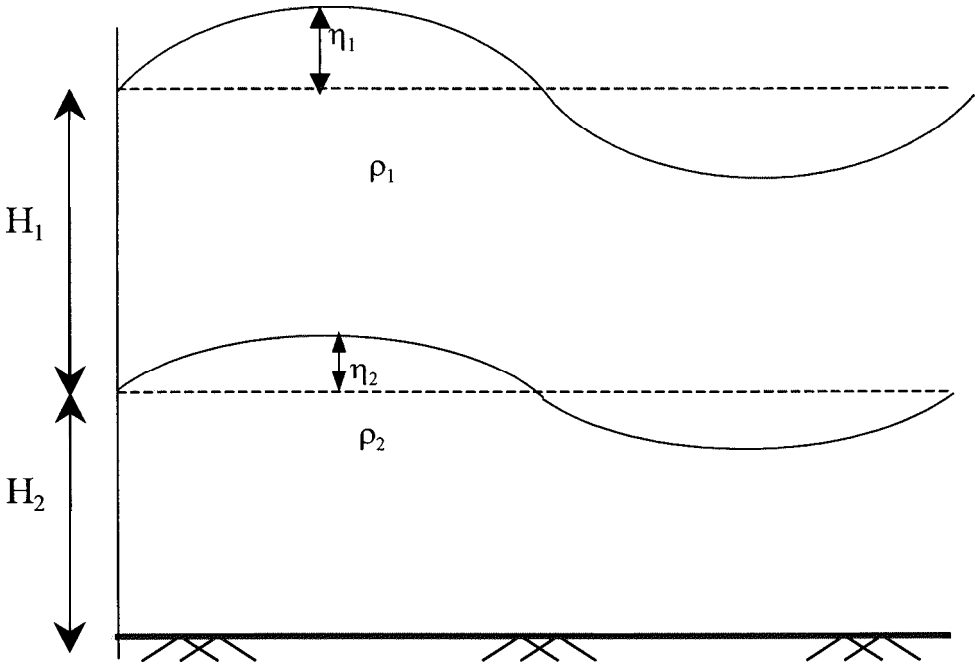

Figure 1 Scematic diagram of two layer profile

ANALYTICAL SOLUTION

The general solution forms of the equations 5 and 6 are still unknown. For $a \approx 1$, the Equation 5 becomes a simple wave equation, general solution form of which is available. The equations were solved using Fourier transform with the assumption that, $a \approx 1$. With the stated assumption, the solution of upper layer water level, η_1 can be expressed as,

$$\eta_1 = a_1 \int \hat{\eta}_0 e^{ik(X-C_1 t)} dk \qquad (7)$$

And, the interface level can be assumed as,

$$\eta_2 = a_2(t) \int \hat{\eta}_0 e^{ik(X-C_2 t)} dk \qquad (8)$$

Where, $C_1 = \sqrt{gh_1(1+\alpha\beta)}$, $C_2 = \sqrt{gh_2(1-\alpha)/(1+\alpha\beta)}$

and a, is constant to be known, and a, is a function of time to be solved.

Substituting Equations (7) and (8) to Equation (6) we get the ordinary differential equation for a_2 as follows:

$$\int\left[\frac{d^2a_2}{dt^2} - 2ikC_2\frac{da_2}{dt} + \frac{\alpha\beta C_1^2 a_1 k^2}{(1+\alpha\beta)}e^{ik(C_2-C_1)t}\right]\hat{\eta}_0\, e^{ik(X-C_2t)}\,dk = 0 \qquad (9)$$

Applying the initial condition that at t = 0, a, = 0, M_2 =0 and $\partial M_2/\partial x$ =0 yields, $\partial\eta_2/\partial t$ = 0. From Equation 8,

$$\frac{da_2}{dt}e^{ik(X-C_2t)} + a_2(-ikC_2t)e^{ik(X-C_2t)} = 0$$

As a_2 =0 at t=0, from above equation, da_2/dt=0. Integration of Equation 9 yields,

$$\frac{da_2}{dt} - 2ikC_2a_2 = -\frac{\alpha\beta C_1^2 a_1 k^2}{ik(C_2-C_1)(1+\alpha\beta)}e^{ik(C_2-C_1)t} + m \qquad (10)$$

where, m is the constant of integration. Substituting the values of a, and da_2/dt at t=0, yields, $m=\alpha\beta gh_1a_1k/i(C_2-C_1)$.

Assuming, $a_2 = b(t)e^{2ikC_2t}$ and substituting it into Equation 10, yields,

$$\frac{db}{dt} = \frac{\alpha\beta gh_1a_1k}{i(C_2-C_1)}\left[e^{-ik(C_2+C_1)t} - e^{-2ikC_2t}\right] \qquad (11)$$

Integration of Equation 11 yields,

$$b = -\frac{\alpha gh_2a_1}{(C_2-C_1)}\left[\frac{e^{-ik(C_2+C_1)t}}{C_2+C_1} - \frac{e^{-2ikC_2t}}{2C_2}\right] + n$$

where, n is the constant of integration. Applying the initial condition (i.e. at t=0, b=O) to the above equation, $n= \alpha gh_2a_1/2C_2(C_2+C_1)$. Substituting, this 'n' value to the above equation,

$$b = -\frac{\alpha gh_2a_1}{(C_2-C_1)}\left[\frac{e^{-ik(C_2+C_1)t}}{C_2+C_1} - \frac{e^{-2ikC_2t}}{2C_2}\right] + \frac{\alpha gh_2a_1}{2C_2(C_2+C_1)} \qquad (12)$$

Therefore,

$$a_2 = -\frac{\alpha gh_2a_1}{(C_2^2-C_1^2)}e^{-ik(C_1-C_2)t} + \frac{\alpha gh_2a_1}{2C_2(C_2-C_1)} + \frac{\alpha gh_2a_1}{2C_2(C_2+C_1)}e^{2ikC_2t}$$

Finally, solution for the wave profile of interface is as follows:

$$\eta_2 = \left[\frac{a_1\alpha gh_2}{2C_2(C_1+C_2)}\right]\int\hat{\eta}_0\, e^{ik(X+C_2t)}\,dk + \left[\frac{a_1\alpha gh_2}{2C_2(C_2-C_1)}\right]\int\hat{\eta}_0\, e^{ik(X-C_2t)}\,dk$$

$$-\left[\frac{a_1\alpha gh_2}{C_2^2-C_1^2}\right]\int\hat{\eta}_0\, e^{ik(X-C_1t)}\,dk \qquad (13)$$

Solution for η_2 is combination of three wave components, two progressive waves and one reflective wave. One of the progressive waves has celerity c, and other has celerity c_2. The reflective wave component has celerity c_2. To get a clear idea on the analytical solution (i.e. Equation 13) wave profiles for different components of interface after 4 sec have shown in Figure 2. It is found that the progressive wave with celerity c_2 and reflective wave with celerity c_2 has much higher magnitude than

the progressive wave of c_1. But higher magnitude components are opposite in sign, so resultant of them become lower in magnitude and comparable with lower amplitude wave component of c,. Therefore final resultant shape of interface is also influenced by wave component of celerity c_1.

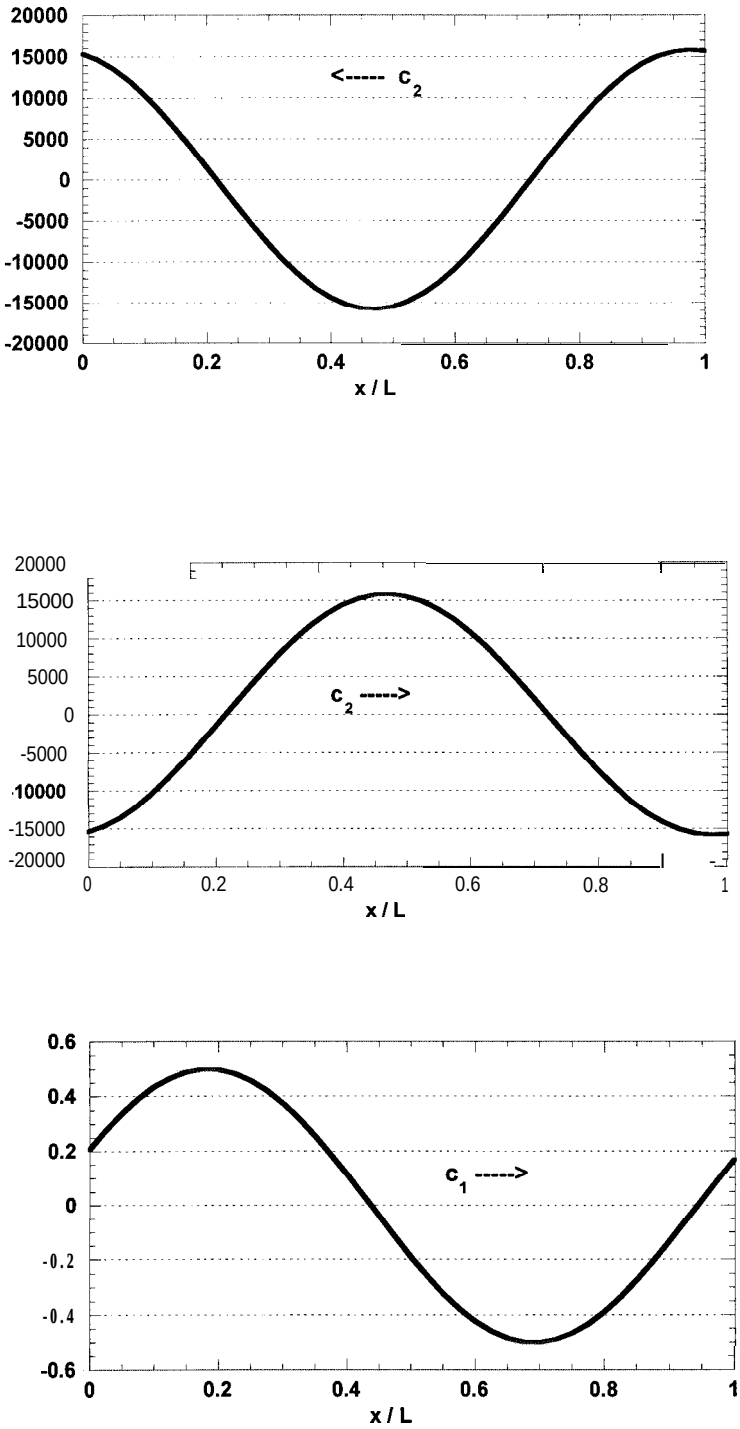

Figure 2 Magnitudes (in m) of different components of interface wave after 4s (analytical solution)

NUMERICAL MODEL

The staggered leap-frog scheme was used to solve the governing equations numerically. This scheme is one of explicit central difference schemes with the truncation error of second order. The staggered scheme considers that the computation point for one variable, η does not coincides with the computation point for other variable, M.. There are half step differences, ½Δt and ½Δx between computation points of two variables as shown in Figure 2. It looks as one variable is placed at the middle of ΔtΔx rectangle, placing other variable at the four comer of rectangle and vice versa. The same scheme was used by Imamura and Imteaz (1995), for the numerical solution of upper layer water level having known variation of interface, which produced good results. Using this scheme, the finite difference equations for the proposed governing equations are,

For upper layer,

$$\frac{\eta_{1,i}^{n+1/2} - \eta_{1,i}^{n-112} - \eta_{2,i}^{n+1/2} + \eta_{2,i}^{n-1/2} + M_{1,i+1/2}^{n} - M_{1,i-1/2}^{n}}{At \qquad Ax} = 0 \tag{14}$$

$$\frac{M_{1,i+1/2}^{n} - M_{1,i+1/2}^{n-1}}{\Delta t} + g\frac{h_{1,i+1} + h_{1,i}}{2}\frac{\eta_{1,i+1}^{n-1/2} - \eta_{1,i}^{n-1/2}}{\Delta x} = 0 \tag{15}$$

and for lower layer,

$$\frac{\eta_{2,i}^{n+1/2} - \eta_{2,i}^{n-1/2} + M_{2,i+1/2}^{n} - M_{2,i-1/2}^{n}}{At \qquad \Delta x} = 0 \tag{16}$$

$$\frac{M_{2,i+1/2}^{n} - M_{2,i+1/2}^{n-1}}{At} + g(\alpha - 1)\frac{\eta_{2,i+1}^{n-1/2} + \eta_{2,i}^{n-1/2}}{2}\frac{h_{1,i+1} - h_{1,i}}{\Delta x} + g\frac{(h_{2,i+1} + h_{2,i})}{2}$$

$$\frac{\alpha(\eta_{1,i+1}^{n-1/2} - \eta_{1,i}^{n-1/2}) + (\alpha - 1)(h_{1,i+1} - h_{1,i}) + (1 - \alpha)(\eta_{2,i+1}^{n-1/2} - \eta_{2,i}^{n-1/2})}{\Delta x} = 0 \tag{17}$$

Where 'n' denotes the temporal grid points and 'i' denotes the spatial grid points as shown in Figure 3. Ax and At are spatial grid spacing and time spacing respectively.

In spatial direction all of η_1, η_2 at step 'n-1/2' and all of M,, M_2 at step '(n-l)' are given as initial conditions. For all later time steps at left and right boundaries all values of η_1 and η_2 are calculated using analytical solution. By using momentum equations for upper and lower layer all M, and M_2 at step 'n' are calculated. Then using the continuity equation for lower layer all values of η_2 at step '(n+1/2)' are calculated. Finally using the values of η_2, M_1 and the continuity equation for upper layer, all values of η_1 at step '(n+1/2)' are calculated. Similarly using latest values of η_1, η_2, M, and M_2 as initial conditions calculations proceeded in time direction up to the desired step.

VERIFICATION OF NUMERICAL MODEL

Numerical model results were compared with the analytical solution for different time periods. As

the analytical solution was found for a ≈ 1, a value was taken as 0.99 (i.e. $\rho_1 = 0.99$ and $\rho_2 = 1$ .O). The value of 'β' was taken as 1 (i.e. $h_2 = h_1 = 25$ m). The wave amplitude of top surface, a, was taken as 1 m, which is smaller compared with the depth of layer, 25 m. Wave period for both the layers was taken as 18.28 sec. Wave period was assumed in such a way that computational domain become equals to the wave length. For spatial grid points ΔX=10 m and for temporal grid points ΔT=0.02 sec was used.

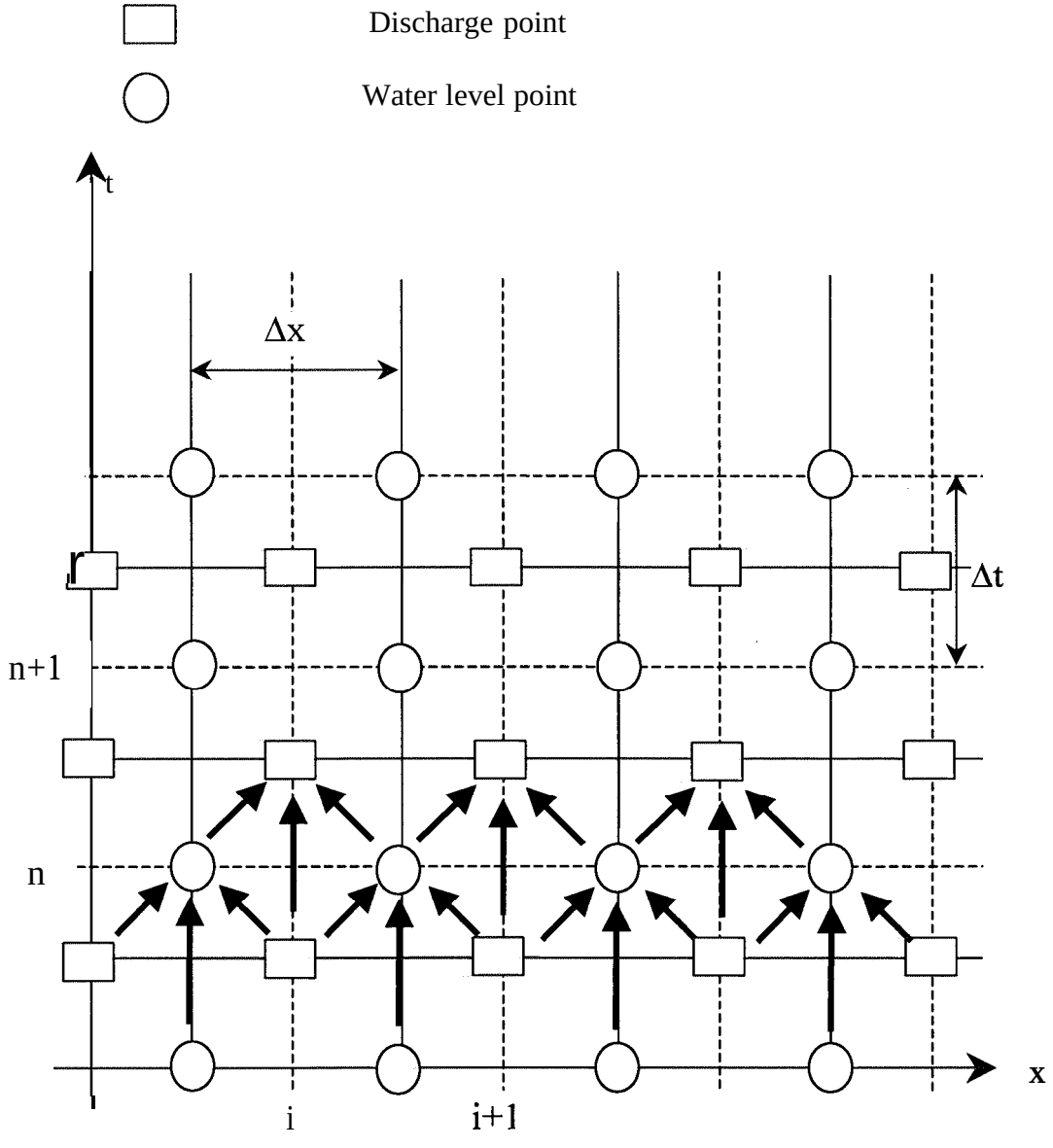

Figure 3 Schematics of staggered leap-frog scheme

As initial condition (i.e. at t = 0) all η_2 and M_2 values were taken as zero. For top surface, initial condition was found just substituting t = 0 in the known expression of η_1, which gives,

$$\eta_1 = a_1 \mathrm{Cos}(kx) = a_1 \mathrm{Cos}(\frac{2\pi}{L} x) \qquad (18)$$

Where, a, is amplitude; k is wave number and L is wavelength.

Discharge was calculated by using the linear relationship between the water level and discharge as,

$$M_1 = \sqrt{(g/H_1)}\,\eta_1(H_1+\eta_1)$$

For numerical calculations it is necessary to assume appropriate boundary conditions at both upstream and downstream boundaries. For top surface and interface values of water level at upstream and downstream boundaries were assumed same as calculated by analytical solution.

Comparisons of analytical and numerical solution for different time periods are shown in Figure 4 and Figure 5. Figure 4 shows the comparison for top surface and Figure 5 shows the comparison for interface. From the figures it is clear that numerical model produces good agreement with analytical solution. For the interface the agreement is very good, but for the top surface there are small differences between numerical and analytical solutions specially in the peak values. The reason for this is that for the analytical solution, the term $gh_2(1-\alpha)\partial^2\eta_2/\partial x^2$ in Equation 5 was ignored, which accounts for the effect of interface to the top surface. But in the numerical solution the effect of interface to the top surface was not ignored. With the increase of $\partial^2\eta_2/\partial x^2$ value, the effect of interface to the top surface is no longer negligible.

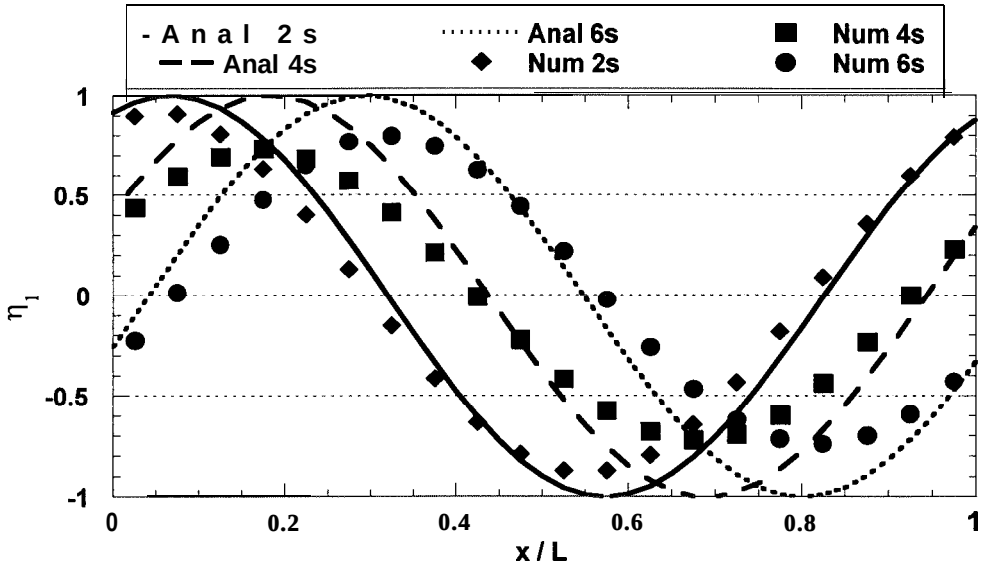

Figure 4 Comparison of numerical model for top surface (α=0.99)

To check the validity of the model for low a values, the model was simulated for α=0.01 and compared with the analytical solution of same a value. Figure 6 shows the comparison for top surface and Figure 7 shows the comparison for interface for different time periods. It is found that numerical model produced very good agreement with analytical solution. No difference was found between numerical solution and analytical solution as it was found for the case of α=0.99. As the variations of η_2 was very small, the term $gh_2(1-\alpha)\partial^2\eta_2/\partial x^2$ was also very small and negligible. So on-mission of this term from Equation 5 did not cause any error.

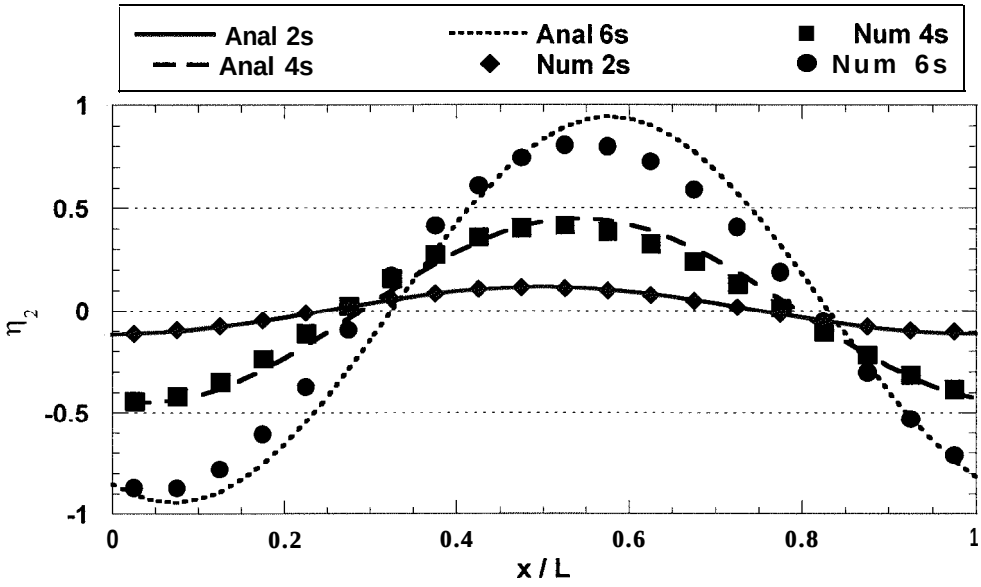

Figure 5 Comparison of numerical model for interface (α=0.99)

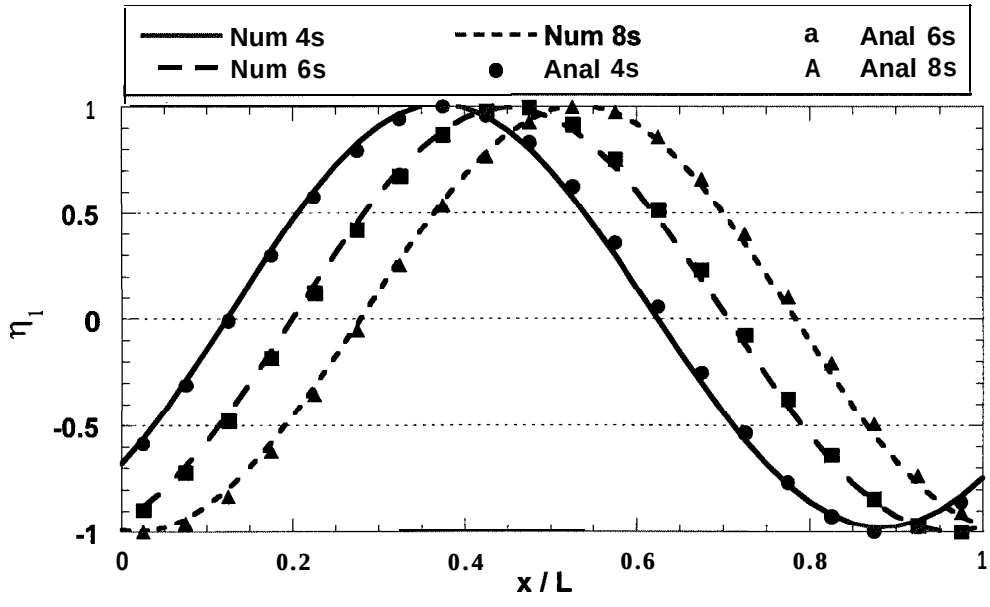

Figure 6 Comparison of numerical model for top surface (α=0.01)

MODEL SIMULATIONS

Effect of Relative Density

Model was simulated for different values of $\alpha(=\rho_1/\rho_2)$, keeping parameters ρ_2 and β as constant. For all cases ρ_2 was assumed as 1 .0, also the value of β was assmued as 1.0 (i.e. h_1=25.0 m and

h_2=25.0 m). Figure 8 shows the profiles of interface at different time periods for two different values of a (i.e. α=0.1 and α=0.75). Variation of amplification of interface with 'α' for different time period is shown graphically in Figure 9. From the figures it is found that as 'α' increases the amplification of interface also increases and vice versa. This is due to the interaction of two layers, as 'α' increases interaction also increases. Because if 'ρ_1' increases keeping 'ρ_2' constant, energy of top surface wave trough will also increase and higher energy will transfer to a same density fluid of lower layer. This higher energy transfer will cause higher amplification of interface. This phenomena also can be proved through derived governing equation for lower layer (Equation 6), in this equation last term ($\alpha\beta\partial^2\eta_1/\partial t^2$) is the effect from upper layer. With the increase of 'a' value, effect of upper layer to lower layer also increases.

From Equation 6, comparing last term to the second term, the effect of upper layer to the lower layer is varying with the function, $\alpha\beta/gh_2(1-a)$. Considering gh_2 as constant, the function is dependent on a and β only. Figure 10 shows the variation of the function with a for different β values. It is found that for higher β values, the effect of a is very high.

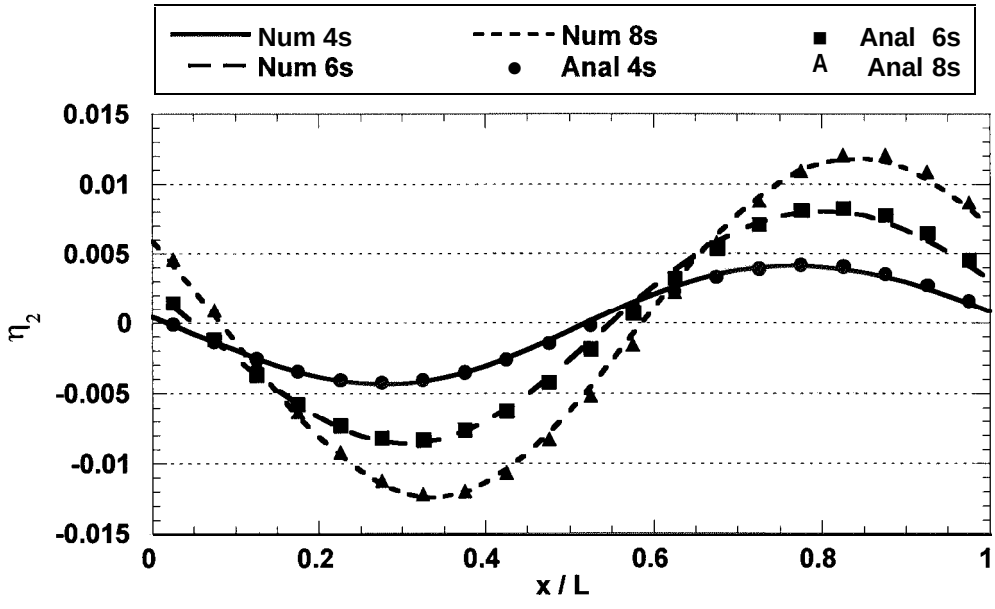

Figure 7 Comparison of numerical model for interface (α=0.01)

Effect of Relative Layer Depths

Model was simulated for different values of $\beta(=h_2/h_1)$, keeping other parameters (ρ_1, ρ_2 and h_2) as constant. For all cases, ρ_1 was assumed as 0.1, ρ_2 was assumed as 1 .O and h_2 was assumed as 25.0 m. Figure 11 shows the profiles of interface at different time periods for two different values of β (i.e. β=1.0 and β=2.0). Variation of amplification of interface with 'β' for different time period is shown graphically in Figure 12. From the figures it is found that as 'β' increases the amplification of interface also increases and vice versa. Again this is due to the interaction of two layers. If 'h_1' decreases keeping 'h_2' constant (i.e. increase of β), upper layer fluid volume associated with certain wavelength will be relatively lower. Therefore energy produced by the top surface wave will cause higher displacement of

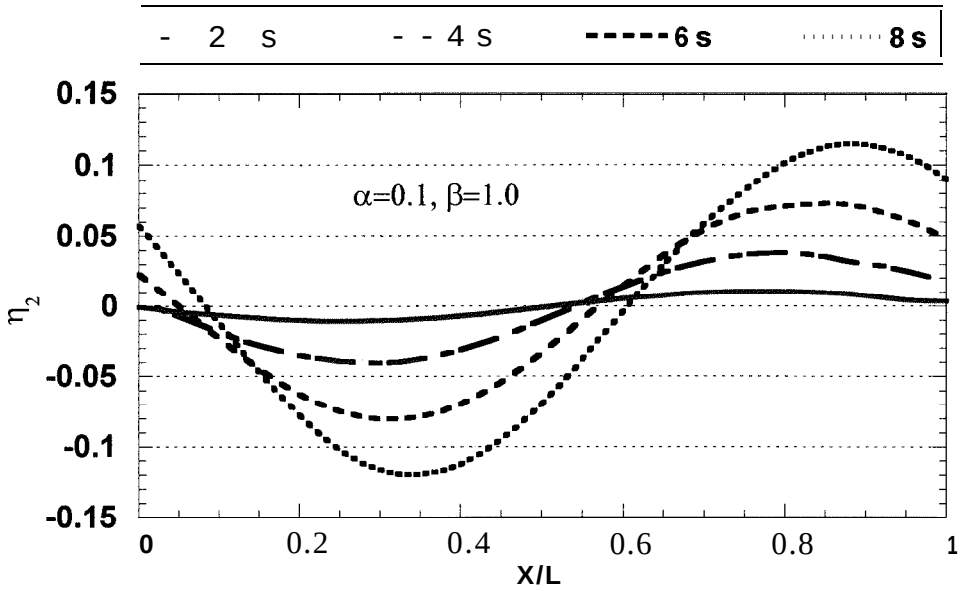

Figure S(a) Interface profile at different time priod for α=0. 1

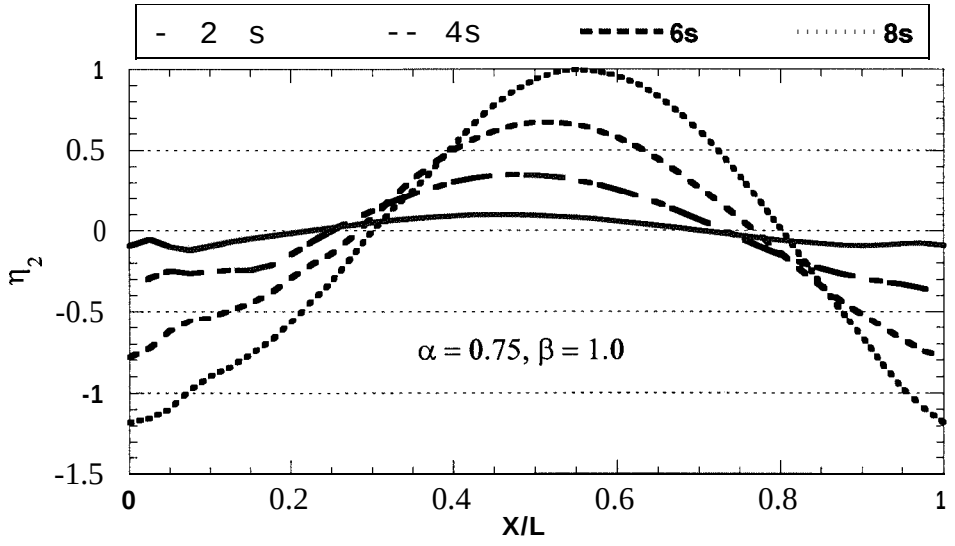

Figure 8(b) Interface profile at different time priod for α=0.75

interface (due to lower volume). Similarly if h, increases keeping h_2 constant, displacement of interface will decrease due to higher volume of upper layer. These characteristics can also be explained by derived governing equation of lower layer (i.e. Equation 6). As last term of Equation 6 $(\alpha\beta\partial^2\eta_1/\partial t^2)$ is the effect from upper layer. With the increase of 'β' value, effect of upper layer to lower layer also increases. As discussed in the previous section, the effect of upper layer to the lower layer is varying with the function, $\alpha\beta/gh_2$(1 -a). The function is dependent on a and β only for a constant gh_2 value, has a linear relationship with β for a certain a value. Figure 13 shows the variation of the function with β for different a values.

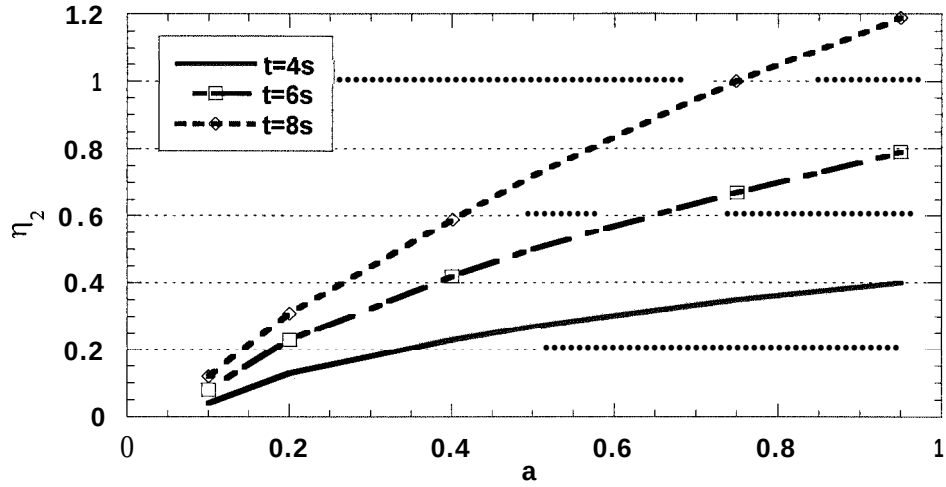

Figure 9 Variation of interface amplification with α

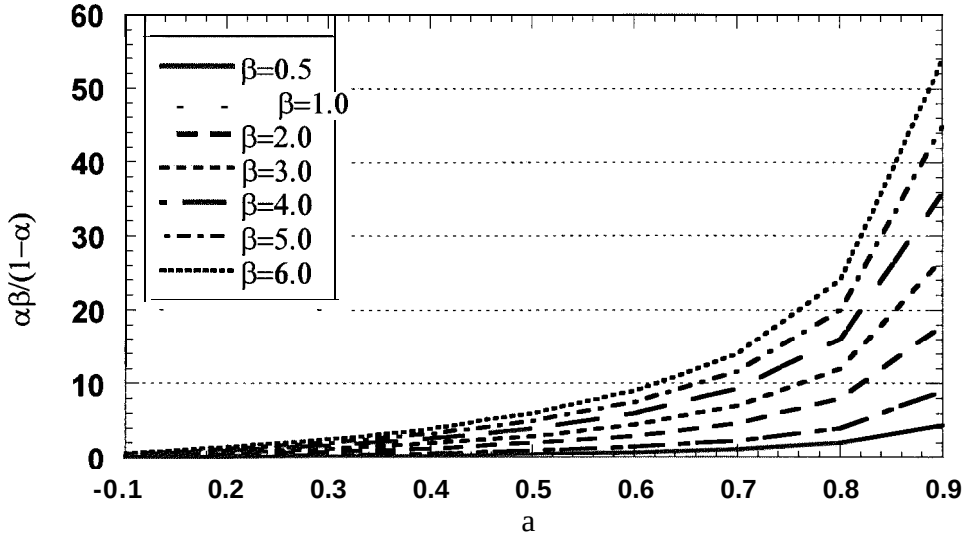

Figure 10 Effect of a on function that carries influence of upper layer to interface

CONCLUSION

Analytical solution was derived by using Fourier transform, only for a certain condition (i.e. $\rho_1/\rho_2 \approx 1$ .O). This solution contains two progressive waves with different celerities and one reflective wave. Numerical model was developed by using staggered leap-frog finite difference scheme. Accuracy of linear numerical model was discussed by comparing the results with analytical solution. General agreement between numerical model and analytical solution was good. Although analytical solution is valid for $\alpha \approx 1$ .O, but good agreement between analytical solution and numerical model was found even for the case of $\alpha \approx 0.0$. Numerical results are influenced by u/s and d/s boundary conditions, good

agreements were found when water levels (both interface and top surface) at both boundaries were calculated by analytical solution. But for other boundary conditions numerical model does not produce good results. Characteristics of the model was discussed by using it for different condition, different 'a' and 'β'. It was shown that for higher 'α' and for higher 'β', amplification of interface increases and vice versa. Both of these phenomena are reasonable and can be well explained by physical fluid properties. Capability of model for the simulation of interface wave variations having known variations of top surface will be useful for many related phenomena.

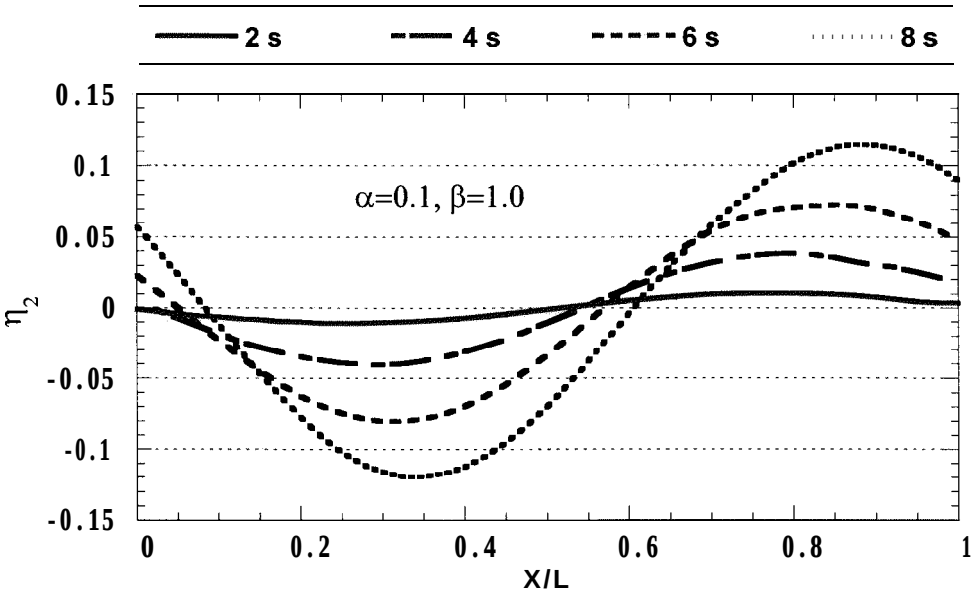

Figure 11 (a) Interface profile at different time period for β=1 .O

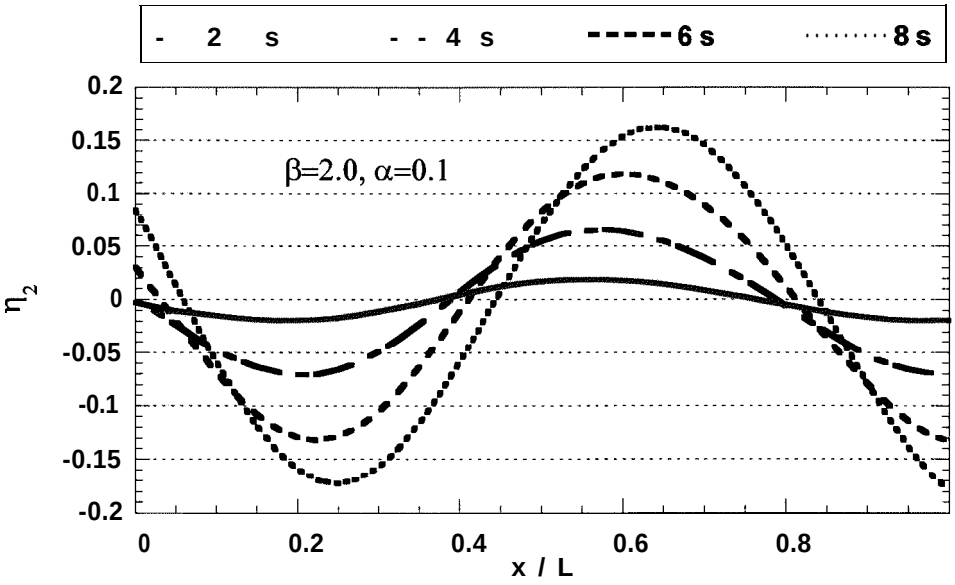

Figure 1 l(b) Interface profile at different time period for β=2.0

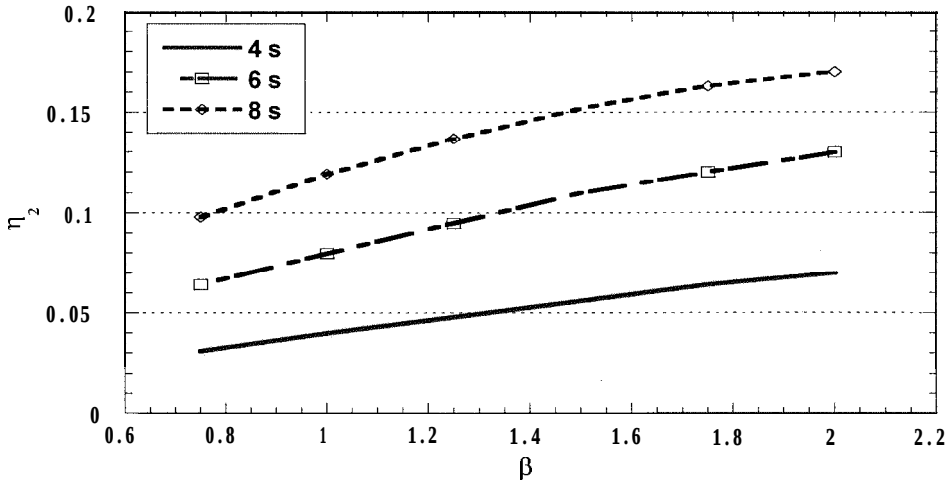

Figure 12 Variation of interface amplification with β

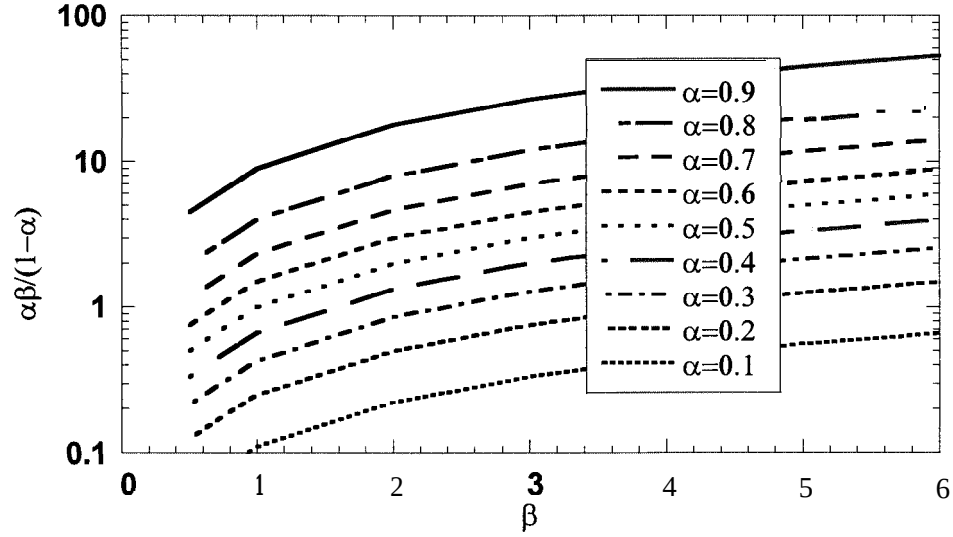

Figure 13 Effect of β on function that carries influence of upper layer to interface

REFERENCES

AIUYAMA, J., WANG, W. & URA, M. (1990) Numerical Model of Unsteady Gravity Currents, *Proc. 7th* Congress, APD, IAHR, Beijin.

HAMPTON, M. H. (1972) The Role of Subaqueous Debris Flow in Generating Turbidity Currents, *J. Sedimentary Petrology*, Vol. 42, No. 4, pp.775-793.

HARBITZ, C. (1991) Numerical Simulations of Slide Generated Water Waves, *Sci. of Tsunami Hazards*, Vol. 9, No. 1, pp. 15-23.

IMAMURA, F. & IMTEAZ, M. A. (1995) Long Waves in Two-Layers: Governing Equations and Numerical Model, *Sci. of Tsunami Hazards*, Vol. 13, No. 1, pp. 3-24.

IMTEAZ, M. A. (1993) Numerical Model for the Long Waves in the Two Layers, *Master's Thesis, Asian Institute of Tech.*, Bangkok, 86p.

JIANG, L. & LEBLOND, P. H. (1992) The Coupling of Submarine Slide and the Surface Waves which it Generates, J. Geophys. Res., Vol. 97, No. C8, pp.12713-12744.

KRANENBURG, C. (1993) Unsteady Gravity Currents Advancing along a Horizontal Surface, J. *Hydraulic Research*, Vol.3 1, pp.49-60.

PARKER, G. (1982) Conditions for Ignition of Catastrophically Erosive Turbidity Currents, *Marine Geology*, Vol. 46, pp. 307-327.

PRANDTL, L. (1952) Essentianls of Fluid Dynamics, *New* York, *Hafner*.

TURNER, J. S. (1973) Buoyancy Effects in Fluids, *Cambridge University Press*, Cambridge, 367p.

THE ASTEROID TSUNAMI PROJECT AT LOS ALAMOS

Jack G. Hills and M. Patrick Goda
T-6, Mail Stop B288
Los Alamos National Laboratory
Los Alamos, NM 87545

A FIRST TSUNAMI SYMPOSIUM CONTRIBUTION

ABSTRACT

Tsunami may produce most of the economic damage in large asteroid impacts. The dust from large asteroid impacts would produce worldwide darkness lasting several months that may kill more people by mass starvation, especially in developing countries, than will tsunami, but the dust should not severely affect economic infrastructure. The tsunami may even kill more people in developed countries with large coastal populations, such as the United States, than the starvation resulting from the darkness. At Los Alamos we are in the middle of a systematic study of asteroid tsunami. The study is divided into three parts: A determination of those regions of Earth that are most susceptible to asteroid tsunami by simulating the effect of an asteroid impact into mid-ocean, the simulation of the formation of the initial crater and the waves generated by it by use of a SPH code, and a Monte Carlo study of the accumulative effect of many small impactors on some of the more strategically valuable regions that we find to be particularly vulnerable in the first part of this study. The first part of the study is well underway. Progress has been made on the other two. The critical factor in the third part of the study is to accurately determine the dispersion in the waves produced by the smaller impactors. Dispersion may greatly reduce the effectiveness of the smaller impactors at large distances from the impact point. We wish to understand this effect thoroughly before performing the Monte Carlo study. We have modeled the effect of mid-Atlantic and mid-Pacific impacts with craters 300 and 150 km in diameter. The larger of these craters would be produced by a KT-size impactor. The code has been progressively improved to eliminate problems at the domain boundaries, so it now runs until the tsunami inundation is finished. We find that tsunami generated by a large mid-Atlantic impactor will travel to the Appalachian mountains in the Eastern USA. We find that the larger of these two mid-Atlantic impacts would engulf the entire Florida Peninsula. The smaller one would inundate the eastern third of the peninsula while a tsunami passing through the Gulf of Cuba would inundate the west coast of Florida. Impacts at three different sites in the Pacific show the great vulnerability of Tokyo and its surroundings to asteroid tsunami.

INTRODUCTION

Asteroid and comet impacts cause a variety of damage: blastwaves, fires, craters and earthquakes on land and tsunami at sea (Hills and Goda 1993, hereafter referred to as HG, and Hills and Goda 1998a). If the impactor is more than 1 km in diameter, it ejects enough dust above the atmosphere to produce global darkening. Global darkening over a period of months could cause mass starvation in developing countries. The work of HG showed that tsunami is the most significant form of damage for objects smaller than this threshold for global darkening.

HG studied the fragmentation and energy dispersal of asteroids in the atmosphere and found the fraction of their kinetic energy that remained when they hit ground. They found that common stony asteroids 200 meters in diameter and larger impact ground with most of their pre-atmospheric entry energy, which makes them very effective in producing tsunami. Asteroids of this size hit Earth about every 3000 to 5000 years, so the probability of one impacting in a given human lifetime is about 2-3%.

HG used this data on asteroid impact energies and the data on tsunami generated by nuclear explosives (Glasstone and Dolan 1977) to estimate the tsunami height from asteroid impacts. Fig. 1 (from HG) shows the resulting full height of tsunami in deepwater (before they hit land) at 1000 miles from the impact point as a function of asteroid radius and impact velocity. (Heights above sea level are half these values.) We note that asteroid tsunami are not important unless the impactor has a radius of about 100 meters (diameter 200 meters). In the absence of wave dispersion, even an asteroid 200 meters in diameter impacting in mid Atlantic would produce tsunami several meters high on either side of the ocean. We see that an asteroid 400 meters in diameter produces waves more than 10 meters above sea level at 1000 km from the impact point. In the absence of wave dispersion an object this size falling in the mid-Atlantic would produce tsunami more than 3 meters high before they come ashore in North America and Europe as the heights drop off inversely with distance from the impact point. This height would rise several fold as it comes ashore. Dispersion would reduce the heights of these waves, but Fig. 1 shows the potential seriousness of these waves.

The smaller the asteroid, the smaller the crater it produces, and the shorter the wavelength of the tsunami. At short enough wavelengths, wave dispersion may significantly reduce the tsunami height at a large distance (many wavelengths) from the impact point. To calculate the effect of wave dispersion on tsunami height will require solution of the Navier-Stokes equation in modeling the propagation from the impact point to the shore. Dispersion is expected to be important if the wave propagation distance is several thousand kilometers.

At Los Alamos we are in the middle of a systematic study of tsunami generated by asteroid impacts. In the first part of this study we are finding the shorelines around the Earth that are most vulnerable to asteroid tsunami by using models in which a large crater is put in the middle of the ocean. These craters are large enough that the wavelength of the disturbance produced by the crater refill and its subsequent rebound is comparable to that of long-period tsunami generated by earthquakes, so we are confident that they can travel across an ocean basin without significant dispersion. In the second part of the study

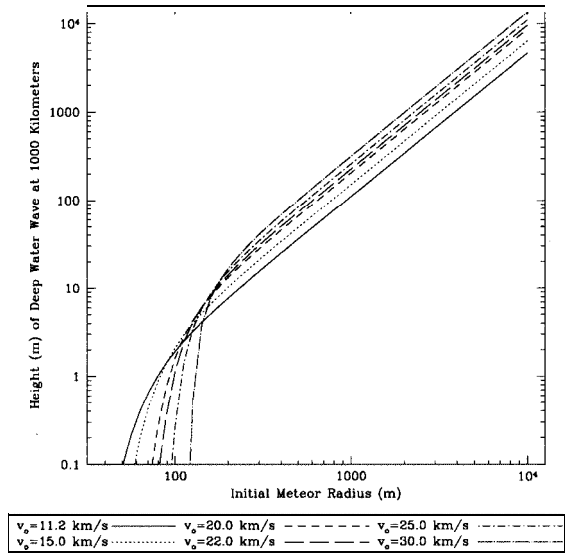

Figure 1: Full height of tsunami in deepwater at 1000 km from the impact site. (Wave height above sea level is half this value.) These values were obtained from the energy of impact of the asteroid allowing for atmospheric dissipation and scaled from experiments with nuclear explosives.

we are using a smooth-particle hydrodynamics (SPH) code to study the initial formation of the crater to find the size of the asteroid required to produce a given crater size. Thirdly, we are studying wave dispersion to better model how it reduces the wave heights in the shorter wavelength disturbances produced by smaller impactors. This is needed to allow us to study the accumulated effect of the numerous smaller impactors on strategic shorelines.

RUNUPS FROM LARGE IMPACTORS

The simulation of the runups by large impactors allows us to find areas of the Earth that are particularly sensitive to asteroid tsunami. Later, we will investigate how sensitive these same areas are to the multitude of many small impacts that occur between the large impacts.

The wavelengths of tsunami produced by larger asteroids are long enough (> 100 km) that wave dispersion is not a problem for wave run-lengths comparable to the width of Earth's oceans. We can model these tsunami accurately using the shallow water (or long-wavelength) approximation. We initially used the SWAN code (Mader 1988) for these calculations. This FORTRAN code has been tested extensively by comparing the runups predicted by the model against historical tsunami from earthquakes and landslides. As our first test case in our study, we modeled wave propagation resulting from a crater 150 kilometers across in the middle of the Atlantic Ocean (Hills and Mader 1997). We estimate that such a crater would be produced by an asteroid about 5-6 kilometers in diameter. An object at least this large impacts Earth every 10 million years. The code was used to find the wave height off the

coast of North America. The code was then rerun with a piston at the eastern boundary having an amplitude comparable to that height. The run time of the code was limited by instabilities at the boundaries. However, the run time was sufficient to show that the wave travels all the way to the Appalachian Mountains in the upper two-thirds of the United States. One of the intriguing results of that simulation was the small amount of flooding in Florida. We found that most of the tsunami energy was being reflected back into the Atlantic by the gradual continental shelf. When we had to terminate the calculations due to instabilities at the boundaries, we found that only the Miami area was flooded (due to tsunami funnelling by its natural shipping channel). As we shall later show, the Florida peninsula is badly flooded when the model is run for a longer time.

M.P. Goda rewrote the SWAN code in the computer language C and improved the graphics package for displaying tsunami runups. This SWIM (Shallow Water Inundation Model) code was tested against the original SWAN code to assure its accuracy. The boundary conditions were later improved to allow us to run the code for times much longer than permitted by SWAN. The new boundary conditions in effect advect the component of the wave that is parallel to the boundary out of the computational domain. This improvement allowed us to run SWIM for model times that are at least twice as long as the tsunami travel time across the major ocean basins. This new code will be ported to a massively parallel computer in the near future to allow runup and wave propagation calculations on a much finer grid than is practical with our current serial machines.

The first application of SWIM was to find the vulnerability of Europe to tsunami flooding from asteroid impacts (Hills and Goda 199813). Again, we took as the initial condition an impact crater 150 km in diameter in the middle of the Atlantic. This calculation was done before the code improvements allowed long running times, so again we used the code to find the height of the tsunami waves before they entered Europe and then restarted the calculations just before the tsunami came ashore using a piston of the same amplitude on the western boundary of the domain. This work showed the extreme vulnerability of the Iberian Peninsula to tsunami from impacts. Waves exceeding 100 meters in height were observed all along the Iberian peninsula. This is the result of the paucity of protective continental shelf around the peninsula. The Atlantic Coast of southern France also suffered severe flooding. The British Isles were much less affected because of the massive continental shelf surrounding them.

In the current paper we would like to report our early work using the improved SWIM code that allows much longer running times. This has allowed us to dispense with the use of the piston. We simply start with the initial crater and allow the computations to proceed until the elapsed time is at least twice the time required for tsunami to travel across the given ocean basin. We find that these long running times are necessary because reflection of tsunami waves off continents and island chains can cause noticeable enhancements in the tsunami runups in certain locales.

We made simulations with impact craters 150 km and 300 km in diameter in the Atlantic at (Long.,Lat.) = (40^o W, 35^oN). We also performed simulations in the Pacific with these two sizes of craters. These simulations were done for three different impact points: (Long, Lat) = (170^oW, 35^oN), (138.25^oW, 27.75^oN), and (169.75^oE, 28.75^oN). The Atlantic and Pacific impact sites are shown in Fig. 2. A crater 300 km in diameter would be produced by a KT size impactor about 10 km in diameter while the 150 km crater would be produced by

an object with half that diameter. The probability of the larger impactor hitting in a given year is about one in 100 million while the probability of the smaller impactor hitting in a given year is about 1 in 10 million. In these simulations the ocean bathymetry is determined from ETOP05 (from the US Defense Mapping Agency). This product provides topography on a grid with resolution of 5 arc minutes.

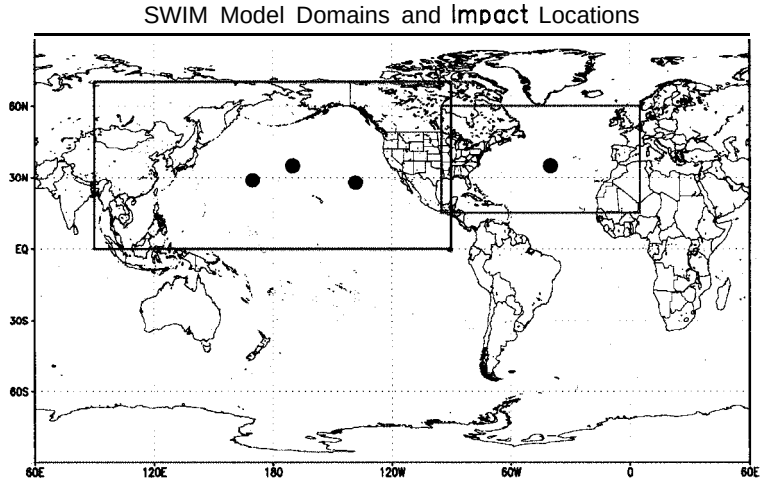

Figure 2: Positions of the four impact sites used in our models.

ATLANTIC IMPACTS

Fig. 3 shows the maximum wave height within the Atlantic ocean as the tsunami propagates away from the impact site. We note that some of the tsunami energy is funnelled south along the western edge of the mid-Atlantic Ridge. There is also a tongue of high water that moves towards Florida. This is due to an absence of sea mounts in that direction to reflect back the energy. We also note the shoaling as the tsunami hits the continental shelf. This provides good protection for the northern most part of the United States and for the Atlantic providences of Canada. It also provides good protection for the British Isles and the European Coast east of it. We also note the lack of protection by continental shelves in the southern Atlantic Coast of France, the Iberian Peninsula, and the Atlantic Coast of Africa.

The shoaling also slows down the tsunami as is evident in Fig. 4 which shows the tsunami travel time from the impact site. We note the slowing down of the tsunami off Florida and Georgia as the wave goes into the progressively shallower water. The situation is similar around the British isles. But, there is no significant slowing down of the tsunami around the Iberian Peninsula and North Africa.

As we might guess from the previous two plots, the most significant flooding in Europe occurred along the south Atlantic Coast of France and the Iberian Peninsula. Fig. 5 shows the depth of inundation along the Atlantic Coast of France. The depth is shown in meters above local ground level for the simulations with craters 150 and 300 kilometers in diameter. The depth of inundation in France is not as great as it is along the Iberian Peninsula where

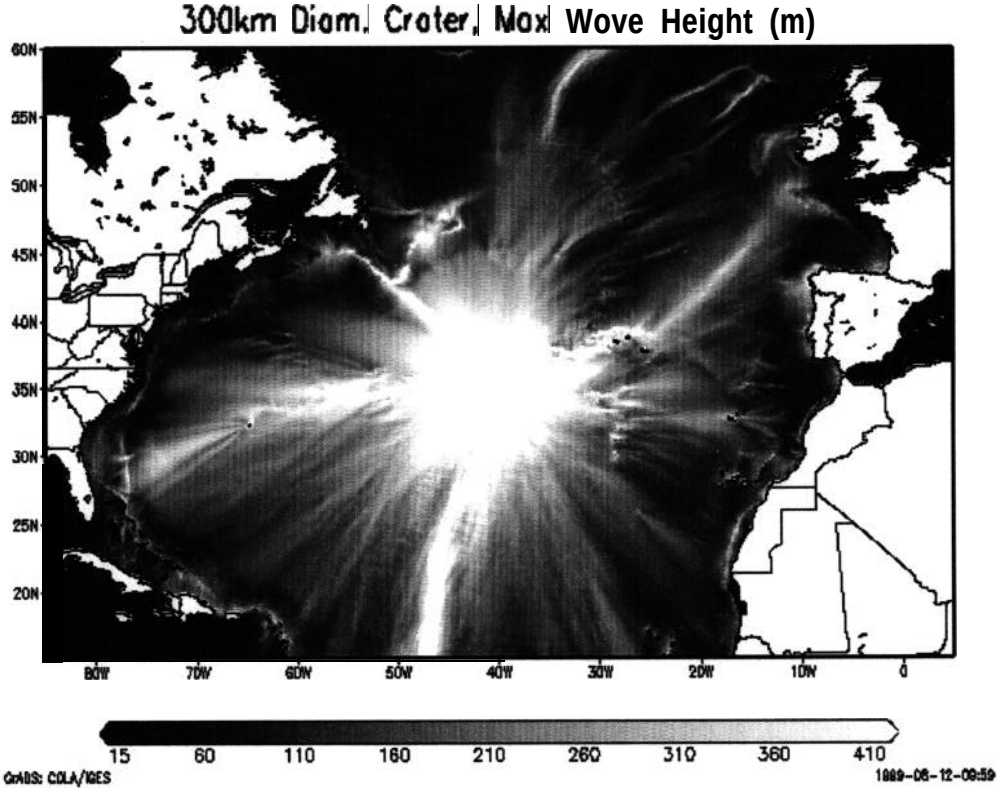

Figure 3: Maximum wave height above sea level reached at each point in the Atlantic Ocean as a result of the impactor. The grey scale gives the height in meters at each location.

the depth reaches over 200 meters for the larger crater and 100 meters for the smaller one, but the distance the flood moves inland in France is much greater due to the lack of mountains to contain it.

The damage is greater in North America than in Europe. The major difference between the results of the new simulations and that of the earlier one is the degree of flooding of the Florida Peninsula. Fig. 6 shows the maximum flooding produced by a crater 150 km in diameter and one 300 km in diameter. The figures show the maximum depth of inundation above local ground level at each point on the peninsula. We find much more profound flooding when we are able to run the code for a much longer time than the maximum possible in Hills and Mader (1998). The larger crater causes all of Florida to be inundated while the smaller one causes the Eastern third to be inundated with additional flooding occurring on the West Coast due to a tsunami wave passing through the straits between Florida and Cuba. The depth of inundation of the East Coast exceeds 100 meters in some places for the larger crater.

We find that two factors are responsible for this late-stage flooding in Florida: The considerable slowing down of the tsunami as it enters the shallows off Florida causes a mesa of water to slowly build up on this shelf. Then a second tsunami wave reflects off the Bahamas chain and piles up on top of the now much deeper water left by the passage of the first tsunami wave. When this mesa of water collapses, it produces the Florida flooding.

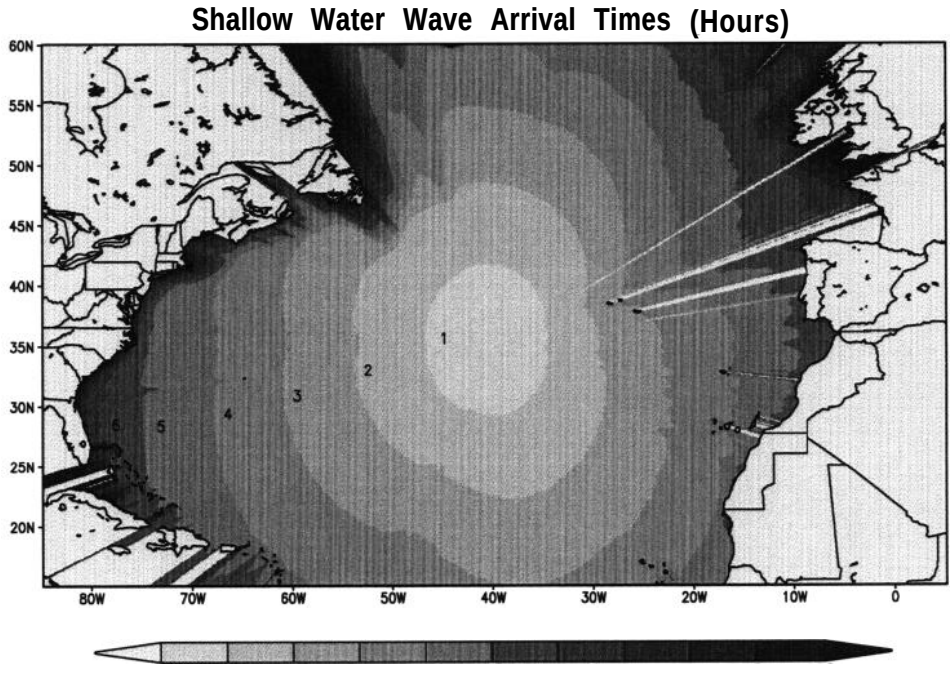

Figure 4: The grey scale shows the travel time between the impact site and each position in the Atlantic Ocean. We note the slowing down of the wave as it enters the continental shelf.

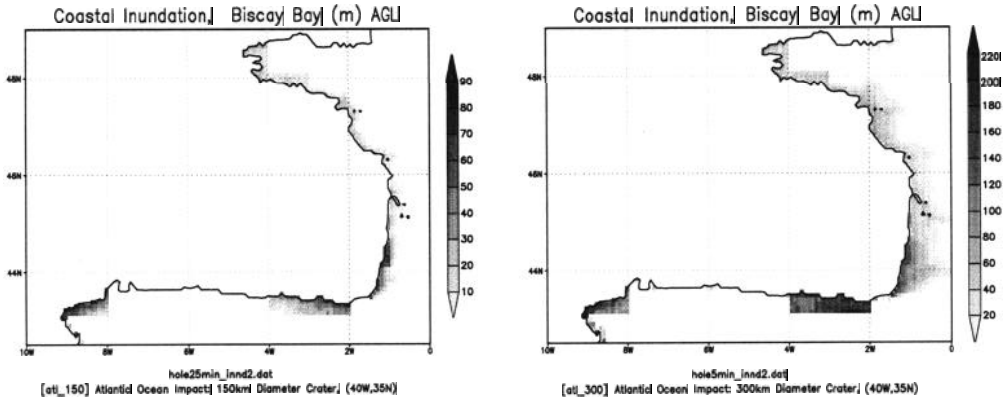

Figure 5: The depth of inundation along the Atlantic Coast of France as a result of the formation of a 150 km and 300 km impact crater in the middle of the Atlantic Ocean. The grey scale gives the maximum local flood depth in meters above mean ground level.

PACIFIC IMPACTS

Fig. 7 shows the highest water reached as the tsunami travels away from the centermost of the three impact sites in the Pacific for a 300 km diameter crater. We see the significant protection afforded by the Aleutian Islands and the continental shelf off Asia. China and most of mainland Asia is relatively protected by the extensive continental shelf. Japan has no significant continental shelf, so the tsunami slams directly into it. A similar situation

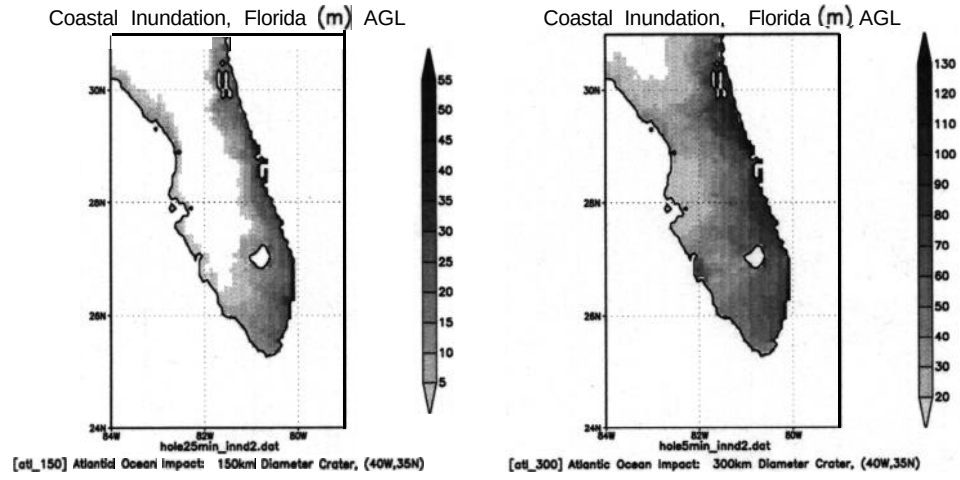

Figure 6: The depth of inundation in Florida due to the formation of a 150 km and 300 km diameter impact crater at the location shown in Fig. 2. The maximum flood depth shown in the figure is given in meters above the local ground level.

occurs along the West Coast of the United States. The West Coast is much more prone to tsunami flood than mainland Asia.

The plains around Tokyo are particularly prone to tsunami flooding. Figs. 8-10 show the depth of tsunami flooding in the vicinity of Tokyo, Japan from each of the three impact sites. Each figure shows the results for a crater 150 and 300 km in diameter. We note that the tsunami flood inundates Tokyo and its vicinity when the impact occurs at any one of the three impact sites.. Tokyo appears to be especially sensitive to tsunami from nearly any impact site in the Pacific.

The runup simulations for the West Coast of the United States do not look as dramatic as for Japan, principally because the coastal mountains restrict the flood to a narrow zone around the coast. However, many major cities are in this narrow coastal band. Fig. 11 shows the depth of inundation in the Pacific Northwest for the eastern most of the three Pacific impact sites. This is shown for the two different crater sizes. The tsunami tends to go up to the coastal mountains. We note the penetration of the tsunami up some of the major river valleys in this region. The apparent tranquil state in Seattle may be due to numerical limitations. The grid resolution may not be good enough to accurately model the passage of the tsunami wave through the straits between Vancouver Island and Washington State.

In the future we will improve the resolution by moving onto a 2 minute grid. This will be increased .to 1 minute resolution when this data becomes available. This will require the use of a massively parallel computer, which we have available at Los Alamos.

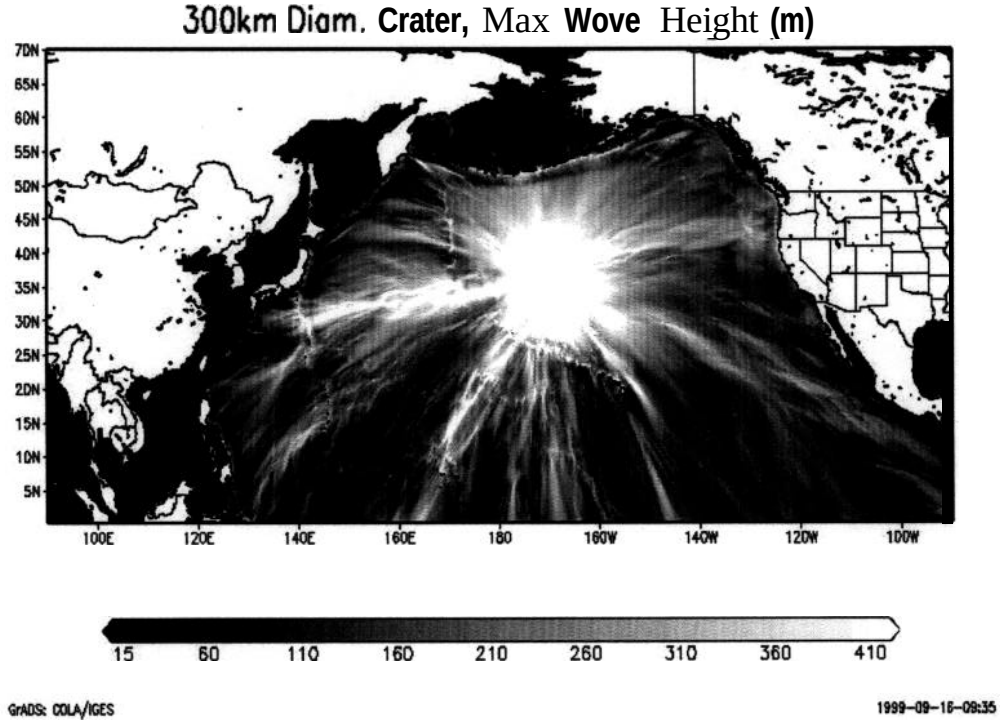

Figure 7: Maximum wave height above sea level in the Pacific due to the formation of an impact crater 300 km in diameter at the northern most of the three Pacific impact sites shown in Fig. 2.

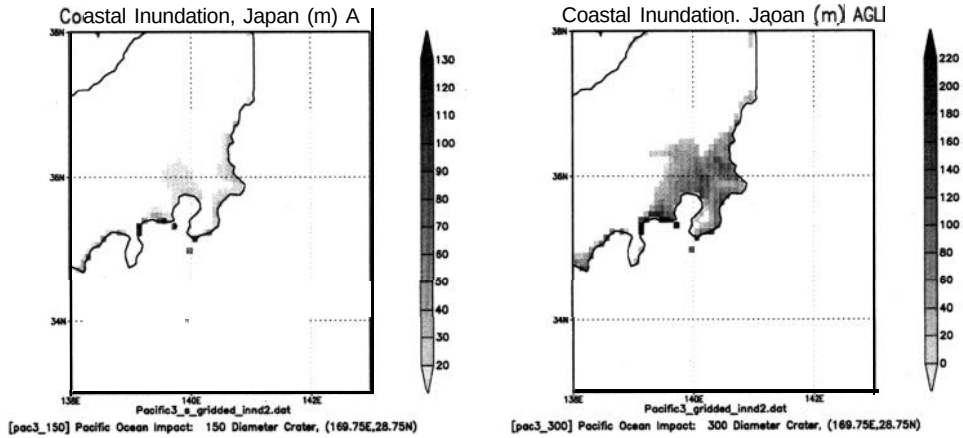

Figure 8: The maximum inundation depth in Japan due to the formation of an impact crater at the westernmost of the three Pacific impacts sites shown in Fig. 2. This is shown for impact craters 150 and 300 km in diameter. The depth is given as meters above local ground level. Note the extreme flooding of Tokyo and its vicinity.

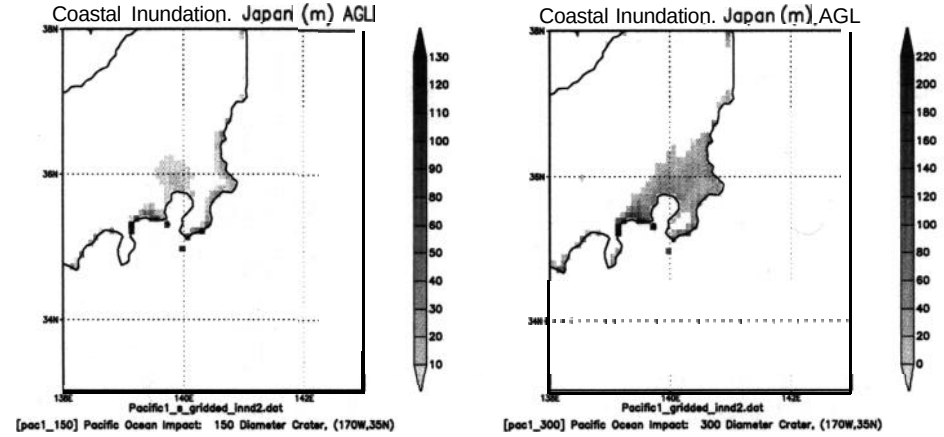

Figure 9: Same as Fig. 8 except it is due to an impact at the northernmost of the three Pacific sites shown in Fig. 2.

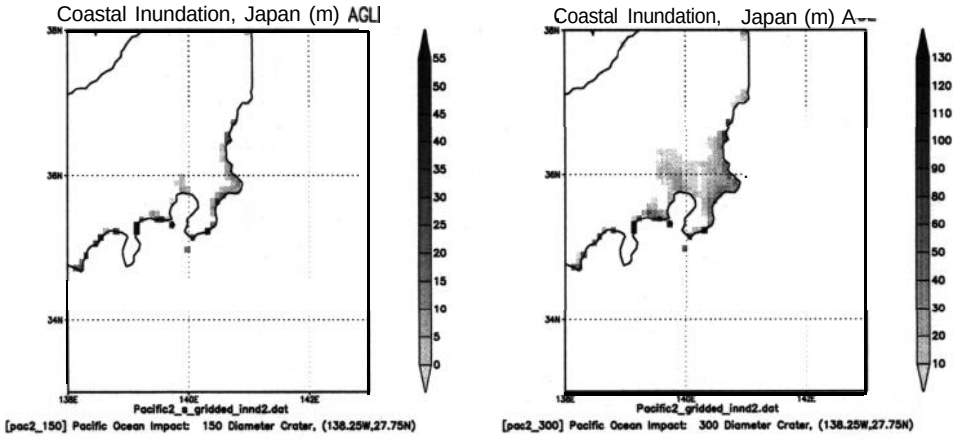

Figure 10: Same as Fig. 8 except it is due to an impact at the easternmost of the three Pacific sites shown in Fig. 2.

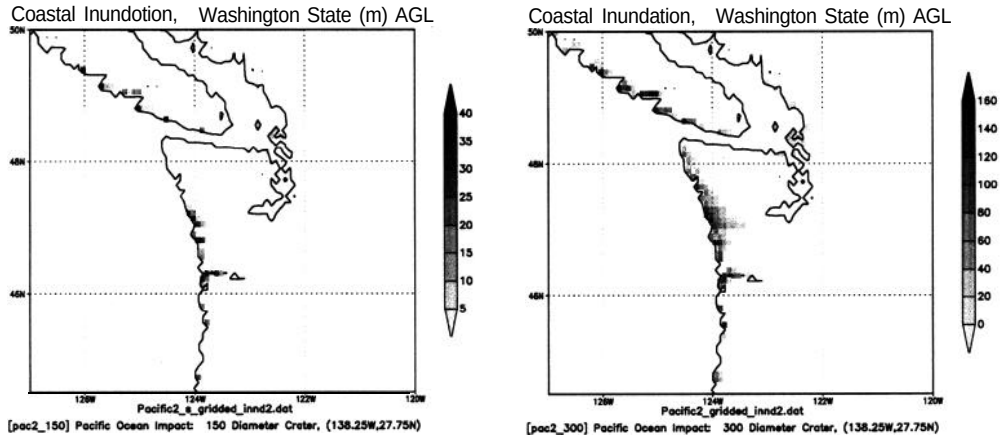

Figure 11: The maximum inundation on the Pacific Northwest Coast of the United States due to an impact at the easternmost of the three impact sites in the Pacific. The plot shows the maximum depth of flooding above local ground level at each point for impact craters 300 and 150 km in diameter.

CONCLUDING REMARKS

It is difficult to imagine trying to manage by normal civil defense procedures the catastrophes produced by asteroid impacts because of the large scale of the damage and short timescales involved. It would be far better to detect these objects well before they impact Earth. This will allow much more time for response. There should be a civil defense response to the degree that it is feasible. There also should be an active defense to assure that these larger impactors never hit the ground. As we see from the presentation by Johndale Solem at this conference, such defense is possible. It should be implemented.

Solem paper in Science of Tsunami Hazards, Vol 17, 141-154 (1999)

REFERENCES

Carrier, G.F. 1971, ***Mathematical Problems in the Geophysical Sciences, American Mathematical Society*** 1, 157-187, "The Dynamics of Tsunami".

Glastone, S. and Dolan, P.J. 1977, ***The Effects*** of Nuclear Weapons, third Ed. (U.S. Government Printing Office, Washington DC).

Hills, J.G. and Goda, M.P. 1993, ***Astron. J.*** **105,** 1114-1144, "The Fragmentation of Small Asteroids in the Atmosphere."

Hills, J.G., Nemtchinov, I.V., Popov, S.P., and Teterev, A.V. 1994, in ***Hazards due to Comet and Asteroid Impacts,*** p.779-789, "Tsunami Generated by Small Asteroid Impacts" (University of Arizona Press: Tucson).

Hills, J.G. and Goda, M.P. 1998a, ***Planet.*** Space Sci. 46, No. 2/3, 219-229, "Damage from the Impacts of Small Asteroids".

Hills, J.G. and Goda, M.P. 1998b, ***Science of Tsunami Hazards*** 16, 3-10, "Tsunami from Asteroid Impacts: The Vulnerability of Europe".

Hills, J.G. and Mader, C.L., 1997, in Near-Earth Objects, Annals of the New York Academy of Sciences, 822, 381-394 "Tsunami Produced by Impacts of Small Asteroids".

Mader, C.L. 1988, Numerical Modeling of Water Waves (University of California Press, Berkeley).

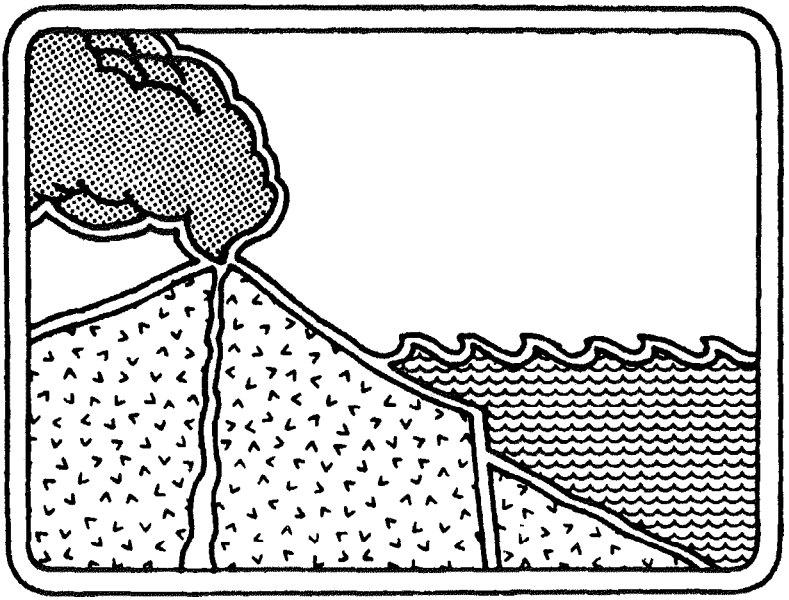

SECOND TSUNAMI SYMPOSIUM

MAY 28, 29, 30, 2002

EAST-WEST CENTER, UH

HONOLULU, HAWAII

http://www.ccalmr.ogi.edu/STH/symp2.html

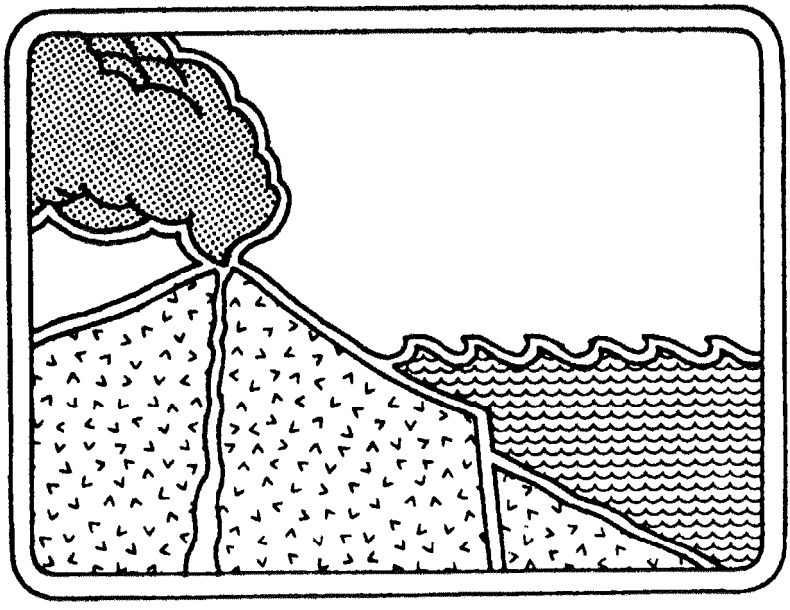

ABSTRACTS DUE - September 1, 2001

PAPERS DUE - January 1, 2002

Send Abstracts and Papers to
Dr. Charles L. Mader
1049 Kamehame Drive
Honolulu, HI 96825 USA
e-mail - MCCOH@juno.com

Application for Membership

THE TSUNAMI SOCIETY
P. 0. Box 37970
Honolulu, Hawaii 96817, USA

I desire admission into the Tsunami Society.

NAME _____

ADDRESS _____

_____

_____

Telephone/FAX _____

E-MAIL ADDRESS _____

Mail Registration to The Tsunami Society, P. 0. Box 37970, Honolulu, Hawaii, 96817, USA. The Membership Fee is $30.00 for individual Members and $100.00 for Institutions. Please make check to"The Tsunami Society".

Send dues for one year with application. Membership shall date from January 1 of the year in which the applicant joins. Membership of an applicant applying on or after October 1 will begin with January 1 or the following calendar year and his first dues payment will be applied to that year.

Membership includes a subscription to the society journal Science ***of Tsunami Hazards.***